INSTITUTE OF PHYSICS
POLISH ACADEMY OF SCIENCES

Valery Kolkovsky (Kalkouski)

“Planar nanostructures made of diluted magnetic semiconductors – epitaxial growth and transport properties”

Supervisor:
Prof. dr hab. Grzegorz Karczewski

Warsaw 2008

Dedicated to my family and blessed memory of my father

Acknowledgements

I would like to express my gratitude to the people who have supported me in preparing this thesis:

first of all I want to thank my supervisor, Prof. dr hab. Grzegorz Karczewski, for his guidance, invaluable advises and constant support during this research;

special thanks are due to my family and my bride for their constant support and inspiration;

also, I would like to thank all my friends and colleagues for their continuous support and friendly encouragement during the last five years;

moreover, special thanks to the Foundation of Polish Science for the financial support, which gives me a possibility to finish this thesis.

Motivation

Spintronics is one of the most exciting and challenging areas in nanotechnology which becomes more and more important in nowadays life. Spintronic-devices, combining the advantages of magnetic materials and semiconductors, play a significant role in high-density data storage, microelectronics, sensors, quantum computing and bio-medical applications, etc.

Using semiconductors for spintronic applications – where spin, in addition to a charge, is manipulated to influence electronic properties – has several advantages. First of all, integration of spintronics with traditional semiconductor technology calls for employing semiconductors (rather than metals) as media for spin control. Secondly, semiconductors are versatile materials, due to their electrical properties, and spin/magnetic characteristics. Doping control of electrical and magnetic properties, optical spin orientation and detection, bipolar (electron and hole) transport, and interface properties (charge and spin accumulation and depletion) leading to device concepts from *p-n* junction diodes to field-effect transistors, are among the great advantages of semiconductors over other candidates for spintronic materials. By allowing for the active control and manipulation of carrier spin and charge by electric and magnetic fields as well as by light, semiconductor spintronics creates the potential for an integrated magneto-optoelectronic technology.

On the other hand, in this class of materials the Diluted Magnetic Semiconductors (DMS) have attracted considerable attention of the scientific community, owing to them unique properties and possibility to make a sizeable break in ‘’spintronics’’. One of the primary interests in heterostructures containing layers of DMS is due to the large magnetic tuning of the DMS band gap, which caused by exchange interactions between free carriers and magnetic Mn^{2+} ions. On applying an external magnetic field, the band edges in such semiconductor undergo a huge spin splitting due to the *sp-d* exchange between carriers and localized magnetic ions, while the splitting in the nonmagnetic layers is much smaller.

Relying on these properties of the DMS materials Zutic and Fabian have proposed two novel types of spintronic-devices: a magnetic *p-n* diode and a magnetic bipolar transistor (MBT) [1-7]. In these works they demonstrated that the presence of an external magnetic field and nonequilibrium spin inside the junction could allow generating spin-polarized current and some other spin-related phenomena may appear in such structures. Moreover, such spintronic-devices can be used as optical detectors of spin-injection carriers from magnetic to

nonmagnetic semiconductors (spin Light Emitting Diodes) [8, 9]. However, until now no experimental evidences of existing of such devices have been presented.

The main goal of the present work is to fabricate various types of spintronic-devices such as the magnetic *p-n* junction, magnetic bipolar transistor, Spin Superlattice structure based on the DMS material using the Molecular Beam Epitaxy (MBE) technique. The presence of exponential and giant magnetoresistance, spin-voltaic, and spin-valve effects which are expected to be significant in such structures has been investigated by the magneto-optical and magneto-transport measurements in this work.

The thesis is organised as follows. It starts from presenting some basics of the semiconductor theory, reviewing the fundamentals Diluted Magnetic Semiconductors materials. In the second chapter, the detailed description of our experimental setup including some physical aspects of the experiment itself will be presented. The third and fourth chapters are devoted to the magnetic *p-n* junction and magnetic bipolar transistor and experimental results of the magneto-transport and magneto-optical measurements performed in such structures. Chapter 5 describes the magneto-optical and magneto-transport results, which were performed in modulation doped Spin Superlattice structure and in its more simple construction such as Single Diluted Magnetic Semiconductor Quantum Well. Finally, the thesis is summarized and conclusions are presented.

Chapter 1. Introduction

1.1 Spintronic state of the art

A generic semiconductor spintronic scheme involves three steps: injection of nonequilibrium spins into a semiconductor; spin storage, manipulation, and transfer; and spin detection.

Spin injection was historically first accomplished optically by illuminating a semiconductor with circularly polarized light [10]. Electrical spin injection into semiconductors, while predicted theoretically already in the 1970s [11], has been demonstrated only recently [12] and realized as an injection from a magnetic semiconductor [9, 13, 14], a ferromagnetic metal [15-17], and a ferromagnetic metal/tunnel barrier contact [18-22]. After the first demonstration of spin injection over several microns in intrinsic GaAs [23] and even up to 100 μm in *n*-doped GaAs [24] observed at low temperatures semiconductor spintronics has gained a strong boost.

In one's turn traditionally spin in semiconductors has been detected using various optical methods. As an example, observation of spin using circular polarization of the recombination light can be mentioned [10]. On the other hand, to our best knowledge only a few attempts are known to detect nonequlibrium spin in semiconductors using electrical methods. All of them rely on spin-charge coupling realized either as spin-dependent Schottky barrier transport [25, 26] or as magnetoresistance [27] and galvano-voltaic [28] effects.

Closely following the experimental progress major theoretical efforts have been dedicated to understanding electrical spin injection into semiconductors [29–35] and investigating fundamental issues of spin-polarized transport in semiconductors [1-4, 10, 36–39]. Moreover, various spintronic-device architectures for possible technological applications have been proposed. Some of them are related to spin field-effect transistors [40–42] where the source and drain are ferromagnetic electrodes serving to inject and detect spin which is transported in a (typically) nonmagnetic channel. While other authors proposed spintronics device schemes based on heterostructure spin filters [43–52], spin polarization detectors [53], resonant tunneling diodes [54], unipolar magnetic diodes [55], quantum-interference mesoscopic schemes [56, 57], various spin electromagnet sources [28, 58–61], and magnetic bipolar diodes [3, 5, 62] and transistors [6, 7]. However, attempts to fabricate

electrical devices, with electrical spin injection and its detection were unsuccessful; the effects which have been demonstrated so far are limited to the order of 1% or less.

1.2 Molecular Beam Epitaxy

The successful growth of Molecular Beam Epitaxy (MBE) layers and structures involving Diluted Magnetic Semiconductors has opened a great possibility for fabrication of modern spintronic-devices. All samples used in the present work have been grown using the MBE technique. MBE is an ultra-high vacuum (UHV) technique for the crystal growth of thin epitaxial structures, such as semiconductors, isolators and metals. Effusion cells are used to sublimate source material, which produce a material flux of molecules and atoms in the UHV growth chamber (Fig. 1.1). The molecules, which impinge on a heated substrate placed in the chamber, are adsorbed and contribute to the epitaxial growth via reactions with the outermost atomic layers of the substrate surface. Mechanical shutters in front of the effusion cells are used to temporarily interrupt the material flow of the constituent elements of a growing film and of the doping materials. This enables the ordered growth of high-quality crystalline layers and complex heterostructures with precise control of the composition, doping concentration, and hetero-interfaces, which can be abrupt on the atomic scale.

Electronic and optical applications of epitaxial structures require extreme efforts to ensure the purity of the crystal because small densities of unintentional impurities strongly affect the material properties. For this reason, source material with a purity of 99.99999% is used. In addition, MBE growth is carried out in UHV. Under this condition, the rate of residual gas molecules impinging on the substrate is at least five orders of magnitude smaller than the beam flux.

Today, the MBE technique is used for the epitaxial growth of a wide range of different materials and heterostructures with interesting physical properties and applications in modern devices. However, when the MBE growth is used for fabrication of heterostructures consisting of different material systems, one has to consider that constituent elements of one material might be impurities for another. In order to achieve the highest possible quality of both material systems, the respective layers are grown in different growth chambers.

Figure 1.1 shows the sketch of a growth chamber of the MBE machine EPI-620 used in the present work. A He cryopump and liquid nitrogen (LN_2) cryogenic traps surrounding the inner walls of the UHV chamber, keep the system base pressure low ($< 10^{-10}$ torr). Substrates mounted on a substrate holder (molybdenum-block) are handled in situ with the substrate manipulator of the growth chamber. The substrate is radiation-heated from the backside and its temperature can be measured using a thermocouple, which is in a thermal contact with the block and shielded from the radiation of the heater. Molecular fluxes are monitored with an ion gauge, positioned in front of the manipulator.

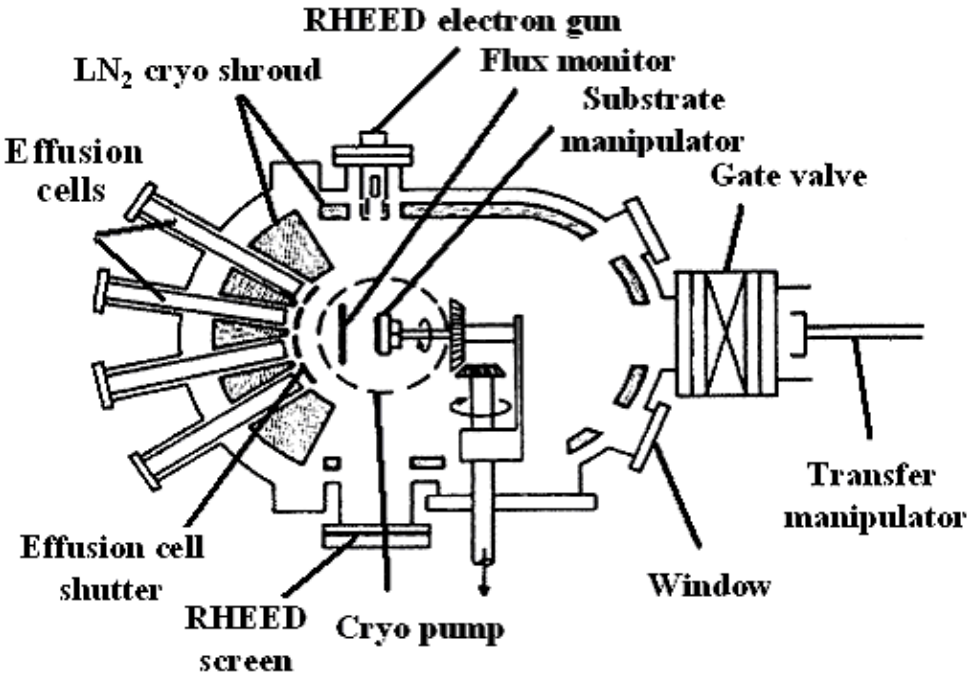

Figure 1.1 Schematic illustration of a MBE growth chamber.

An advantage of the UHV environment is that the MBE growth can be controlled *in situ* by surface sensitive diagnostic methods such as reflection high-energy electron diffraction (RHEED), low-energy electron diffraction and scanning tunneling microscopy. This has led to a good understanding of the microscopic surface processes during epitaxial growth and resulted in a tremendous improvement of the process control.

RHEED is the standard technique used for monitoring MBE growth on a surface in real time. A RHEED measurement consists of the electron beam from an electron gun (Fig. 1.1), which is directed towards a substrate surface at a glancing angle typically

ranging from 0.5° to 3° to enable forward scattering of the beam. A fluorescence RHEED screen is used to visualize the diffracted electrons. Using the RHEED measurements one can obtain the following useful information.

I. Surface morphology. The diffracted beam visualized on the RHEED screen shows patterns which are characteristic for the surface morphology. As can be seen in Fig. 1.2 an atomically smooth interface (2D) corresponds to a streaky RHEED pattern, while three-dimensional islands or a rough surface morphology (3D) causes spotty features in RHEED images. The shape, symmetry, intensity, and width of superimposed streaky and spotty features give additional information on the nature of the surface morphology. A key observation by Cho [63] is the change of surface morphologies from initially 3D to quasi 2D during the growth of a GaAs buffer on a GaAs substrate (timescale from left to right in Fig. 1.2). This demonstrates that the lateral growth rate of islands on a substrate can exceed the vertical growth rate leading to a smoothing of the surface.

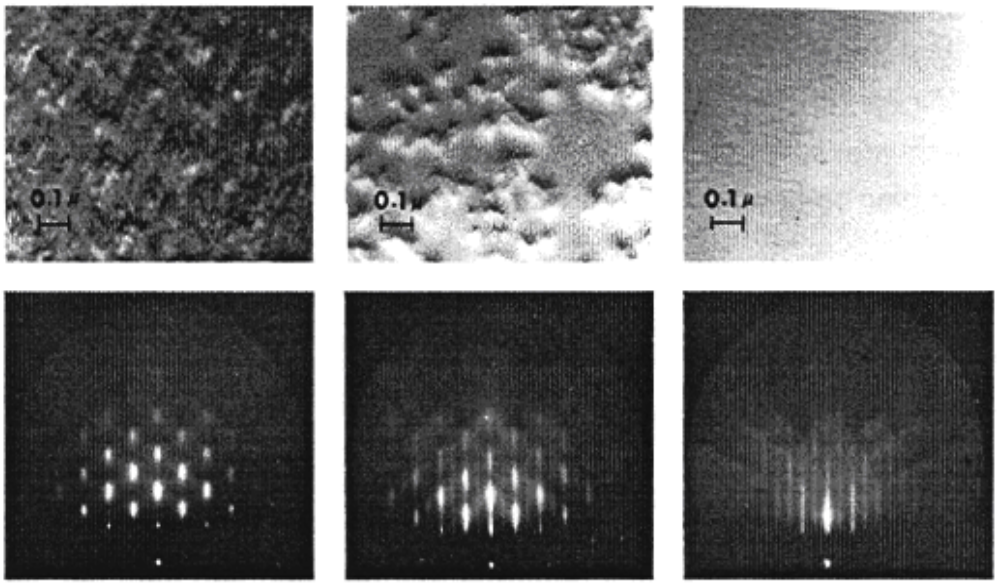

Figure 1.2 The correlation between the RHEED pattern and the morphology of the GaAs surface as a function of growth time (from left to right). The initial 3D surface giving rise to a spotty pattern due to electron transmission through 3D features. The more 2D surface giving rise to the commonly observed RHEED streaks [63].

II. Surface reconstruction. Another important piece of information gathered from RHEED images is the surface reconstruction, which depends on the growth conditions, i.e., the flux ratio and substrate temperature. The lateral periodicity of the surface reconstruction is often one, two, or four unit-cells wide, and, thus, causes RHEED

patterns with zero, one, and three minor diffraction rods, respectively. The right-hand RHEED image in Fig. 1.2 shows the characteristic pattern of the (2 x 4) reconstructed GaAs (001) surface, observed in the $(1\,1\,0)$ azimuth. The surface reconstruction can be uniquely identified from the patterns of the $(1\,1\,0)$, (110), and (100) azimuths.

III. RHEED oscillations. At last, the intensity of the specular beam, which exhibits oscillatory behavior (Fig. 1.3 (a)) can also hold an important piece of information. RHEED oscillations are observed in layer-by-layer growth. When one monolayer (ML) high islands nucleate on an atomically smooth surface (Fig. 1.3 (b)), the specular intensity decreases because of the increasing disorder of the surface. When one ML high islands cover about half of the surface area, the specular intensity starts to recover because the islands coalescence and vacant areas between them are filled until the growth of one ML is completed. Thus, a smooth interface is recovered and new islands can start to nucleate, hence the period of RHEED oscillations is indicative for the growth rate. In a conventional MBE process, RHEED oscillations are always damped (see Fig. 1.3 (a)). This shows that new islands nucleate before one full ML is completed, i.e., the surface roughness increases and can be up to several MLs.

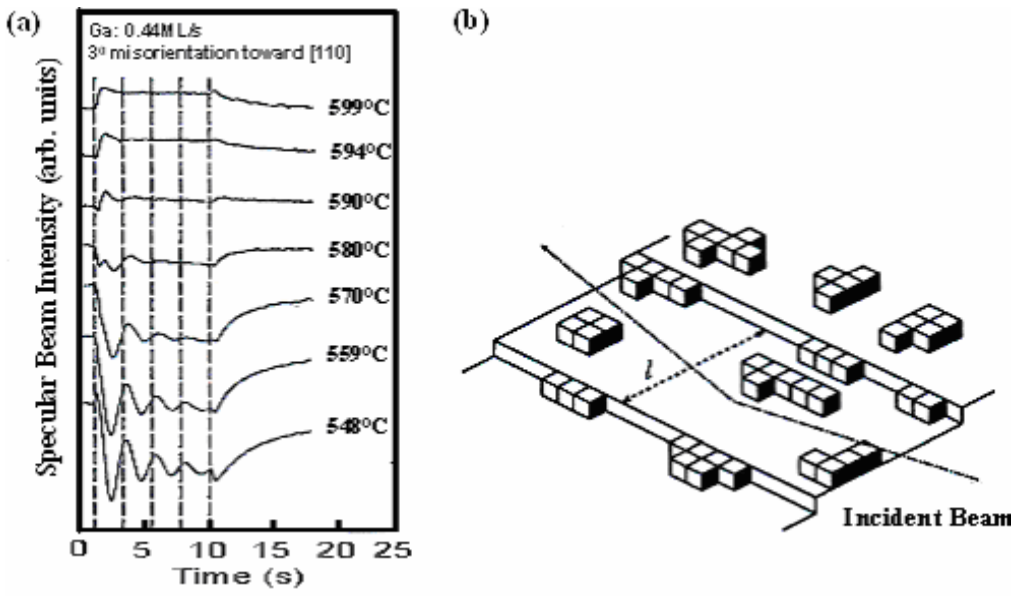

Figure 1.3 (a) Specular beam intensity during GaAs MBE on 3^0 misoriented (001) substrate as a function of time, at various substrate temperatures, showing RHEED oscillations at low substrate temperatures. (b) Schematic illustration of growth on a vicinal substrate. Adatoms are preferentially incorporated at the step edges. However, one ML high islands nucleate on a terrace when the diffusion length is limited at low substrate temperature, thus contributing to the oscillatory modulation of the intensity of the specular beam.

1.3 Basic properties of CdTe and CdMnTe

1.3.1 Band structure of CdTe

CdTe is one of the basic compounds of II-VI group semiconductors used for fabrication different kinds of electrical devices. CdTe crystallizes in zinc blende (ZB) structure shown in Fig. 1.4. The ZB structure is the stable form for bulk single crystals of CdTe at atmospheric pressure. This structure belongs to the cubic space group and consists of two interpenetrating face center cubic lattices offset from one another by one-fourth of a body diagonal as shown in Fig. 1.4.

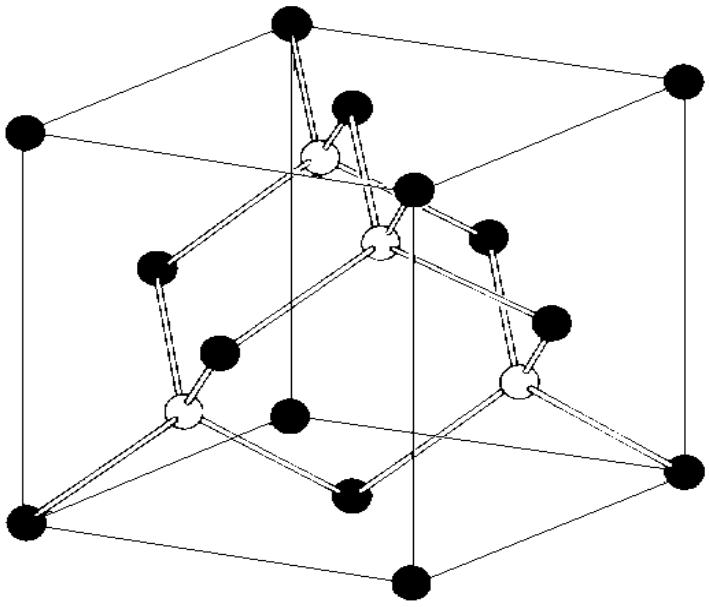

Figure 1.4 The unit cell of CdTe possesses zinc blende structure.

There are four molecules per unit cell, the coordinates of the Te atoms are (000), $(0\frac{1}{2}\frac{1}{2})$, $(\frac{1}{2}0\frac{1}{2})$, and $(\frac{1}{2}\frac{1}{2}0)$ and those of the Cd atoms are $(\frac{1}{4}\frac{1}{4}\frac{1}{4})$, $(\frac{1}{4}\frac{3}{4}\frac{3}{4})$, $(\frac{3}{4}\frac{1}{4}\frac{3}{4})$, and $(\frac{3}{4}\frac{3}{4}\frac{1}{4})$. As a result every atom of Cd is surrounded tetrahedrally by four atoms of Te and opposite. The distance between them is $\sqrt{3}\frac{a}{4}$. The cubic lattice parameter (a) at room temperature is 6.481 Å [64]. This value can be changed due to deviations from stoichiometry, but usually belongs to the interval 6.482 Å ± 0.001 Å.

The band structure of a crystalline solid, i.e., the energy-momentum (***E-k***) relationship is usually obtained by the solution of the Schrödinger equation of an approximate one-electron problem. One of the most important theorems basic to band structure is the Bloch theorem, which states that if a potential energy ***PE(r)*** is periodic with the periodicity of the lattice, then the solutions $\phi_k(r)$ of the Schrödinger equation:

$$\left[\left(-\frac{\hbar^2}{2m}\nabla^2 + PE(r)\right)\right]\phi_k(r) = E_k\phi_k(r) \tag{1.1}$$

are of the form

$$\phi_k(r) = e^{jkr}U_k(r) = \text{ Bloch function} \tag{1.2}$$

where $U_k(r)$ is periodic in **r** with the periodicity of the direct lattice, $\hbar$ is reduced Planck constant, E is the kinetic energy, ϕ is the wave function of the particle.

From the Bloch theorem one can show that the energy E_k is periodic in the reciprocal lattice, i.e., $E_k = E_{k+g}$, where g is general reciprocal lattice vector. Thus, to label the energy uniquely it is sufficient to use only ***k***'s in a primitive cell of the reciprocal lattice. The standard convention is to use the Wigner-Seitz cell in the reciprocal lattice. This cell is called the Brillouin zone or the first Brillouin zone. It is thus evident that we can reduce any momentum ***k*** in the reciprocal space to a point in the Brillouin zone where any energy state can be given a label in the reduced zone scheme.

The energy bands of solids have been analyzed using a variety of computer methods. For semiconductors two most frequently used methods are the orthogonalized plane wave method [65] and the pseudopotential method [66]. Results of studies of the energy band structure of CdTe are shown in Fig. 1.5 [67].

As can be seen the conduction band minimum and the valence band maximum are at the **Γ** point (at **k** = 0), classifying CdTe as a direct gap material. Reasonable agreement between the calculated and experimental results provides a firm basis for interpretation of the band structure of CdTe. The valence band is associated with the *5s* and *5p* atomic orbitals of Cd and Te. Neglecting spin, the valence band is composed of four subbands. The fourth or lowest valence band state is $\mathbf{\Gamma_1}$ level primarily associated with *s*-orbitals of Te. The three upper bands are degenerate at **k** = 0 and form the upper edge of the band. The higher valence band states consist largely of the *p*-electron states of Te and a small admixture of *s*-electron

states of Cd. For $\mathbf{k} \neq 0$ the threefold degeneracy at the top of the band is split into a twofold degenerate and a nondegenerate band.

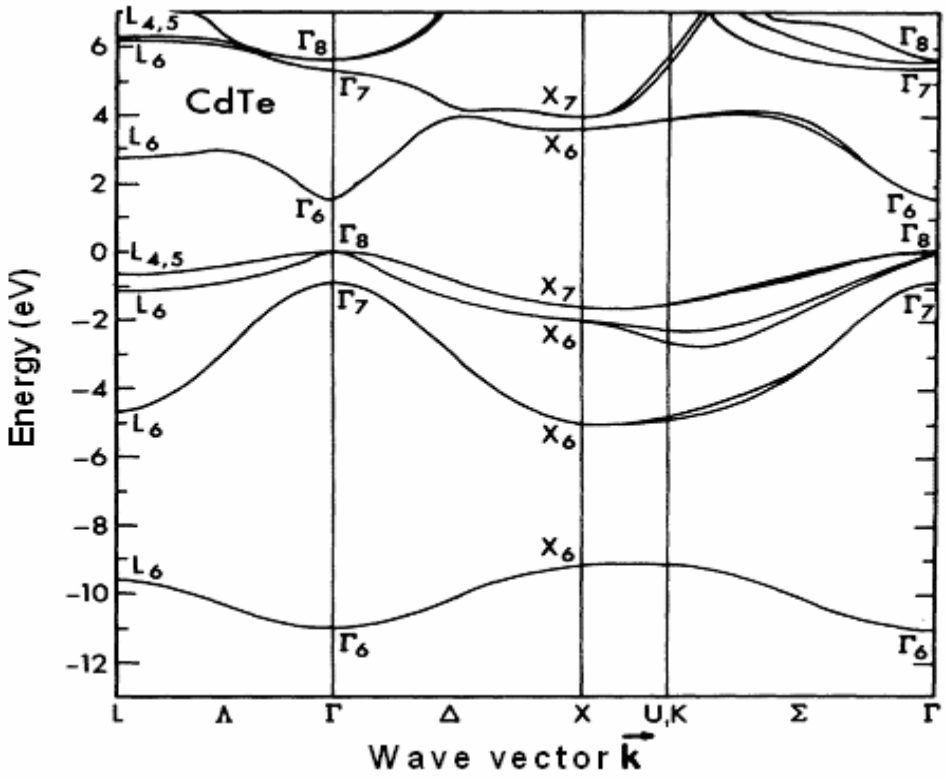

Figure 1.5 Electronic band structure of CdTe.

As shown in Fig. 1.5 the two top valence bands $\mathbf{\Gamma_8}$ can be approximately fitted by two parabolic bands with different curvatures: the heavy-hole band having smaller $\frac{\partial^2 E}{\partial k^2}$ and the light-hole band having larger $\frac{\partial^2 E}{\partial k^2}$. The separation between the energy of the lowest conduction band and that of the highest valence band is called the band gap, $\boldsymbol{E_g}$, which is one of the most important parameters in semiconductor physics. Literature values for the band gap energy of CdTe at room temperature vary from 1.39 [68] to 1.547 eV [69]. From magneto-absorption measurements, it was found to be 1.606 eV at 1.6 K [70]. The electron effective mass in CdTe was reported to be 0.096 m_0. Values of 1 m_0 and 0.1 m_0 were obtained for the heavy and light hole masses, respectively [71]. The Lande factor – g of electron (hole) was found experimentally to be -1.67 (0.3). The dielectric constant of CdTe was obtained 10.4 [72].

1.3.2 Basic properties of $Cd_{1-x}Mn_xTe$

Recently Diluted Magnetic Semiconductors, mainly $A^{II}_{1-x}Mn_xB^{VI}$, have attracted much interest due to their potential applications in spintronics. There are three main aspects of DMS properties that make such alloys interesting subject for spintronics. The first of these aspects concerns semiconducting properties: the parameters determining the band structure of the material such as the energy gap can be varied by changing appropriately the Mn^{2+} mole fraction in the crystal. Similarly, lattice constants can be tuned by varying the composition of DMSs, where lattice matching is of obvious importance. Because of the tunability of their lattice parameters and their energy gaps, the $A^{II}_{1-x}Mn_xB^{VI}$ alloys are excellent candidates for the preparation of quantum wells, superlattices and other material systems that involve band-gap engineering. Secondly, magnetic properties of DMS encompass a very broad spectrum of behavior, including paramagnetic, spin-glass and antiferromagnetic properties. The substitutional Mn atoms in the $A^{II}B^{VI}$ lattice are also characterized by highly efficient electroluminescence, which makes dilute $A^{II}_{1-x}Mn_xB^{VI}$ alloys important in the context of optical flat panel display applications. Thirdly, the exchange interaction between the localized magnetic moments of Mn^{2+} and the conduction and/or valence band electrons results in a series of features which are unique to DMS. The presence of localized magnetic ions in these semiconductor alloys leads to an exchange interaction between the *sp* band electrons and the *d* electrons associated with Mn^{2+}, resulting in extremely large Zeeman splittings of electronic (band and impurity) levels. This selective amplification of spin-dependent properties leads to dramatic new effects, such as the giant Faraday rotation, the magnetic-field-induced metal-insulator transition, and the formation of bound magnetic polarons.

As mentioned above the most extensively studied and most thoroughly understood DMS materials are the $A^{II}_{1-x}Mn_xB^{VI}$ alloys in which a fraction of the group II sublattice is replaced at random by Mn. There are good reasons for this particular choice. Firstly, Mn^{2+} can be incorporated in sizable amounts in the $A^{II}B^{VI}$ host without affecting substantially the crystallographic quality of the resulting material (up to nearly 80% of Mn can be accommodated in CdTe). Secondly, Mn^{2+} possesses a relatively large magnetic moment (s = 5/2), characteristic of a half-filled *d* shell. Thirdly, Mn^{2+} is electrically neutral in $A^{II}B^{VI}$ hosts and as a result it constitutes neither accepting nor donating centers.

A. $Cd_{1-x}Mn_xTe$ alloy: lattice parameter and band structure

$Cd_{1-x}Mn_xTe$ is one of the most intensively studied and thus best known DMS. Similar CdTe, $Cd_{1-x}Mn_xTe$ crystallizes in the zinc blende structure (see Fig. 1.4) in the range $0 < x \leq 0.77$. The lattice parameter of $Cd_{1-x}Mn_xTe$ obeys Vegard's law [73] and can be described by the following equation:

$$a = (1-x)a_{II-VI} + xa_{Mn-VI}, \tag{1.3}$$

where a_{II-VI} and a_{Mn-VI} are lattice parameters of the binary constituents (e.g., of CdTe and of the "hypothetical" zinc blende MnTe).

Thus, from equation (1.3) it clearly follows that the lattice parameter decreases linearly with increasing Mn content (see Fig 1.6).

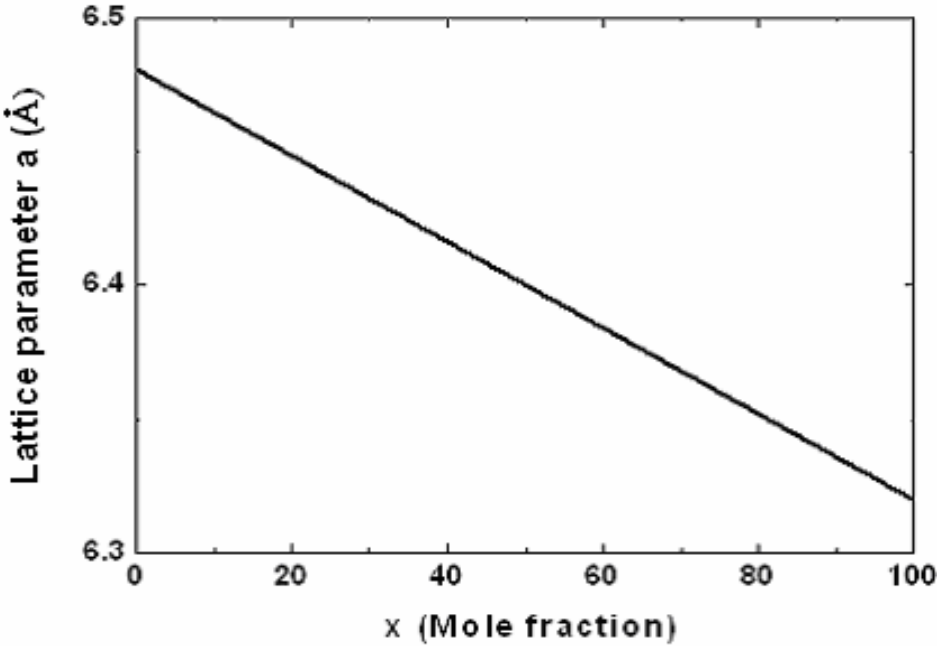

Figure 1.6 Lattice parameter as a function of Mn mole fraction x in $Cd_{1-x}Mn_xTe$.

In the absence of an external magnetic field the band structure of the $A^{II}_{1-x}Mn_xB^{VI}$ alloys closely resembles that of the $A^{II}B^{VI}$ materials having the same crystal structure. In particular, CdMnTe is a direct-gap semiconductor with the band extrema at the **Γ** point. Because Mn is substituted by Cd in the CdTe lattice the energy gap increases to the

point that the originally opaque material becomes transparent to visible light. The variation of E_g in $Cd_{1-x}Mn_xTe$ is found to be linear as a function of composition and can be expressed as:

$$E_g\,(300\text{ K}) = (1.528 + 1.316x)\text{ eV}, \tag{1.4}$$

$$E_g\,(4.2\text{ K}) = (1.606 + 1.592x)\text{ eV}, \tag{1.5}$$

for $x < 0.77$ [74].

B. *Sp-d* exchange interaction and its influence on the Zeeman splitting in DMS materials

When a semiconductor contains localized magnetic moments, its band structure will be modified by the exchange interaction of these moments (i.e., the $3d^5$ electrons) with band (i.e., *sp*) electrons. It is because of the *sp-d* exchange that magneto-optical and high field magneto-transport properties of DMS are qualitatively different from those observed in their nonmagnetic counterparts. The *sp-d* exchange interaction influences physical phenomena which involve electrons in the conduction and valence bands (e.g., magneto-transport, interband and intraband magneto-optics), exciton levels (e.g., Faraday rotation), and impurity levels (e.g., bound magnetic polaron, giant negative magnetoresistance, metal-semiconductor transition). Such interaction is expressed formally by a new Kondo-like exchange term H_{ex} to the original Hamiltonian $H_{0,}$ so that the total Hamiltonian H can be represent by equation (1.6):

$$H = H_0 + H_{ex} = H_0 + \sum_{R_i} J(\vec{r} - \vec{R}_i) S_i \cdot s\,, \tag{1.6}$$

where S_i and s are the spin operators for the Mn^{2+} ion and for the band electron, $J(r\text{-}R_i)$ is the electron-ion *sp-d* exchange coupling constant, and r and R_i are the coordinates of the band electron and of the Mn^{2+} ion, respectively. The summation is only over the lattice sites occupied by the Mn^{2+} ions in the system.

The difference between the present case and a nonmagnetic semiconductor lies in the presence of the ion-carrier exchange Hamiltonian H_{ex}. The nonmagnetic semiconductor in the presence of an external magnetic field is described through appropriate Hamiltonian, which is

denoted H_0 and contains all information required to describe the semiconductor with the exception of the *sp-d* exchange contribution [73].

Two convenient approximations can be made to simplify H_{ex}. Firstly, since the electronic wave function is very extended, so that the electron sees a large number of magnetic ions at any time, so we can make use of the molecular field approximation, replacing S_i, by the thermal average $\langle S \rangle$ taken over all Mn^{2+} ions. For paramagnetic systems, if the applied magnetic field B is in the z direction, $\langle S \rangle = \langle S_z \rangle$. Secondly, because the electronic wave function spans a large number of lattice sites, we can replace $J(r-R_i)$ by $xJ(r-R)$, where R denotes the coordinate of every site of the cation sublattice, with the summation now carried out over all R. We are thereby expressing in terms of the virtual crystal approximation. With these assumptions, we obtain:

$$H_{ex} = s_z \langle S_z \rangle x \sum_R J(\vec{r} - \vec{R}), \tag{1.7}$$

with the summation extending over all cation sites, and x denotes the manganese mole fraction.

On the other hand, the thermal average of the Mn spin component in z-direction $\langle S_z \rangle$ is directly related to the magnetization of Mn ions, which characterized magnetic system in a presence of magnetic field. The form of this dependence can be expressed by equation (1.8):

$$M(x, B, T) = -g_{Mn} \mu_B N_0 x \langle S_z \rangle, \tag{1.8}$$

where μ_B is the Bohr magneton, N_0 is the number of unit cells per unit volume, g_{Mn} is factor Lande of Mn ions ($g_{Mn} = 2$).

In a case of low Mn content, when $x < 0.01$, the Mn^{2+} spins can be regarded as isolated, i.e., independent from one another.

For $3d^5$ electrons of Mn, $\langle S_z \rangle = -Sf_{norm}$, where S is a spin value of Mn ion ($S = \frac{5}{2}$) and f_{norm} denotes the normalized magnetization.

For non-interacting magnetic moments:

$$f_{norm} = B_S\left(\frac{g_{Mn}\mu_B BS}{k_B T}\right), \tag{1.9}$$

where k_B is Boltzmann constant, B is the applied magnetic field, T is temperature, B_S is the Brillouin function for a spin $S = \frac{5}{2}$:

$$B_S(x) = \frac{2S+1}{2}\coth\frac{2S+1}{2}x - \frac{1}{2}\coth\frac{x}{2}. \tag{1.10}$$

Basing on equations (1.8), (1.9) and (1.10), the magnetization can be rewritten in a form of equation (1.11):

$$M(x,B,T) = -g_{Mn}\mu_B N_0 x\langle S_z\rangle = g_{Mn}\mu_B N_0 x S B_s\left(\frac{g_{Mn}\mu_B SB}{k_B T}\right). \tag{1.11}$$

For DMS of arbitrary x, the magnetization M cannot be expressed by the standard Brillouin function because of the Mn-Mn interactions. However, there still is a qualitative similarity between the observed M versus B behavior and the Brillouin function. Based upon this resemblance, in Ref. [75] authors proposed an empirical but very useful expression by replacing the magnetic ion mole fraction x and temperature T in Eq. (1.11) by effective values x_{eff} and T_{eff}, correspondingly:

$$M(x,B,T) = g_{Mn}\mu_B N_0 x_{eff} S B_s\left(\frac{g_{Mn}\mu_B SB}{k_B(T_{eff})}\right), \tag{1.12}$$

where x_{eff} and $T_{eff} = T + T_0$ are phenomenological fitting parameters.

Most of the electrical and optical phenomena of interest in $A^{II}B^{VI}$ materials and their alloys involve electrons and holes in the vicinity of the **Γ** point. Thus, in order to understand the vast majority of the effects involving *sp-d* exchange, it is sufficient only to consider how the exchange affects the top of the valence band and the bottom of the conduction band.

In Ref. [74-76] authors calculated energy states of conduction and valence band electrons by the $k \cdot p$ perturbation method for a case of wide-gap DMS material

($Cd_{1-x}Mn_xTe$). In this case the calculated splitting of transition energies was shown to be proportional to the following expression:

$$\Delta E_{sp-d} = J_{sp-d} N_0 x \langle S_z \rangle , \tag{1.13}$$

where J_{sp-d} is exchange integral, which in a case of $Cd_{1-x}Mn_xTe$ for conduction band electrons is $J_{s-d} N_0 \equiv \alpha N_0 = 0.22$ eV and for valence band holes is $J_{p-d} N_0 \equiv \beta N_0 = -0.88$ eV.

Thus, the total spins splitting (ΔE), which is a sum of "intrinsic" Zeeman splitting in the host material ($\Delta E_Z = g\mu_B B$), and the "giant" Zeeman splitting (ΔE_{Sp-d}), due to the *sp-d* exchange interaction (eq. (1.13)) have a form of equation (1.14):

$$\Delta E = \Delta E_Z + \Delta E_{sp-d} = g\mu_B B + J_{sp-d} N_0 x S B_S \left(\frac{S g_{Mn} \mu_B B}{k_B (T + T_0)}\right) = g_{eff} \mu_B B , \tag{1.14}$$

where g_{eff} is the effective electron *g* factor in DMS materials, which depends on magnetic field:

$$g_{eff}(B) = g + \frac{\left(J_{sp-d} N_0 x S B_S \left(\frac{S g_{Mn} \mu_B B}{k_B (T + T_o)}\right)\right)}{\mu_B B} . \tag{1.15}$$

The corresponding energy levels at the center of the Brillouin zone for wide-gap DMS in the presence of a magnetic field are shown in Fig. 1.7.

The splitting is qualitatively identical to ordinary spin splitting which takes place in nonmagnetic semiconductors (two spin levels for $\mathbf{\Gamma_6}$, four for $\mathbf{\Gamma_8}$), and in this sense the exchange contribution can be naturally absorbed into the concept of an effective *g* factor whenever the concept of a *g* factor is meaningful. The situation differs from the case of nonmagnetic semiconductors primarily by the fact that the magnitude of spin splitting is extremely large that its behavior is determined primarily by the properties of the magnetization. In Ref. [77] authors demonstrated that the total splitting in bulk CdMnTe can reach about 100 meV. However, the selection rules governing transitions between the levels shown in Fig. 1.7 remain the same as between spin levels of a nonmagnetic semiconductor.

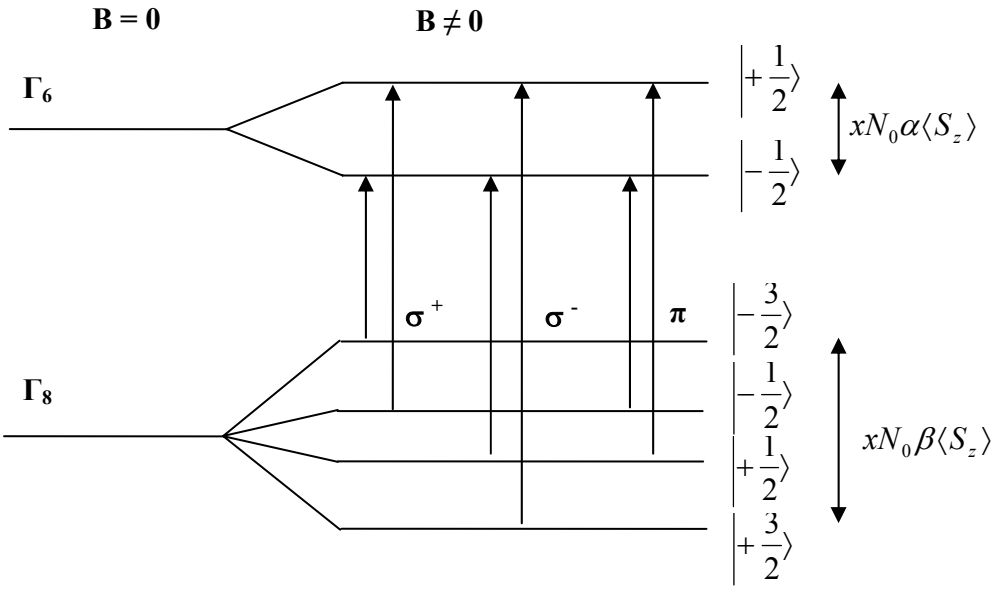

Figure 1.7 A schematic picture of the spin splitting of the top of the valence band (Γ_8) and the bottom of the conduction band (Γ_6) for a wide-gap $Cd_{1-x}Mn_xTe$ in a presence of magnetic field. Arrows show optical transitions allowed in the dipole approximation for various light polarizations.

1.3.3 Impurity doping of CdTe and CdMnTe

In semiconductor technology, doping refers to the process of intentionally introducing impurities into an extremely pure (also referred to as intrinsic) semiconductor in order to change its electrical properties. Either these impurities can be unintentional due to lack of control during the growth of the semiconductor or they can be added on purpose to provide free carriers in the semiconductor. The generation of free carriers requires not only the presence of impurities, but also that the impurities give off electrons to the conduction band in which case they are called *donors* or that they give off holes to the valence band in which case they are called *acceptors* (since they effectively accept an electron from the filled valence band). A semiconductor doped with impurities, which are ionized (meaning that the impurity atoms either have donated or accepted an electron), will therefore contain free carriers. *Shallow impurities* are impurities, which require little energy - typically around the thermal energy or less - to ionize. *Deep impurities* require energies larger than the thermal energy to ionize so that only a fraction of the impurities present in the semiconductor contributes to free carriers. Deep impurities, which are more than five times the thermal energy away from either band edge, are very unlikely to ionize. Such impurities which are also called *traps* can be

effective recombination centers in which electrons and holes fall and annihilate each other. Apart from intentional introduction of electrically active impurities into a host crystal, any doping process may induce undesired formation of deep defects. The presence of defects strongly influences the properties of the material and, eventually, of devices made out of it.

Ionized donors provide free electrons in a semiconductor, which is then called *n-type*, while ionized acceptors provide free holes in a semiconductor, which we refer to as being a *p-type* semiconductor.

If a semiconductor contains both shallow donors and shallow acceptors it is called *compensated* since equal amounts of donors and acceptors compensate each other, yielding no free carriers. The presence of shallow donors and shallow acceptors in a semiconductor cause the electrons given off by the donor to fall into the acceptor state, which ionizes the acceptor without yielding a free electron or hole. The resulting carrier density in compensated material, which contains both shallow donors and shallow acceptors, is approximately equal to the difference between the donor and acceptor concentration.

In a case of cadmium telluride (CdTe), grown by the MBE technique, *n*-type CdTe films can be fabricated using Indium dopants, up to carrier concentrations exceeding 10^{18} cm^{-3} without any compensation effects [78-88]. It was shown in Refs. [87, 88] that the carrier concentration in CdTe films can be effectively tuned by adjusting the In flux and Cd/Te flux ratio. Moreover, in a wide concentration range the activation efficiency of Indium doping is close to 100%. Another approach to obtain the *n*-type doping in CdTe is to use halogens such as chlorine, bromine and iodine, which play as alternative dopants. Halogen atoms form hydrogen-like donors on Te sites, but elemental halogens are not compatible with an MBE process. That's why; usually one can use solid compounds such as $ZnCl_2$, $ZnBr_2$ and ZnI_2. This choice of the dopant source material is due to the vapour pressure of zinc halogenide is much less than the vapour pressure of elemental halogens, and the incorporation of a halogen atom might be enhanced by the incorporation of the zinc atom. In this case a maximum Hall concentration was 2×10^{18} cm^{-3} for the photoassisted use of $ZnCl_2$ [89], 2.8×10^{18} cm^{-3} for $ZnBr_2$ [90], and 8×10^{18} cm^{-3} for ZnI_2 [91]. In general, a halogen doping depends much less critically on growth parameters than, for example, it does in a case of In doping.

In Ref. [91] authors compared properties of CdTe and $Cd_{1-x}Mn_xTe$ films doped with ZnI_2 and In. Thus, it was demonstrated that replacing Indium by Iodine results in much higher electron concentration in CdTe layers (Fig 1.8 (a)). As can be seen in Fig. 1.8 (b), in contrast to Indium-doped samples in which electron concentration quickly decreases with an increasing manganese content, Iodine doping of $Cd_{1-x}Mn_xTe$ enables to keep a high doping

level in samples rich in manganese [92]. Such metallic conductivity can be expected in samples with Mn molar fraction up to $x = 0.3$. Similar results can be obtained in $Cd_{1-y}Mg_yTe$ ternary alloy. For Iodine dopant, a free carrier density of 1×10^{17} cm^{-3} for $y = 0.37$ and 1.5×10^{18} cm^{-3} for $y = 0.2$ can be obtained. This drop of free carrier concentration in samples with higher Mg or Mn concentrations may be attributed to the formation of deep donor states. Moreover, comparing *n*-doped CdMgTe and CdMnTe alloys [88], one can conclude that the depth of the deep level seems to be independent of the type of ternary component and depends only on the band gap of semiconductor.

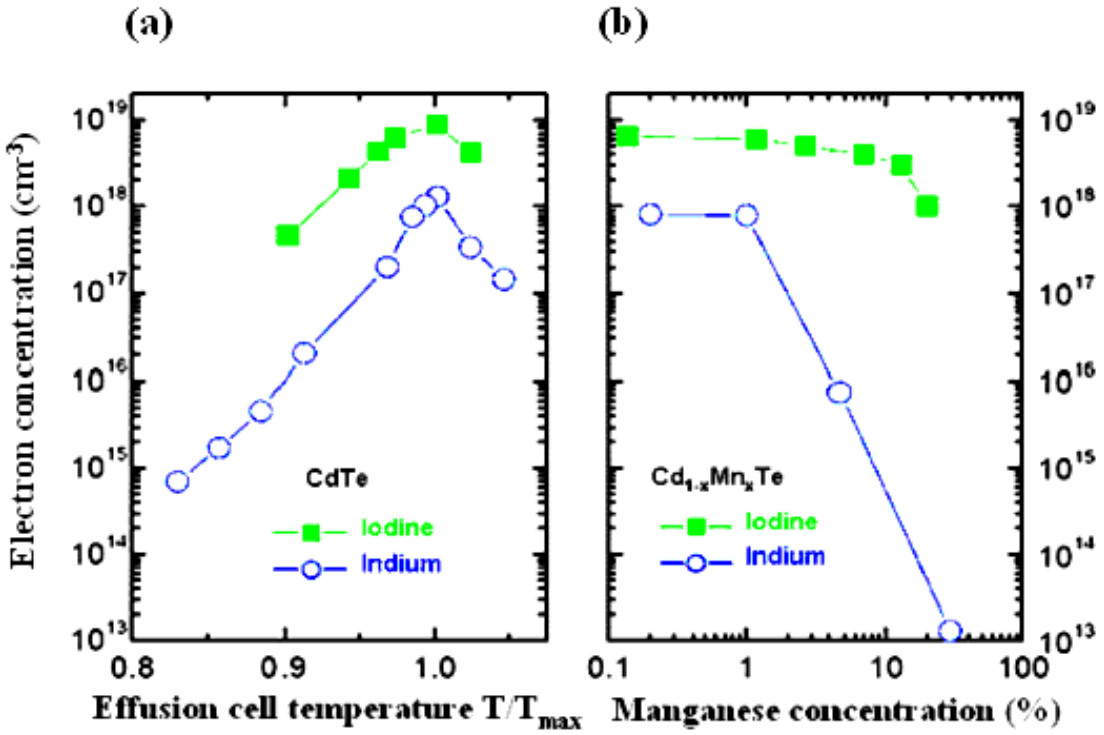

Figure 1.8 Room temperature electron concentration in MBE-grown iodine- and indium-doped (a) CdTe and (b) $Cd_{1-x}Mn_xTe$ layers determined from the Hall effect measurements [91].

There were a lot of attempts to obtain *p*-type ZnTe and CdTe epilayers. In most of works conventional Knudsen cells containing P, As and Sb species have been used to dope CdTe and ZnTe during the MBE growth procedure. The best reported results have been obtained using Sb-doped layers with hole concentration $p\approx5\times10^{18}$ cm^{-3} and $\approx10^{18}$ cm^{-3} for CdTe [93] and ZnTe [94], respectively. Harper *et. al.* [95] suggested a photo-assisted doping and demonstrated that the hole concentration $p = 6.2\times10^{18}$ cm^{-3} can be obtained for CdTe in this case. Dhese *et. al*. [96] and Han *et. al*. [97] showed that the *p*-type doping with nitrogen

can be also obtained using a radio frequency (RF) plasma source. In this case they obtained $p = 1.2\times10^{19}$ cm^{-3} and 2×10^{17} cm^{-3} for ZnTe and CdTe, respectively. Baron *et. al.* [98] presented a detailed study of *p*-type doping of Te-based compounds (CdTe, ZnTe) and alloys (CdMgTe, ZnMgTe and CdZnTe) during the MBE growth, using nitrogen atoms produced by a direct current glow plasma source. According to them *p*-type doping as high as $p\approx10^{20}$ cm^{-3} can be obtained in ZnTe when a number of nitrogen atoms about 1.5×10^{20} cm^{-3} are incorporated into the layer. It is interesting to note that Baron *et. al.* observed a saturation of the doping level with increasing incorporation of nitrogen, but no deep traps were detected even when a large amount of nitrogen was introduced into the layer. Moreover, changing the growth conditions from a Cd overpressure to a Te overpressure, doping level decreases. From this it was concluded that the compensation mechanism was related to the formation of N_2 interstitial defects or complex defects involving metal vacancies in such materials. The highest concentration is $p\approx10^{18}$ cm^{-3} in CdTe. The doping level increases considerably in CdZnTe and ZnMgTe alloys as a function of the Zn content. For identical incorporation of nitrogen (of about 10^{19} cm^{-3}) the highest doping level was 10^{17} cm^{-3} in $Cd_{0.76}Mg_{0.24}Te$ whereas ZnMgTe can be doped up to 3×10^{18} cm^{-3} even for 34% of Mg.

In the present work ZnI_2 Knudsen diffusion cell was used as a donor impurity for fabrication *n*-type semiconductors. At the same time nitrogen and radio frequency (RF) plasma source were used to obtain materials with the *p*-type conductivity. In addition, in order to increase the *p*-type doping efficiency we added a small amount of Zn (about 9%) to CdTe and CdMnTe.

1.4 Semiconductor devices

1.4.1 *P-n* junction

A *p-n* junction plays an important role both in modern electronic applications and in understanding other semiconductor devices. It is used extensively in rectification, switching, and other operations in electronic circuits. *P-n* junction is a key building block for the bipolar transistor and thyristor. Given proper biasing conditions or when exposed to light *p-n* junction also functions as either microwave or photonic device.

The term junction refers to the region where the two regions of the semiconductor meet (Fig 1.9 (a,b)). It can be thought of as the border region between the *p*-type and *n*-type

blocks. *P*-doped semiconductor is relatively conductive. The same is true of *n*-doped semiconductor, but the junction between them is a nonconductor. This nonconducting layer, called the *depletion zone*, occurs because the electrical charge carriers in doped *n*-type and *p*-type semiconductor attract and eliminate each other in a process called *recombination.* By manipulating this nonconductive layer, *p*-*n* junctions are commonly used as diodes: electrical switches that allow a flow of electricity in one direction but not in the other (opposite) direction. This property is explained in terms of the forward-bias and reverse-bias effects, where the term bias refers to an application of electric voltage to the *p*-*n* junction.

Generally, when the *p*- and *n*-type semiconductors as shown in (Fig 1.9 (a)) are joined together (Fig. 1.9 (b)), a part of the electrons, majority carriers in the *n*-doped material, diffuse from the *n*-side to the *p*-side, where their concentration is very low, and a part of the holes, majority carrier in the *p*-side, diffuse in the opposite direction. As holes continue to leave the *p*-side, some of the negative acceptor ions (N_A) near the junction are left uncompensated, since the acceptors are fixed in the semiconductor lattice, whereas the holes are mobile. Similarly, some of the positive donor ions (N_D) near the junction are left uncompensated as the electrons leave the *n*-side. Consequently, a negative space charge forms near the *p*-side of the junction and a positive space charge forms near the *n*-side Fig. 1.9 (c). This space charge region creates an electric field that is directed from the positive charge toward the negative charge, as indicated in the upper illustration of Fig. 1.9 (b). The electric field is in the direction opposite to the diffusion current for each type of charge carrier, the hole diffusion current flows from left to right, whereas the hole drift current due to the electric field flows from right to left. The electron diffusion current also flows from left to right, whereas the electron drift current flows in the opposite direction (Fig. 1.9 (b)).

Moving from a neutral region toward the junction, we encounter a narrow transition region, shown in Fig. 1.9 (c). Here the space charge of impurity ions is partially compensated by the mobile carrier. Beyond the transition region is the completely depleted region, where the mobile density carrier densities are zero. Fig. 1.9 (d) represented the electric field distribution of the *p*-*n* junction in thermal equilibrium.

At thermal equilibrium, that is the steady-state condition at a given temperature without any external excitations, the individual electron and hole current flowing across the junctions are identically zero.

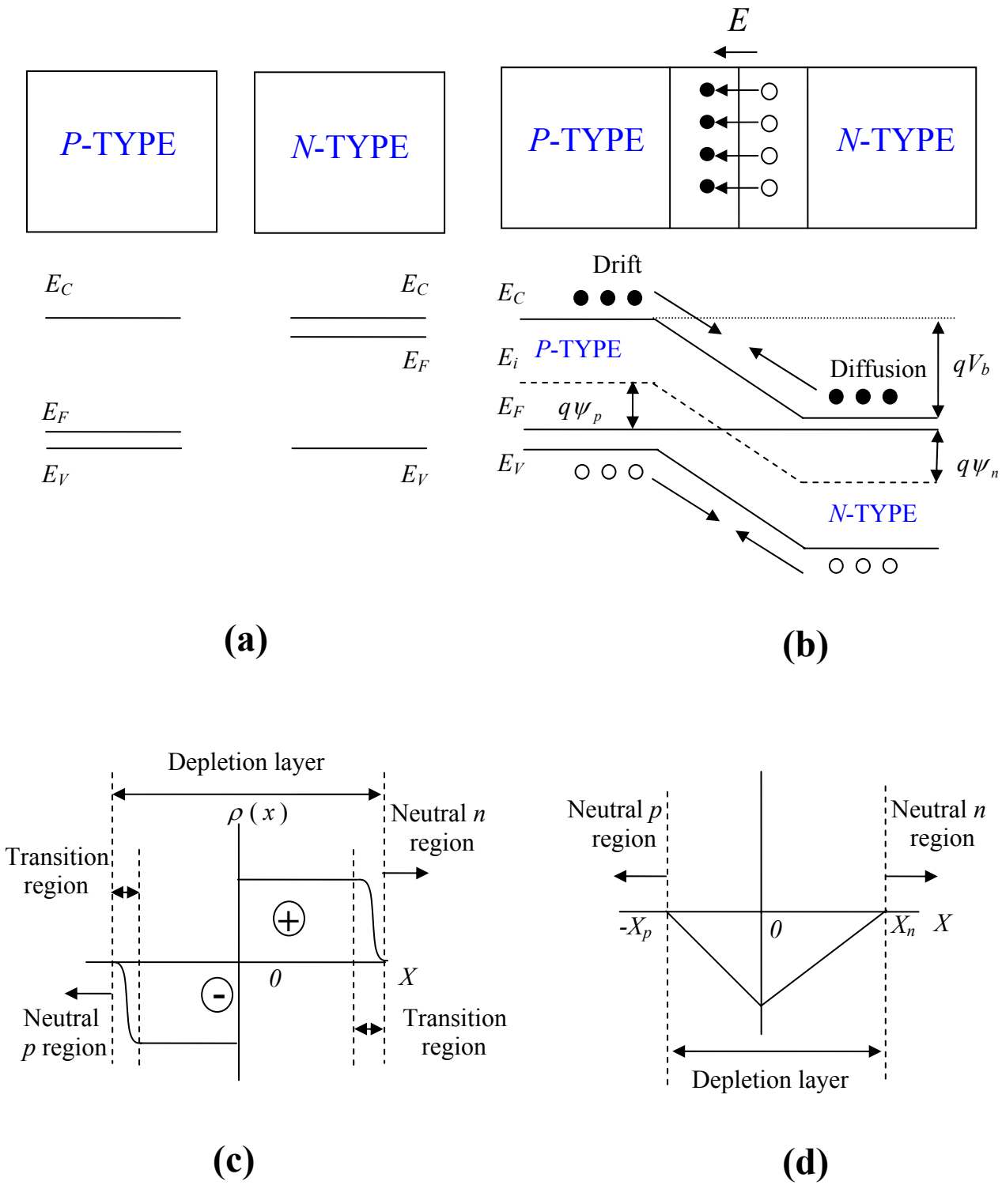

Figure 1.9 (a) Uniformly doped *p*-type and *n*-type semiconductors before the junction is formed. (b) The electric field in the depletion region and the energy band diagram of a *p-n* junction in thermal equilibrium. (c) Space charge distribution. (d) Electric field distribution.

$$J = J_{drift} + J_{Diffusion} = J^{n}_{drift} + J^{p}_{drift} + J^{n}_{Diffusion} + J^{p}_{Diffusion} = 0\,, \qquad (1.16)$$

where $J^{n}_{drift}, J^{p}_{drift}$ are the electron and hole drift currents (the transport of carriers under the influence of an applied electric field) and $J^{n}_{Diffusion}, J^{p}_{Diffusion}$ are the electron and hole diffusion currents (current component, which can exist if there is a spatial variation of carrier concentration or temperature in the semiconductor material).

Thus, for each type of carrier the drift current due to the electric field must exactly cancel the diffusion current due to the concentration gradient. So, for the net electron current density:

$$J_n = J^{n}_{drift} + J^{n}_{Diffusion} = q\mu_n nE + qD_n \frac{dn}{dx} = \mu_n n \frac{dE_F}{dx} = 0\,. \qquad (1.17)$$

Similarly one can obtain for the hole current density:

$$J_p = J^{p}_{drift} + J^{p}_{Diffusion} = q\mu_p pE - qD_p \frac{dp}{dx} = \mu_p p \frac{dE_F}{dx} = 0\,, \qquad (1.18)$$

where n (p) is the electron (hole) concentration, $\mu_n(\mu_p)$ is the electron (hole) mobility, E is the electric field in the x direction, $D_n(D_p)$ is called the diffusion coefficient for electron (hole) respectively.

Thus, from the equations (1.17) and (1.18) follows that for the condition of zero net electron and hole currents, the Fermi level must be constant (independent of x) throughout the sample, as illustrated in the Fig 1.9 (b). The constant Fermi level required at thermal equilibrium results in a unique space charge distribution at the junction, and is managed by the diffusion voltage or built-in potential V_b. The built-in potential V_b in a semiconductor equals the potential across the depletion region in thermal equilibrium. Since thermal equilibrium implies that the Fermi energy is constant throughout the *p-n* diode, the internal potential must equal the difference between the Fermi energies of each region. It also equals the sum of the bulk potentials of each region (ψ_n and ψ_p), since the bulk potential quantifies the distance between the Fermi energy and the intrinsic energy (E_i). Thus, the built-in potential can be described by the following equation:

$$V_b = \frac{k_B T}{q} \ln\left(\frac{N_A N_D}{n_i^2}\right), \tag{1.19}$$

where T is the absolute temperature, k_B is Boltzmann constant, q is magnitude of electronic charge, n_i is intrinsic density, N_A and N_D are the acceptor and donor concentrations.

On the other hand, the zero bias barrier height (ϕ_B) can be written as:

$$\phi_B = V_b + \frac{kT}{q} \ln\left(\frac{N_C}{N_D}\right), \tag{1.19a}$$

where N_C is the effective density of states in the conduction band.

A voltage applied to a *p*-*n* junction will disturb the precise balance between the diffusion current and drift current of electrons and holes. If we apply a positive voltage V to the *p*-type semiconductor material with respect to the *n*-side, the *p*-*n* junction becomes forward biased. The positive charge applied to the *p*-type material repels the holes, while the negative charge applied to the *n*-type material repels the electrons. Because electrons and holes are pushed towards the junction, the distance between them decreases. This lowers the barrier in potential, from the magnitude qV_b at the thermal equilibrium to the $q(V_b\text{-}V)$, as shown in Fig. 1.10 (b). With increasing forward-bias voltage, the depletion zone eventually becomes thin enough that the zone's electric field cannot counteract charge carrier motion across the *p*-*n* junction, consequently reducing electrical resistance. The electrons which cross the *p*-*n* junction into the *p*-type material (or holes which cross into the *n*-type material) will diffuse in the near-neutral region. Therefore, the amount of minority diffusion in the near-neutral zones determines the amount of current that may flow through the diode.

Under reverse bias (when we apply positive voltage V to the *n*-type semiconductor with respect to the *p*-side) the applied voltage increases the electrostatic potential across the depletion region by V, as shown in Fig. 1.10 (c).

Because the *p*-type material is now connected to the negative terminal of the power supply, the holes in the *p*-type material are pulled away from the junction causing the width of the depletion zone to increase. Similarly, because the *n*-type region is connected to the positive terminal, the electrons will also be pulled away from the junction. Therefore the depletion region widens, and does so increasingly with increasing reverse-bias voltage. This increases the voltage barrier causing a high resistance to the flow of charge carriers, thus, allowing minimal electric current to cross the *p*-*n* junction.

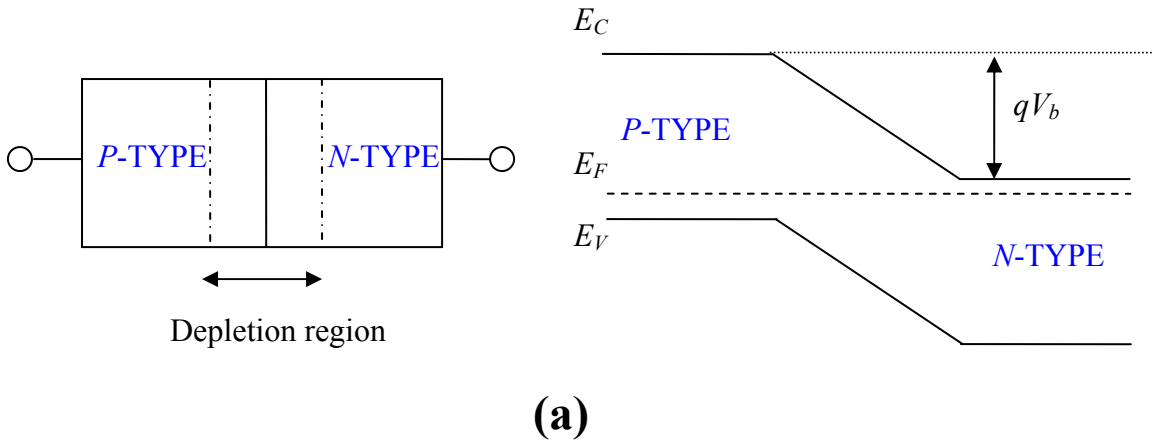

(a)

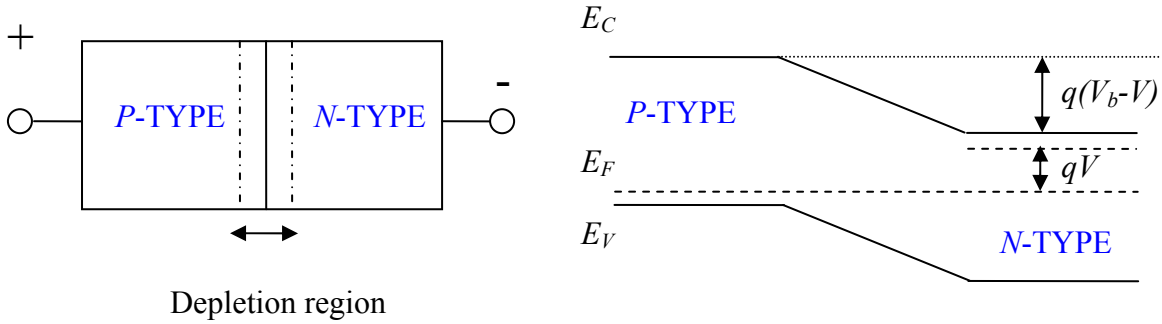

(b)

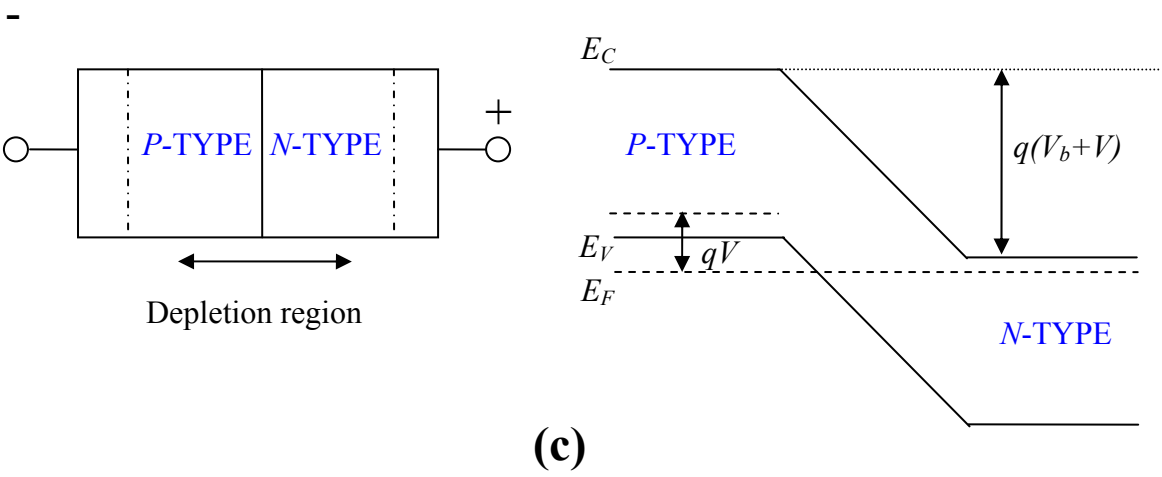

(c)

Figure 1.10 Schematic diagrams of width of depletion layer and energy bands of a *p-n* junction under various bias conditions. (a) Thermal equilibrium condition. (b) Forward bias condition. (c) Reverse bias condition.

The Current-Voltage (*I-V*) characteristic for an ideal *p-n* junction is presented in Fig. 1.11 (in the Cartesian (a) and semi log (b) scale) and can be described by equation (1.20):

$$J = J_S(\exp(\frac{qV}{kT}) - 1), \tag{1.20}$$

where J_S is the saturation current density (the term saturation indicates that J approaches an asymptote and becomes independent of the voltage V), and have form:

$$J_S = \frac{qD_p p_{no}}{L_p} + \frac{qD_n n_{po}}{L_n}, \tag{1.21}$$

where D_p (D_n) is the hole (electron) diffusion coefficient, L_p (L_n) is the hole (electron) diffusion length, p_{no} (n_{po}) is the equilibrium hole (electron) density in the *n (p)*-side.

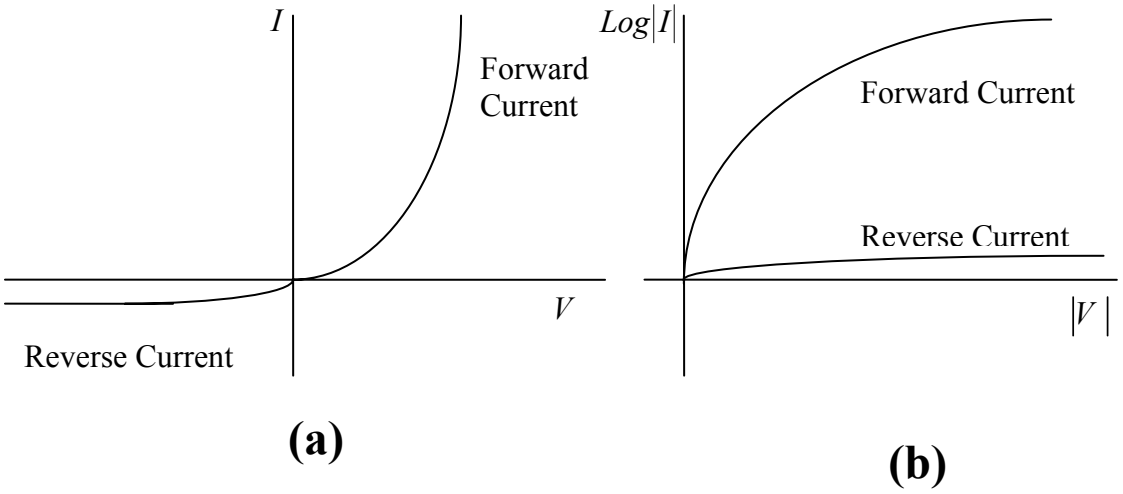

Figure 1.11 Ideal Current-Voltage characteristics. (a) Cartesian plot. (b) Semilog plot.

However, the equation (1.20) can only give qualitative agreement. The deviations from the ideal case are mainly due to the following effects: (a) the surface effect, (b) the generation and recombination of carriers in the depletion layer, (3) the tunneling of carriers between states in the band gap, (4) the high-injection condition, which may occur even at relatively small forward bias, (5) series resistance effect.

The total current of the real diode (when the generation-recombination processes are taken into account) is given by the empirical relation:

$$J = J_S(\exp(\frac{qV}{nkT}) - 1), \tag{1.22}$$

where n is ideality factor.

If the ideal diffusion current dominates n = 1, whereas n = 2 if the recombination current dominates. When both currents are comparable n has a value of between 1 and 2.

The change in applied voltage modulates the space-charge layer thickness. As a result the charge Q in the space charge region changes with respect to the junction voltage. The small signal capacitance associated with the dipole of charge in the depletion layer of a p-n junction is defined by:

$$C = \frac{dQ}{dV}. \tag{1.23}$$

With the depletion approximation, the space charge can be easily found by neglecting free electrons and holes in that region. The depletion capacitance per unit area is

$$C = \frac{\varepsilon_S}{W} = \begin{cases} \left[\dfrac{qa\varepsilon_S{}^2}{12(V_b - V)}\right]^{\frac{1}{3}} & \text{(for a linearly graded junction)} \quad (1.24) \\ \sqrt{\dfrac{q\varepsilon_S N_A N_D}{2(N_A + N_D)(V_b - V)}} & \text{(for abrupt junction)} \quad (1.25) \end{cases}$$

where ε_S is semiconductor permittivity, a is the impurity gradient, W is the total depletion layer width, q is magnitude of electronic charge.

The depletion approximation only accounts for the change of charge due to shifting the edges of the space-charge region and neglects the change of the free carrier charge in the volume of the space charge region associated with the carrier injection from one side of the junction to the other. Thus, the depletion capacitance in (1.24) and (1.25) is only accurate when the p-n junction is reverse biased.

1.4.2 Spin diodes

Spin diodes are inhomogeneous two-terminal devices, whose electronic or optical properties depend on the spin polarization of the carriers. Such devices were envisaged long before the emergence of spintronics. For example, in 1976 Solomon *et. al*. [99] demonstrated a silicon *p*-*n* junction whose current was modified by changing spin polarization of recombination centers. In a magnetic field both the mobile carriers and the recombination centers have an equilibrium spin polarization due to the Zeeman splitting. The current in a *p*-*n* junction depends on the recombination rate, which in turn, depends on the relative orientation of the spin of the carriers and the centers [100]. The trick to modifying the current is to decrease (even saturate) the spin polarization of either the electrons or the centers by electron spin resonance. Solomon obtained a variation of about 0.01% of the saturation current at small biases where recombination in the space-charge region dominates.

Afterwards several types of spin diodes [101-103] have been proposed to employ for spin injection and spin detection through semiconductor interfaces comprising a magnetic semiconductor as the spin injector. Thus, in these works authors demonstrated that magnetic tunneling diodes can be used for spin injection from ferromagnetic (*p*-type GaMnAs) to nonmagnetic (*n*-type GaAs) semiconductors. The spin transfer in such structures was investigated by the total spin-polarized electron current after its injection into a GaAs quantum well (QW).

Another kind of spin diodes, spin light emitting diode (spin-LED), which could also be used for spin injection and spin detection in semiconductors, has been proposed in Refs. [9, 12]. In a spin-LED carriers are electrically injected from a contact with a net spin polarization into a semiconductor heterostructure, where they radiatevely recombine. Polarization analysis of the electroluminescence effectively interrogates the spin polarization of the carrier involved.

In contrast to the spin-LED diode resonant tunneling diodes have been demonstrated playing as both effective spin injectors and spin filters. Solid state spin filtering was firstly realized in normal metal/ferromagnet/normal metal (N/F/N) tunneling junction. Esaki *et*. *al*. [104] demonstrated that magnetic tunneling through (ferro) magnetic semiconductor Eu chalcogenides [105-107] such as EuSe and EuS can be modified by magnetic field. In this case the change in *I*-*V* characteristics of the N/F/N structure was explained by influence of the magnetic field on the barrier height formed at the N/F interface (for EuSe, the barrier height

was lowered by 25% at 2 T). Thus, the Zeeman splitting results in effective spin filtering and leads to appearance of spin-polarized current in semiconductor heterostructures and superlattices (enhanced by large g factors) [46, 108], quantum dots [109-111] and nanocrystals [48]. These spin filtering properties of the Eu chalcogenides used together with one-electron quantum dots were proposed as the basis for a method to convert single spin into single charge measurements and provide an important ingredient in realizing a quantum computer [112].

Besides bipolar devices, a magnetic unipolar diode has been proposed by Flatte and Vignale [55] to simulate the performance of ordinary diodes but with homogeneous monopolar doping (either donors or acceptors). However, of course, this literature review cannot be completed without mentioning of works by Zutic and Fabian in which authors described three spintronics device schemes having an advantage of bipolar nature of transport in inhomogeneously doped semiconductors: spin-polarized *p-n* junction [1, 2, 36], spin solar cell [2] and magnetic bipolar diode [3, 5].

In this part of the thesis the main principles of operation of magnetic bipolar diode (MBD) are presented. According to Zutic and Fabian the MBD is a *p-n* junction diode with one or both magnetic regions. One should notice that MBD is the prototypical device of bipolar spintronics, a subfield of spintronics in which both electrons and holes take part in carrier transport, while either electrons or holes (or both) are spin polarized. The advantages of magnetic bipolar spintronic devices lie in the combination of equilibrium magnetism and nonequilibrium spin and effective methods to manipulate a minority carrier population. The important question, of whether spin can be injected by the majority carriers from the magnetic majority region into the nonmagnetic minority one, was answered negative. Zutic and Fabian demonstrated that only if nonequilibrium spin is firstly generated in the majority region it can subsequently be injected through the depletion layer. They have also shown that magnetoresistance of a magnetic *p-n* junction increases exponentially with increasing magnetic field at large fields. Moreover, for these structures authors predicted a spin-voltaic effect [3, 5] which is related to the Silsbee-Johnson spin-charge coupling [113, 114] and in which charge current (or voltage in an open circuit) arises solely due to a nonequilibrium spin maintained in a proximity to the magnetic region. Such magnetic *p-n* junctions can also serve as spin valves since the direction of the zero bias current can be reversed by reversing either polarization of the source spin or direction of the applied magnetic field.

Band energy schemes of the magnetic *p-n* junction with magnetically active electrons (arrows) and unpolarized holes are shown in Fig. 1.12.

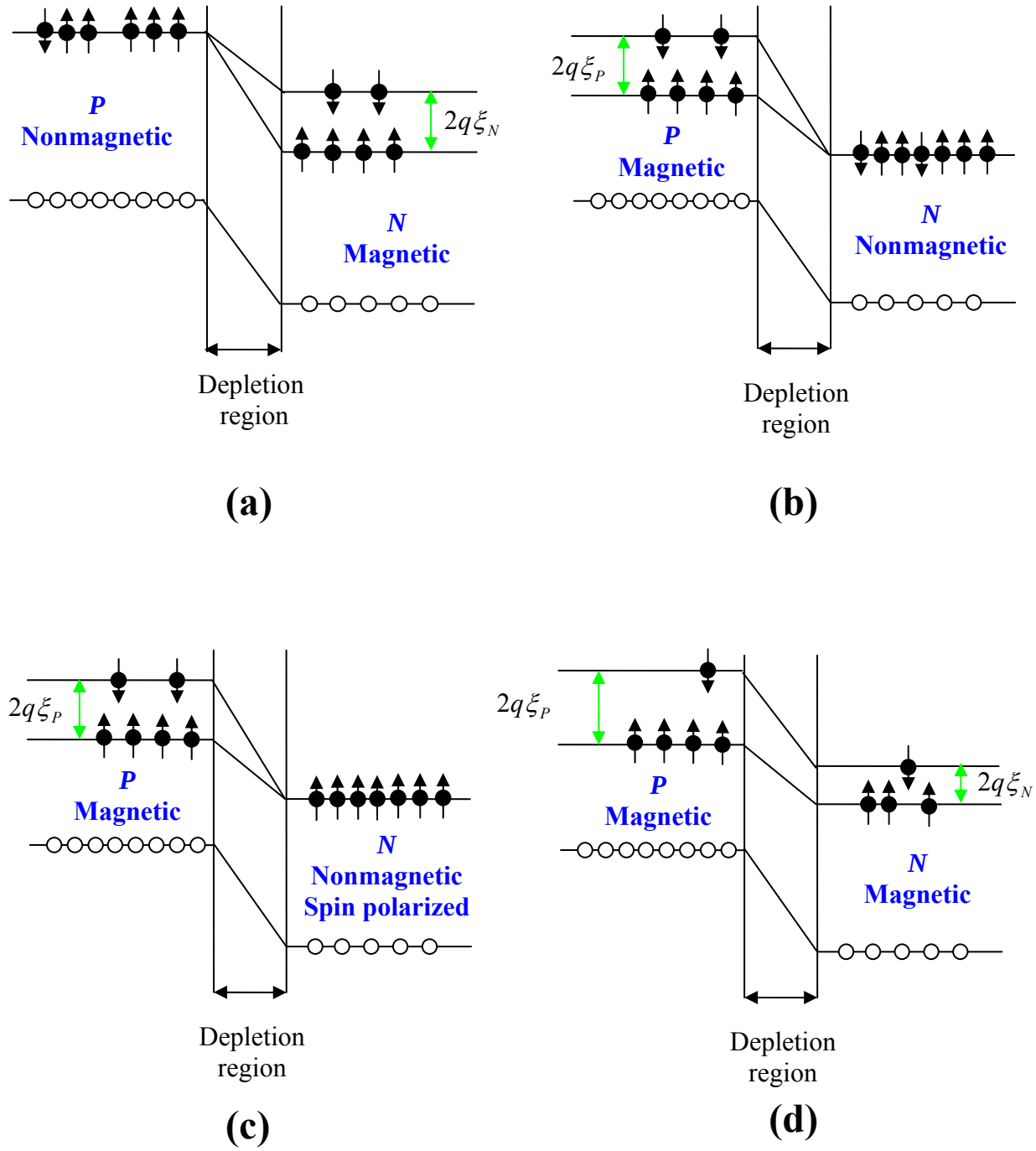

Figure 1.12 Band-energy schemes of the magnetic/nonmagnetic *p-n* junctions with magnetically active electrons (arrows) and unpolarized holes. (a) Electrons from the magnetic *n* region can be injected into the nonmagnetic *p* region. (b) Similarly for spin extraction if the *p* region is magnetic. (c) If the *p* region is magnetic and there is a nonequilibrium spin in the *n* region, a giant magnetoresistance and spin-voltaic effects arise. (d) Magnetic *p-n* junction with both magnetic regions.

The presence of magnetic impurities can significantly increase the carrier g factor; so that application of a magnetic field B induces a large Zeeman spin splitting of the bands. In the following we will assume that only the conduction band is spin split. This means that only electrons are spin polarized keeping holes unpolarized. This simplification does not affect the main conclusions, as electron and hole transports are fully separated.

To introduce equations for spin and charge bipolar transport in inhomogeneously doped magnetic semiconductors a semiconductor doped with $N_a(r)$ acceptors and $N_d(r)$ donors and with magnetic impurities, whose density varies in space and whose presence leads to large g factor for electrons and holes $g_n(r)$ and $g_p(r)$ is considered. In a homogeneous magnetic field B the carrier energies are Zeeman split: spin up ($\lambda = 1$ or $\uparrow$) and spin down ($\lambda = -1$ or $\downarrow$) electrons have their energy shifted by $-2\lambda q\xi_n(r) = -\lambda g_n(r)\mu_B B$, where μ_B is Bohr magneton and q is the proton charge. The energy of holes changes by $2\lambda q\xi_p(r) = \lambda g_p(r)\mu_B B$.

Carrier charge current densities, resulting from the electric field $E = -\nabla\phi$ (ϕ is the electric potential), nonuniform magnetic potential ξ, electron (hole) densities $c = n$ ($c = p$), can be written in the following form:

$$J_{C\lambda} = q\mu_n c_\lambda E \pm qD_{C\lambda}\nabla c_\lambda - q\lambda\mu_{C\lambda}c_\lambda\nabla\xi_C, \tag{1.26}$$

where the upper (lower) sign is for electrons (holes), μ and D stand for mobility and diffusivity, and the magnetic drift $q\nabla\xi$ forces carriers with opposite spins to go in opposite directions.

Equation (1.26) was obtained from the requirement that carrier densities in an inhomogeneous environment have the quasi-equilibrium form [115]. From eq. (1.26) the carrier charge and spin current densities $J = J_\uparrow + J_\downarrow$ and $J_S = J_\uparrow - J_\downarrow$ are

$$J_C = \sigma_C E - \sigma_{SC}\nabla\xi_C \pm qD_C\nabla n \pm qD_{SC}\nabla s_C \tag{1.27}$$

$$J_{SC} = \sigma_{SC} E - \sigma_C\nabla\xi_C \pm qD_{SC}\nabla c \pm qD_C\nabla s_C, \tag{1.28}$$

where $c = c_\uparrow + c_\downarrow$ and $s_C = c_\uparrow - c_\downarrow$, and the carrier charge and spin conductivities are $\sigma_C = q(\mu_C c + \mu_{SC} s_C)$, $\sigma_{SC} = q(\mu_{SC} c + \mu_C s_C)$ respectively, $\mu_C = \frac{(\mu_{C\uparrow} + \mu_{C\downarrow})}{2}$ and $\mu_{SC} = \frac{(\mu_{C\uparrow} - \mu_{C\downarrow})}{2}$ are carrier charge and spin mobilities, respectively. Similar equations can be written for diffusivities.

Equation (1.27), which is a generalization of the Johnson-Silsbee magneto-transport equations [116], reflects the spin-charge coupling in bipolar transport in inhomogeneous magnetic semiconductors: a spatial variation in spin density, as well as in $q\nabla\xi$, can cause charge currents, while spin currents can flow as a result of a spatial variation of carrier densities and ϕ.

Generation and recombination of electrons and holes are assumed to be mostly due to band-to-band processes. Further, electrons (holes) with a given spin are assumed to recombine with holes (electrons) of either spin. The stationary continuity for carriers is

$$\nabla \cdot \frac{J_{C\lambda}}{q} = \pm w_{C\lambda}(c_\lambda \bar{c} - c_{\lambda 0}\bar{c}_0) \pm \frac{c_\lambda - c_{-\lambda} - \lambda \tilde{s}_c}{2T_{1C}} \qquad (1.29)$$

where $\bar{c}$ is *p(n)* if *c* is *n(p), c_0* is the equilibrium carrier density, $w_{C\lambda}$ is the band-to-band recombination rate, T_1 is the spin relaxation time. Spin relaxation equilibrates carrier spins while preserving nonequilibrium carrier density, so for a nondegenerate semiconductor, $\tilde{s}_C = \alpha_{C0} c$, where $\alpha_{C0} = \frac{s_{C0}}{c_0} = \tanh(\frac{\xi_C}{V_T})$ is the equilibrium carrier spin polarization ($V_T = \frac{k_B T}{q}$, with k_B being the Boltzmann constant and *T* temperature).

Equations (1.27-1.29), and Poisson's equation $\nabla \cdot \varepsilon E = \rho$, where $\rho = q(p - n + N_D - N_A)$ and ε is the dielectric constant of the semiconductor, determine the distributions of charge and spin in a magnetic semiconductor under applied bias *V* [3].

To illustrate the *I-V* characteristics of MBD's, the magnetic *p-n* junction, with magnetic *p*-type region and nonmagnetic *n*-type region is assumed to be at the low-injection limit. Zutic and Fabian distinguished equilibrium spin electron J_n and holes J_p currents, and

nonequilibrium spin induced current $J_n^{'}$, so that the total charge current is $J = J_n + J_p + J_n^{'}$. The individual contributions are

$$J_n = q\frac{D_n n_i^2}{L_n N_A}\cosh(\frac{\xi}{V_T})\coth(\frac{x_p}{L_n})(\exp(\frac{V}{V_T})-1) \tag{1.30}$$

$$J_p = q\frac{D_p n_i^2}{L_p N_D}\coth(\frac{L-x_n}{L_p})(\exp(\frac{V}{V_T})-1) \tag{1.31}$$

$$J_n^{'} = q\frac{D_n n_i^2}{L_n N_A}\sinh(\frac{\xi}{V_T})\coth(\frac{x_p}{L_n})\alpha_n \exp(\frac{V}{V_T}) \tag{1.32}$$

where L_n (L_p) is minority diffusion length of electron (hole), V is applied bias, x_n (x_p) is the thickness of *n*- and *p*-type regions, D_n, D_p are electron and hole diffusivities, and $V_T = \frac{k_B T}{q}$, α_n is nonequilibrium spin population, n_i is the intrinsic carrier density.

Equations (1.30-1.32) reveal another interesting phenomenon called a spin-voltaic effect. The current $J_n^{'}$ stays finite even for $V = 0$, if $\alpha_n \neq 0$. This means that a current flows at zero bias. This is analogue of the photovoltaic effect, where a reverse current flow if carriers are photo generated in the space-charge region. In the spin-voltaic effect both reverse and forward currents can flow depending on the relative orientation of B and α_n; and the device can function as a spin valve. The physics of the spin-voltaic effect is that nonequilibrium spin in the space-charge region disturbs the balance between the generation and recombination currents. If $\xi > 0$, and more spin up electrons are present at x_n ($\alpha_n > 0$), the barrier for them to cross the region is smaller than the barrier for the spin down electrons, so more electrons flow from *n* to *p* than from *p* to *n*, and positive charge current results. If $\alpha_n < 0$ the current is reversed.

One should also emphasize that the current through a magnetic/nonmagnetic *p*-*n* junction depends exponentially on magnetic field. This origins from the following. First of all, a magnetic field makes the band gap spin dependent leading to the increased density of the minority carriers. For example, the equilibrium density of electrons in a magnetic *p* region

(Fig. 1.12 (c)) is $n_0 = n_i^2 \cosh(\frac{\xi}{V_T}) / N_A$ (in equilibrium $n_0 p_0 = n_i^2 \cosh(\frac{\xi}{V_T})$). The current through a *p*-*n* junction is proportional to the density of minority carriers, and, thus, it will grow exponentially with B for $\xi \geq V_T$. Secondly, a current can also depend on magnetic field if a nonequilibrium spin with polarization α_n is introduced optically or by electrical spin injection into the sample. In this case, the exponential magnetoresistance becomes giant and leads that the resistance of the structure changes when orientation of the magnetic moment in the magnetic region changes with respect to orientation of the injected spin. Thus, the current is exponentially sensitive to both B and α_n, being large (small) if they have the same (opposite) sign [3].

Although until now practical MBD's are not commonly used, magnetic *p*-*n* junctions have already been demonstrated. For example, Wen *et. al*. [117] demonstrated that a ferromagnetic *p*-*n* junction based on $CdCr_2Se_4$ doped with Ag acceptors and In donors can act as a magnetic diode. Also, heavily doped *p*-GaMnAs/*n*-GaAs junctions were used to demonstrate tunneling interband spin injection [3-5,118]. Incorporation of (Ga,Mn) As layer in the intrinsic region of *p*-*i*-*n* GaAs diode was shown lo lead to an efficient photodiode, in which the Mn ions function as recombination centers [119]. At last, Tsui *et. al*. [120] showed that the current in *p*-CoMnGe/*n*-Ge magnetic heterojunction diodes can indeed be controlled by the magnetic field.

1.4.3 Bipolar transistor

The transistor (contraction for transfer resistor) is three-terminal, solid-state electronic device. Normally, the transistor is integrated with other circuit elements for voltage gain, current gain, or signal power gain. There are two general types of transistors in use today: (1) the bipolar transistor (often called the bipolar junction transistor, or BJT), and (2) the field-effect transistor (FET). The bipolar transistor is one of the most important semiconductor devices. It has been used extensively in high-speed circuits, analog circuits and power amplification. This is in contrast to the field-effect devices, in which predominantly only one kind of carrier participates.

A BJT consists of a thin piece of one type of semiconductor material between two thicker layers of the opposite type. For example, if the middle layer is *p*-type, the outside layers must be *n*-type. Such a transistor is an *n*-*p*-*n* transistor. One of the outside layers is

called the *emitter*, and the other is known as the *collector*. The middle layer is the *base*. The places where the emitter joins the base and the base joins the collector are called *junctions*. The layers of an *n-p-n* transistor must have the proper voltage connected across them. The voltage of the base must be more positive than that of the emitter. The voltage of the collector, in turn, must be more positive than that of the base. The emitter supplies electrons. The base pulls these electrons from the emitter because it has a more positive voltage than does the emitter. This movement of electrons creates a flow of electricity through the transistor. The current passes from the emitter to the collector through the base. Changes in the voltage connected to the base modify the flow of the current by changing the number of electrons in the base. In this way, small changes in the base voltage can cause large changes in the current flowing out of the collector. However, the usefulness of any transistor comes from its ability to control a strong current with a weak voltage. Manufacturers also make *p-n-p* junction transistors. In these devices, the emitter and collector are both a *p*-type semiconductor material and the base is *n*-type. A *p-n-p* junction transistor works on the same principle as an *n-p-n* transistor. However, it differs in one respect. The main flow of current in a *p-n-p* transistor is controlled by altering the number of holes rather than the number of electrons in the base. In addition, this type of transistor works properly only if the negative and positive connections to it are the reverse of those of the *n-p-n* transistor.

In electronics there are three basic single-stage BJT amplifier topologies: the emitter follower, which is a current amplifier but has no voltage gain, the common emitter amplifier which has current and voltage gain, and the common base amplifier which has voltage gain but no current gain.

The available power gain of the transistor in the common-emitter configuration is higher than it is in either of the other two configurations. This follows qualitatively from the fact that input voltage and current are small in the common-emitter amplifier. Other unique features of the common-emitter stage are its phase reversal property, and the fact that current gain and voltage gain can simultaneously be greater than unity. These properties make the common-emitter stage more widely used than the other circuit configurations, so that common-emitter characteristics not only give the most accurate information about the transistor, but also are generally most useful in practice.

Moreover, Bipolar Junction Transistors have five distinct regions of operation, defined mostly by applied bias:

(a) **Forward-active** (or simply, **active**): The emitter-base junction is forward biased and the base-collector junction is reverse biased. Most bipolar transistors are designed to afford

the greatest common-emitter current gain, β_0 in forward-active mode. If this is the case, the collector-emitter current is approximately proportional to the base current, but many times larger, for small base current variations.

(b) **Reverse-active** (or **inverse-active** or **inverted**): By reversing the biasing conditions of the forward-active region, a bipolar transistor goes into reverse-active mode. In this mode, the emitter and collector regions switch roles. Since most BJTs are designed to maximize current gain in forward-active mode, the β_0 in inverted mode is several times smaller. This transistor mode is seldom used, usually being considered only for failsafe conditions and some types of bipolar logic. The reverse bias breakdown voltage to the base may be an order of magnitude lower in this region.

(c) **Saturation**: With both junctions forward-biased, a BJT is in saturation mode and facilitates high current conduction from the emitter to the collector. This mode corresponds to a logical "on", or a closed switch.

(d) **Cutoff**: In cutoff, biasing conditions opposite of saturation (both junctions reverse biased) are present. There is very little current flow, which corresponds to a logical "off", or an open switch.

(e) **Avalanche breakdown region:** Avalanche breakdown is a phenomenon that can occur in both insulating and semiconducting materials. It is a form of electric current multiplication that can allow very large currents to flow within materials which are otherwise good insulators.

Figure 1.13 (a) and (d) shows an idealized *p*-*n*-*p* transistor and its energy band diagram in thermal equilibrium, where all three leads are connected together or all are grounded. The depletion regions near the two junctions are illustrated by dash lines. Figure 1.13 (b) presents the impurity densities in the three doped regions, where the emitter is more heavily doped than the collector. On the other hand, the base region doping is less than the emitter doping, but greater than the collector doping. The corresponding electric field profiles in the two depletion regions are present in Fig. 1.13 (c).

Figure 1.14 shows the *p*-*n*-*p* transistor from Fig. 1.13, which is biased in the active mode and connected as an amplifier, for example, with the common-base configuration, that is the base lead is common to the input and output circuits (Fig. 1.14 (a)). Figs. 1.14 (b) and (c) show the charge densities and the electric fields, under biasing conditions. Note that the depletion layer width of the emitter-base junction is narrower and the collector-base junction is wider, compared with the equilibrium case shown in Fig. 1.13. Figure 1.14 (d) shows the corresponding energy band diagram under the active mode.

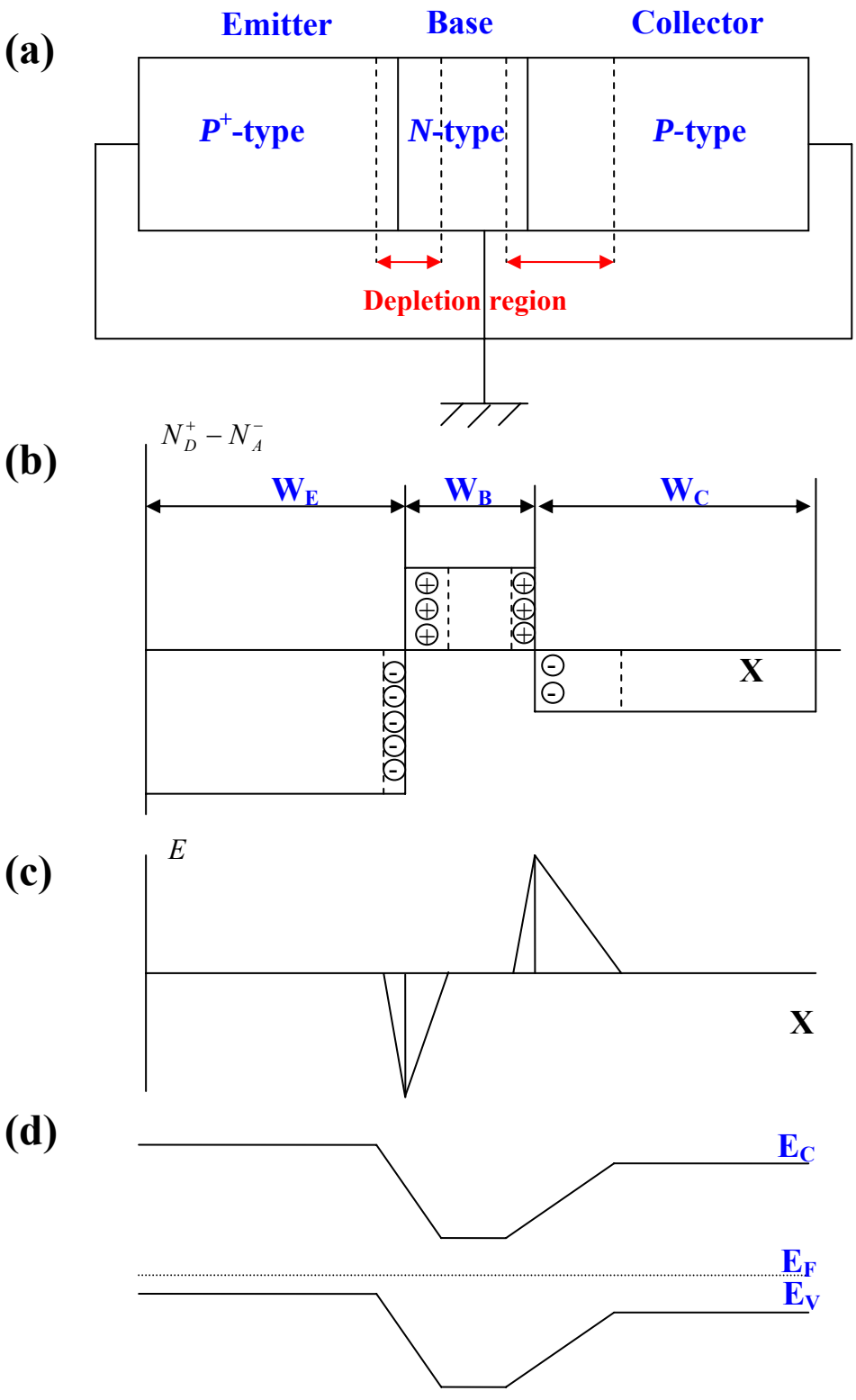

Figure 1.13 (a) A *p-n-p* transistor with all leads grounded (at thermal equilibrium). (b) Doping profile of transistor with abrupt impurity distributions. (c) Electric field profile. (d) Energy band diagram in thermal equilibrium.

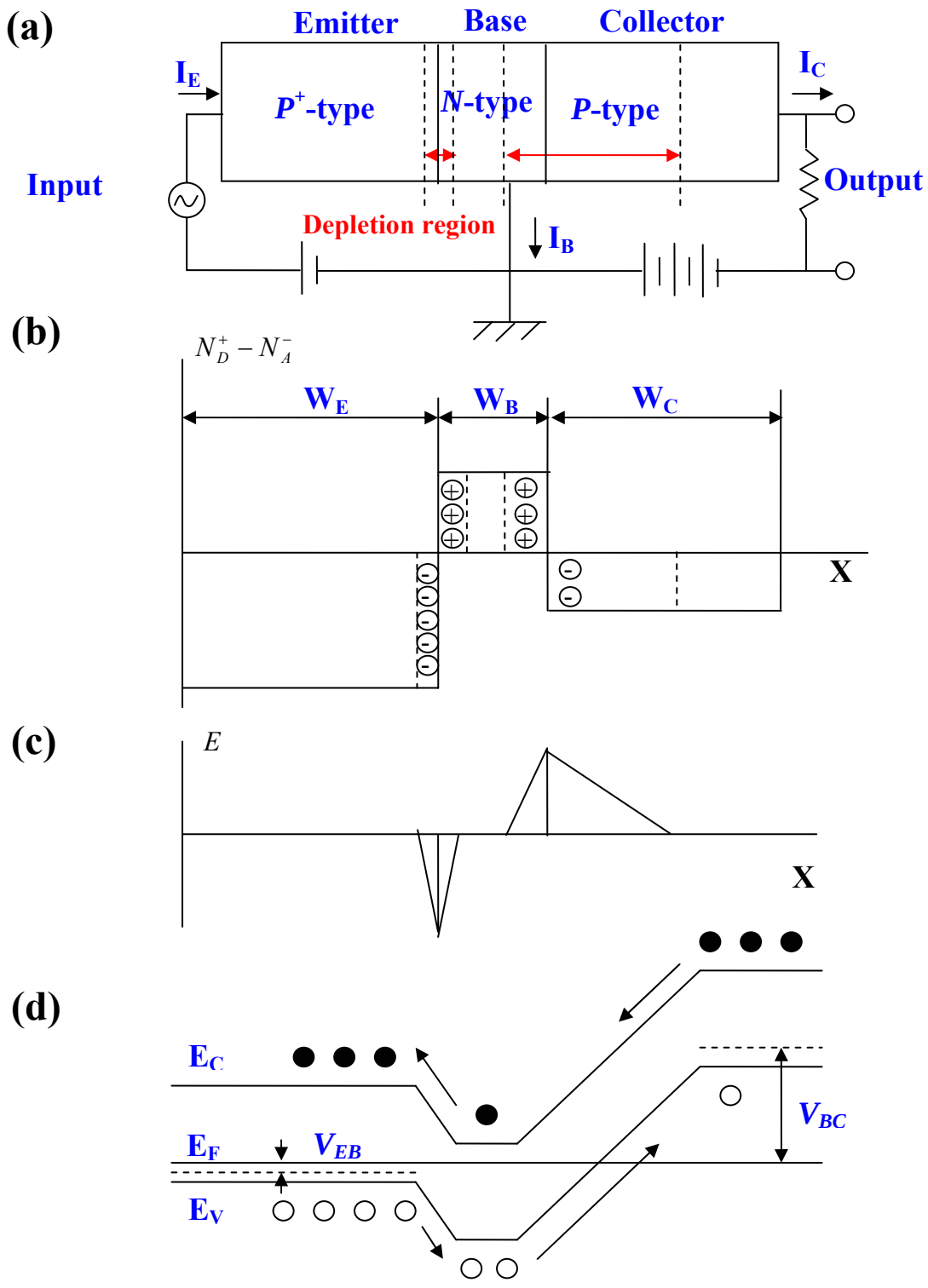

Figure 1.14 (a) A *p-n-p* transistor under the active mode of operation. (b) Doping profiles and the depletion regions under biasing conditions. (c) Electric field profile. (d) Energy band diagram at thermal equilibrium.

Since the emitter-base junction is forward biased, holes are injected from the *p*-type emitter into the base and electrons are injected from the *n*-type base into the emitter. Under the ideal-diode condition, there is no generation-recombination current in the depletion region; these two current components constitute the total emitter current. The collector-base junction is reverse biased, and a small reverse saturation current will flow across the junction. However, if the base width is sufficiently narrow, the holes injected from the emmiter can diffuse through the base to reach the base-collector depletion edge and then "float up" into the collector. If most of the injected holes can reach the collector without recombining with electrons in the base region, then the collector hole current will be very close to the emitter hole current. Therefore, carriers injected from a nearby emitter junction can result in a large current flow in a reverse-biased collector junction. This is the transistor action, and it can be realized only when the two junctions are physically close enough.

If on the other hand, the two junctions are so far apart that all the injected holes are recombined in the base before reaching the base-collector junction, then the transistor action is lost and the *p*-*n*-*p* structure becomes merely two diodes connected back to back.

Figure 1.15 shows the various current components in a real *p*-*n*-*p* transistor biased in the active mode.

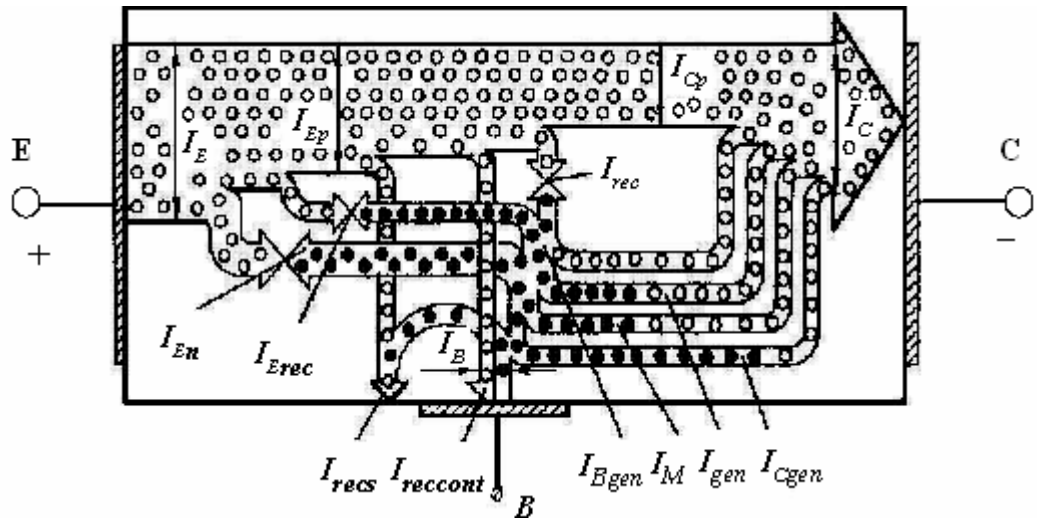

Figure 1.15 Various current components in a *p*-*n*-*p* transistor under active mode of operation.

The holes injected from the emitter constitute the current I_{Ep}, which is the largest current component in a well-designed transistor. Most of the injected holes will reach the collector junction and give rise to the current I_{Cp}. However, a part of them will recombine: with

electrons in *n*-type base region *(I_{rec})*, on the surface states and just under contact layer (respectively I_{recs}, $I_{reccont}$).

These current components are not desirable and must be minimized usually by using heavier emitter doping or heterojunction, decreasing base region width and surface passivation. Moreover, there are four base current components, labeled I_B, I_{En} and I_{Bgen}, I_{gen}. I_B corresponds to electrons that must be supplied by the base to replace electrons recombined with the injected holes. I_{En} corresponds to the current arising from electrons being injected from the base to the emitter. I_{Bgen} (I_{Cgen}) and I_{gen} correspond to thermally generated electrons into the base (collector) region and near the base-collector junction edge. Also at high voltage the avalanche multiplication of the carriers can arise and then a new current component I_M should be taken into account in the collector junction.

Analyzing currents distribution in an ideal transistor one can conclude that only emitter and base currents have a strong influence on the output collector current, whereas influence of other current components mentioned above can be neglected.

Thus, all terminal currents for an ideal transistor in terms of the various current components, described above can be expressed by the following equations:

$$I_E = I_{Ep} + I_{En}, \tag{1.33 a}$$

$$I_C = I_{Cp} + I_{Cn}, \tag{1.33 b}$$

$$I_B = I_E - I_C = I_{En} + I_{Ep} - I_{Cp} - I_{Cn}. \tag{1.33 c}$$

The important parameters in characterization of bipolar transistors are the common-base current gain α_0, emitter efficiency γ and base transport factor α_T. These quantities are defined by:

$$\alpha_0 = \frac{I_{Cp}}{I_E}; \qquad \gamma = \frac{I_{Ep}}{I_E}; \qquad \alpha_T = \frac{I_{Cp}}{I_{Ep}} \tag{1.34 a,b,c}$$

or in a more general form:

$$\alpha_0 = \gamma \alpha_T \,. \qquad (1.34\ d)$$

For a high quality transistor I_{En} is much smaller comparing with I_{Ep} and I_{Cp}, and then both γ and α_T approach unity. Therefore, α_0 is also close to unity.

Based on these parameters the collector current for the common-base configuration can be expressed by the following equation:

$$I_C = \alpha_0 I_E + I_{CBO}\,, \qquad (1.35)$$

where I_{Cn} was designated as I_{CBO}, in which the first two subscripts (CB) refer to the two terminals between which the current (or voltage) is measured and the third subscript (0) refers to the state of the third terminal with respect to the second.

In a case of common-emitter configuration for a *p-n-p* transistor the collector current can be obtained by substituting Eq. (1.33 (c)) into Eq. (1.35) and solving for I_C:

$$I_C = \frac{\alpha_0}{1-\alpha_0} I_B + \frac{I_{CBO}}{1-\alpha_0} = \beta_0 I_B + I_{CEO}\,, \qquad (1.36)$$

where $\beta_0 = \dfrac{\Delta I_C}{\Delta I_B} = \dfrac{\alpha_0}{1-\alpha_0}$ is the common-emitter current gain, which is the incremental change of I_C with respect to an incremental change of I_B, whereas $I_{CEO} = \dfrac{I_{CBO}}{1-\alpha_0}$ is the current which corresponds to the collector-emitter leakage current for $I_B = 0$.

Because the value of α_0 is generally close to unity, β_0 is much larger than 1. Therefore, a small change in the base current can give rise to a much larger change in the collector current. Figure 1.16 shows typical results of output current-voltage characteristics for the common-base configuration with various emitter current (Fig. 1.16 (a)) and for the common-emitter configuration with various input base current (Fig. 1.16 (b)) in a good quality bipolar transistor.

In a case of common-base configuration, the collector current is practically equal to the emitter current ($\alpha_0 \equiv 1$) and virtually independent of V_{CB}. This is in close agreement with an ideal transistor behavior given by Eq. (1.35). The collector current remains

practically constant, even down to zero volts for V_{CB}, where the holes are still extracted by the collector.

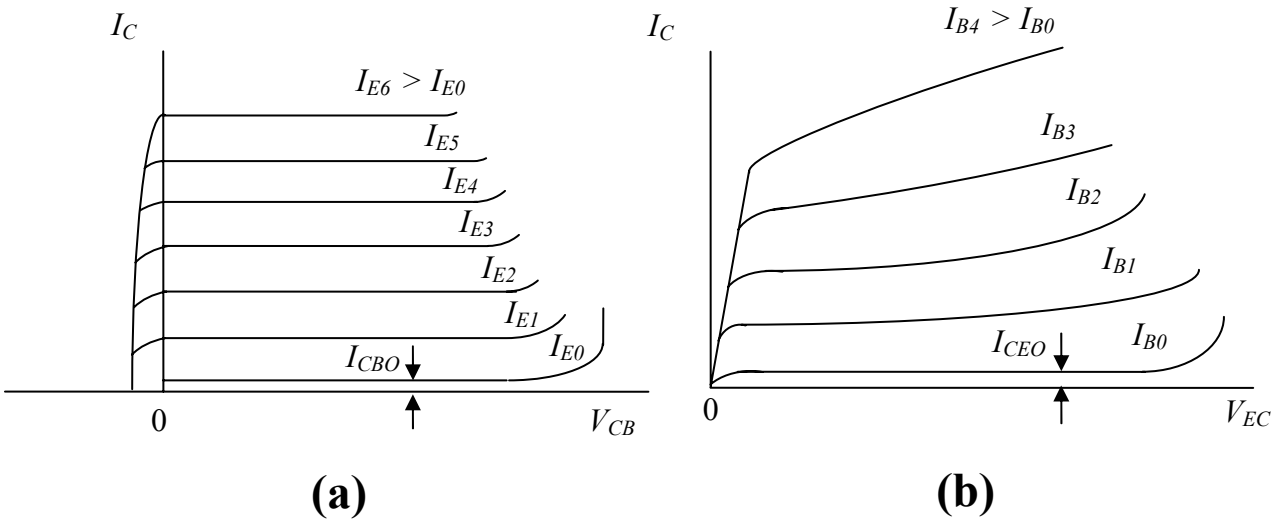

Figure 1.16 Current-Voltage characteristics of *p-n-p* transistor for the Common-Base (a) and Common-Emitter (b) configurations.

In an ideal transistor with the common-emitter configuration, the collector current for a given I_B is expected to be independent of V_{EC} for $V_{EC} > 0$. This is true if we assume that the neutral base width is constant. However, since the width of the space charge region extending into the base region varies with the base-collector voltage, the base width is a function of the base-collector voltage. The collector current, therefore, is dependent on V_{EC}. As the base-collector reverse-bias voltage increases, the base width will be reduced. The reduced base width causes the gradient in the minority-carrier concentration to increase, which causes an increase in the diffusion current. As a result, β_0 will be increased as well.

1.4.4 Magnetic bipolar transistor

Transistors are naturally suited for spin control of electrical currents since three regions (emitter, base, and collector) can serve as a spin injector, transport medium, and a spin detector, respectively. Supporting this S. van Dijken *et. al*. [121] and Jiang *et. al*. [122] showed that the hot-electron transistors consisted of hybrid ferromagnetic metal and semiconductor structures can be used as effective spin injectors and the magnetoresistance of such transistors can be increased up to 3400%.

In 1990, Datta and Das [39] proposed the Datta-Das spin field-effect transistor (SFET) which in the following became a prototypical spintronic device scheme. This transistor is based on spin injection and spin detection performed by a ferromagnetic source and drain, and on spin precession about the built-in structure inversion asymmetry (Bychkov-Rashba) field Ω, in the asymmetric quasi-one dimensional channel of an ordinary field-effect transistor. The attractive feature of the Datta-Das SFET is that spin-dependent device operation is controlled not by external magnetic fields but by gate bias, which controls the spin precession rate.

Afterward, various spin transistors that contain metallic (and insulating) regions have been proposed by Bauer [123], Johnson [124], You and Bader [125], Zvezdin [126]. There is also a large category of the spin single-electron transistors, first realized by Ono [127], and later investigated by Barnas and Fert [128], Ciorga [129], Korotkov and Safarov [130], Martinek [131]. It is not the aim of this work to present all these results obtained in details in the present work.

However, here we would like to concentrate our attention on a model of Magnetic Bipolar Transistor (MBT) proposed by Zutic and Fabian in 2002. Within this model both equilibrium spin due to spin-split carrier bands and a nonequilibrium source spin introduced, for example, by external electrical spin injection or optical orientation should be considered in MBT [6, 61]. The equilibrium spin can be a result of the Zeeman splitting in an applied magnetic field or the exchange splitting due to ferromagnetic semiconductors integrated into the device structure.

A related device structure was already proposed in 1997 by Gregg [132] in a push for silicon-based spintronics. In that work a semiconductor has no equilibrium spin, and the spin source is provided by a ferromagnetic spin injector attached to the emitter, while another ferromagnetic metal, a spin detector, is attached to the base-collector junction to modulate the current flow. In both configurations the aim is to control current amplification by spin and magnetic field.

On the other hand, Zutic and Fabian considered *n*-*p*-*n* structure with magnetic *p*-type base region with the spin splitting $2q\xi_p$, which was doped with N_{Ab} acceptors, and nonmagnetic *n*-type emitter and collector terminals with concentration of donors N_{De} and N_{Dc} in the emitter and in the collector, respectively. A scheme of this MBT is shown in Fig. 1.17.

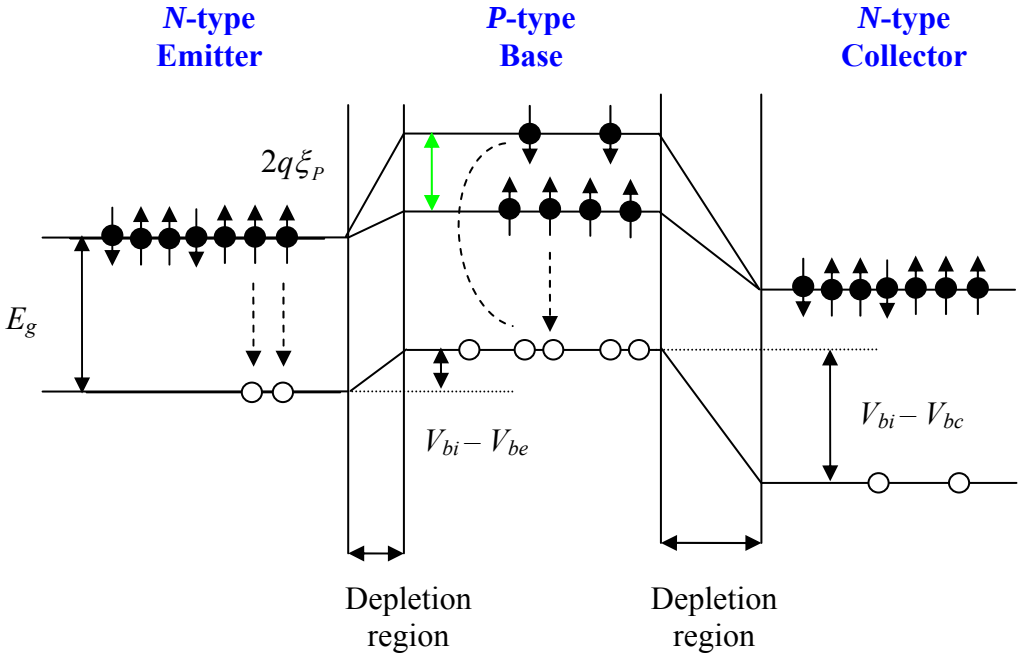

Figure 1.17 The scheme of a *n-p-n* transistor with a magnetic base region in the amplification mode.

In this model the following assumptions have been made. First of all, only electrons are taken to be spin polarized. In many important semiconductors (for example, such as GaAs) holes lose their spin orientation very fast [133] and, indeed, can be treated as unpolarized. Secondly, the electron-hole recombination was assumed to occur mostly in the emitter region whereas the base is spin independent. This is a reasonable approximation for unpolarized holes. Thirdly, the spin splitting is believed to be uniform in the bulk regions, eliminating magnetic drift and the source spin is injected into the emitter within the spin-diffusion length from the emitter-base *(b-e)* depletion layer so that enough spin can diffuse to the base. Other assumptions are those of the standard Shockley theory [134]. Then, electrical properties of such MBT are determined by both charge and spin of current carriers. For that purpose it is enough to know the minority electron densities n_{be} and n_{bc} to determine the electron charge currents, and p_e and p_c to determine the hole charge currents. The spin current j_s is the difference between the charge currents formed by the spin-up and spin-down electrons and the total charge current *j*. In these considerations the amplification mode of operation of the MBT was used. Based on theory of magnetic *p-n* junction electron n_{be} and spin s_{be} densities at the *b-e* region at the depletion layer edge [5] can be determined as:

$$n_{be} = n_{0b} \exp(\frac{qV_{be}}{k_B T})(1 + \alpha_e \alpha_{0b}) \tag{1.37}$$

$$s_{be} = n_{0b} \exp(\frac{qV_{be}}{k_B T})(\alpha_{0b} + \alpha_e), \tag{1.38}$$

where $\alpha_{0b} = \tanh(\frac{q\xi}{k_B T})$ is equilibrium spin polarization in the base, $n_{0b} = \frac{n_i^2}{N_{Ab}\sqrt{1-\alpha_{0b}^2}}$ is equilibrium number of electrons in the base, α_e is the nonequilibrium spin polarization injected externally into the emitter, V_{be} is applied voltage to the *b*-*e* junction, T is the absolute temperature, k_B is Boltzmann constant, n_i is intrinsic density.

In Ref. [6] Zutic and Fabian demonstrated that all expressions for currents from the Shockley theory of bipolar transistor, which are written in a general form, can be also applicable to MBT's. Then the emitter current in MBT can be written as:

$$j_e = j_{gb}^n(\frac{n_{be}}{n_{0b}}) + j_{ge}^p(\frac{p_e}{p_{0e}}), \tag{1.39}$$

where the electron generation current is $j_{gb}^n = (\frac{qD_n}{L_n}) n_{0b} \coth(\frac{w_b}{L_n})$, the hole generation current is $j_{ge}^p = (\frac{qD_p}{L_p}) p_{0e} \coth(\frac{w_e}{L_p})$, and the injected hole density in the emitter is $p_e = p_{0e} \exp(\frac{qV_{be}}{k_B T})$. Here L_n *(L_p)* is electron (hole) diffusion length, D_n *(D_p)* is electron (hole) diffusivities, w_b is the width of the base region, p_{0e} is equilibrium number of holes in the emitter.

The collector current is comprised only of electrons

$$j_c = j_{gb}^n(\frac{n_{be}}{n_{0b}}) \cosh(\frac{w_b}{L_n}), \tag{1.40}$$

Evaluating $j_b = j_e - j_c$ the current amplification coefficient (gain) β_0 can be defined as the ratio of the large collector current to the small base current. For practical transistors β_0 is order of 100, which means that small variations in j_b (input signal) lead to large variations

in j_c (output signal). One should notice that this ratio depends on a lot of factors, such as doping density, carrier lifetime, diffusion coefficient, and structure geometry. Zutic and Fabian showed that β_0 in a case of MBT also depends on spin splitting and nonequilibrium polarization.

$$\beta_0 = \frac{1}{(\alpha_T^{'} + \gamma^{'})}, \tag{1.41}$$

where $\alpha_T^{'} = \frac{1}{2}(\frac{w_b}{L_n})^2$ and $\gamma^{'} = \frac{N_{Ab} D_p}{N_{De} D_n} \frac{w_b}{L_p \tanh(\frac{w_e}{L_p})} \frac{\sqrt{1-\alpha_{0b}^2}}{(1+\alpha_e \alpha_{0b})}$.

The factor $\alpha_T^{'}$ determines how much electrons will recombine in the base, thus not reaching the collector. This factor is not affected by the presence of spin, and is the same as in the standard transistors. On the other hand, $\gamma^{'}$ is related to the emitter injection efficiency, since it measures the proportion of the electron flow in the emitter current (where both electrons and holes contribute). This factor does depend on the spin. To get the maximum amplification, both $\alpha_T^{'}$ and $\gamma^{'}$ need to be small. For the most efficient spin control of β_0, one needs $\alpha_T^{'} \le \gamma^{'}$.

The spin current density in the collector can be described by the following equation:

$$j_{sc} = \frac{qD_n}{L_s} \coth(\frac{w_c}{L_s}) \delta s_c, \tag{1.42}$$

where L_s is spin diffusion length, w_c and δs_c is the width and magnitude of the nonequilibrium spin in the collector region

Thus, one can also consider MBT as a magnetic heterostructure transistor, since its functionality depends on tunability of the band structure of the emitter, the base, or the collector. The advantage of MBT, however, is that the band structure is not built-in, but it can be tuned during the device operation by magnetic field or spin injection signals. In such structures spin can be injected through MBT's and current amplification can be controlled by the source and equilibrium spin, making MBT's attractive for spintronic applications.

1.5 Literature

[1] I. Zutic, J. Fabian, and S. Das Sarma, Phys. Rev. B **64**, 121201 (2001).

[2] I. Zutic, J. Fabian, and S. Das Sarma, Appl. Phys. Lett. **79**, 1558 (2001).

[3] I. Zutic, J. Fabian, and S. Das Sarma, Phys. Rev. Lett. **88**, 066603 (2002).

[4] I. Zutic, J. Supercond. **15**, 5 (2002).

[5] I. Zutic, Das Sarma, Phys. Rev. B **66**, 165301(2002).

[6] J. Fabian, I. Zutic and S. Das Sarma, Phys. Rev. B **69**, 115314 (2004).

[7] J. Fabian, I. Zutic, and S. Das Sarma, Appl. Phys. Lett. **84**, 85 (2004).

[8] M. Holub, P. Bhattacharya, J. Phys. D (Appl. Phys.) **40,** r179 (2007).

[9] R. Fiederling, M. Kleim, G. Reuscher, W. Ossau, G. Schmidt, A. Waag, and L. W. Molenkamp, Nature (London) **402**, 787 (1999).

[10] F. Meier and B. P. Zakharchenya, "*Optical Orientation*" (North-Holland, New York, 1984).

[11] A. G. Aronov and G. E. Pikus, Fiz. Tekh. Poluprovodn. **10**, 1177 (1976) (Sov. Phys. Semicond. **10**, 698 (1976)).

[12] M. Oestreich, J. Hubner, D. Hagele, P. J. Klar, W. Heimbrodt, W. W. Ruhle, D. E. Ashenford, and B. Lunn, Appl. Phys. Lett. **74**, 1251 (1999).

[13] Y. Ohno, D. K. Young, B. Beschoten, F. Matsukura, H. Ohno, and D. D. Awschalom, Nature (London) **402**, 790 (1999).

[14] B. T. Jonker, Y. D. Park, B. R. Bennett, H. D. Cheong, G. Kioseoglou, and A. Petrou, Phys. Rev. B **62**, 8180 (2000).

[15] P.R. Hammar, B. R. Bennett, M. J. Yang, and M. Johnson, Phys. Rev. Lett. **83**, 203 (1999).

[16] H. J. Zhu, M. Ramsteiner, H. Kostial, M. Wassermeier, H. P. Schonherr, and K.H. Ploog, Phys. Rev. Lett. **87**, 016601 (2001).

[17] V. Dediu, M. Murgia, F. C. Matacotta, C. Taliani, and S. Barbanera, Solid State Commun. **122**, 181 (2002).

[18] C. M. Hu, J. Nitta, A. Jensen, J. B. Hansen, and H. Takayanagi, Phys. Rev. B **63**, 125333 (2001).

[19] P. R. Hammar and M. Johnson, Appl. Phys. Lett. **79**, 2591 (2001).

[20] A. T. Hanbicki, B. T. Jonker, G. Itskos, G. Kioseoglou, and A. Petrou, Appl. Phys. Lett. **80**, 1240 (2002).

[21] V. F. Motsnyi, V. I. Safarov, J. De Boeck, J. Das, W. Van Roy, E. Goovaerts, and G. Borghs, Appl. Phys. Lett. **81**, 265 (2002).

[22] S. van Dijken, X. Jiang, and S. S. P. Parkin, Appl. Phys. Lett. **80**, 3364 (2002).

[23] D. Hagele, M. Ostreich, W. W. Ruhle, N. Nestle, and K. Eberl, Appl. Phys. Lett. **73**, 1580 (1998).

[24] J. M. Kikkawa and D. D. Awschalom, Nature (London) **397**, 139 (1999).

[25] A. Hirohata, Y. B. Xu, C. M. Guertler, J. A. C. Bland, and S. N. Holmes, Phys. Rev. B **63**, 104425 (2001).

[26] A. F. Isakovic, D. M. Carr, J. Strand, B. D. Schultz, C. J. Palmstrom, and P. A. Crowell, Phys. Rev. B **64**, 161304 (2001).

[27] G. Schmidt, G. Richter, P. Grabs, C. Gould, D. Ferrand, and L. W. Molenkamp, Phys. Rev. Lett. **87**, 227203 (2001).

[28] S. D. Ganichev, E. L. Ivchenko, S. N. Danilov, J. Eroms, W. Wegscheider, D. Weiss, and W. Prettl, Phys. Rev. Lett. **86**, 4358 (2001).

[29] G. Schmidt, D. Ferrand, L. W. Molenkamp, A. T. Filip, and B. J. van Wees, Phys. Rev. B **62**, 4790 (2000).

[30] E. I. Rashba, Phys. Rev. B **62**, 16 267 (2000).

[31] D. L. Smith and R. N. Silver, Phys. Rev. B **64**, 045323 (2001).

[32] A. Fert and H. Jaffres, Phys. Rev. B **64**, 184420 (2001).

[33] C.-M. Hu and T. Matsuyama, Phys. Rev. Lett. **87**, 066803 (2001).

[34] R. H. Silsbee, Phys. Rev. B **63**, 155305 (2001).

[35] E. I. Rashba, Appl. Phys. Lett. **80**, 2329 (2002).

[36] S. Das Sarma, J. Fabian, X. Hu, and I. Zutic, *58th DRC (Device Research Conference) Conference Digest* IEEE, Piscataway (2000).

[37] H. X. Tang, F. G. Monzon, R. Lifshitz, M. C. Cross, and M. L. Roukes, Phys. Rev. B **61**, 4437 (2000).

[38] M. E. Flatte and J. M. Byers, Phys. Rev. Lett. **84**, 4220 (2000).

[39] K. Flensberg, T. S. Jensen, and N. A. Mortensen, Phys. Rev. B **64**, 245308 (2001).

[40] S. Datta and B. Das, Appl. Phys. Lett. **56**, 665 (1990).

[41] S. Gardelis, C. G. Smith, C. H. W. Barnes, E. H. Linfield, and D. A. Ritchie, Phys. Rev. B **60**, 7764 (1999).

[42] Th. Schapers, J. Nitta, H. B. Heersche, and H. Takayanagi, Phys. Rev. B **64**, 125314 (2001).

[43] J. Carlos Egues, Phys. Rev. Lett. **80**, 4578 (1998).

[44] A. E. de Andrada e Silva and G. C. La Rocca, Phys. Rev. B **59**, 15 583 (1999).

[45] G. Kirczenow, Phys. Rev. B **63**, 054422 (2001).

[46] Y. Guo, J.-Q. Lu, B.-L. Gu, and Y. Kawazoe, Phys. Rev. B **64**, 155312 (2001).

[47] A. A. Kiselev and K. W. Kim, Appl. Phys. Lett. **78**, 775 (2001).

[48] A. L. Efros, E. I. Rashba, and M. Rosen, Phys. Rev. Lett. **87**, 206601 (2001).

[49] T. Matsuyama, C.-M. Hu, D. Grundler, G. Meier, and U. Merkt, Phys. Rev. B **65**, 155322 (2002).

[50] M. Governale, D. Boese, U. Zu¨licke, and C. Schroll, Phys. Rev. B **65**, 140403 (2002).

[51] J. Wrobel, T. Dietl, K. Fronc, A. Lusakowski, M. Czeczott, G. Grabecki, R. Hey, and K. H. Ploog, Physica E (Amsterdam) **10**, 91 (2001).

[52] T. Koga, J. Nitta, H. Takayanagi, and S. Datta, Phys. Rev. Lett. **88**, 126601 (2002).

[53] I. Zutic and S. Das Sarma, Phys. Rev. B **60**, R16322 (1999).

[54] A. G. Petukhov, Appl. Surf. Sci. **1230124**, 385 (1998).

[55] M. E. Flatte and G. Vignale, Appl. Phys. Lett. **78**, 1273 (2001).

[56] D. Frustaglia, M. Hentschel, and K. Richter, Phys. Rev. Lett. **87**, 256602 (2001).

[57] S. K. Joshi, D. Sahoo, and A. M. Jayannavar, Phys. Rev. B **64**, 075320 (2001).

[58] M. I. D'yakonov and V. I. Perel, Phys. Lett. **35A**, 459 (1971).

[59] M. I. D'yakonov and V. I. Perel, Pis'ma Zh. Eksp. Teor. Fiz. **13**, 657 (1971) (JETP Lett. **13**, 467 (1971)).

[60] J. E. Hirsch, Phys. Rev. Lett. **83**, 1834 (1999).

[61] R. D. R. Bhat and J. E. Sipe, Phys. Rev. Lett. **85**, 5432 (2000).

[62] J. Fabian, I. Zutic and S. Das Sarma, Appl. Phys. Lett. **84**, 85 (2003).

[63] A. Y. Cho, J. Vac. Sci. Technol. **8**, 31 (1971).

[64] W. D. Lawson, S. Nielsen, E. H. Putley and A. S. Young, J. Phys. Chem. Solids **9**, 325 (1959).

[65] C. Herring, Phys. Rev. **57**, 1169 (1940).

[66] L. C. Allen, Phys. Rev. **98**, 993 (1955).

[67] J. Chelikowsky and M.L. Cohen, Phys. Rev. B, **14**, 556 (1976).

[68] C. Konak, Phys. Stat. Solidi **3**, 1274 (1963).

[69] V. V. Karmazin and V. K. Miloslavskii, Fiz. Tech. Poluprovodn. **5,** 1048 (1971).

[70] M. Nawrocki, A. Twardowski, Phys. Stat. Solidi (B) **97**, k61 (1980).

[71] M. Costato, C. Jacobini and L. Reggiani, Phys. Stat. Solidi (B) **52**, 461 (1972).

[72] I. Strzalkowski, S. Joshi and C. R. Crowell, Appl. Phys. Lett. **28**, 15 (1976).

[73] J. Kossut, J. K. Furdyna Semiconductor and Semimetals vol. **25** (Academic press Inc., 1988).

[74] J. Furdyna, J. Appl. Phys. **64**, 4 (1988).

[75] J. Gaj, R. Planel and G. Fishman, Sol. State Commun. **29**, 435 (1978).

[76] J. Gaj, J. Ginter and R.R. Gałązka, Phys. Stat. Sol. (b) **89**, 655 (1978).

[77] J. Gaj, W. Grieshaber, C. Bodin-Deshayes and J. Cibert, Phys. Rev. B **50**, 5512 (1994).

[78] R. N. Bicknell, N. C. Giles and J. F. Schetzina, Appl. Phys. Lett. **49**, 1095 (1986).

[79] F. Bassani, S. Tatarenko, K. Saminadayar, J. Bleuse, N. Magnea and J. L. Pautrat, Appl. Phys. Lett. **58**, 2651 (1991).

[80] D. Ashenford, P. Devine, J. H. Hogg, B. Lunn and C. G. Scott, J. Phys. Condens. Matter **3,** s245 (1991).

[81] D. Rajavel and C. J. Summers, Appl. Phys. Lett. **60,** 2331 (1991).

[82] S. Seto , A.Tanaka, Y. Masa and M. Kawashima, J. cyst. Growth **117**, 271 (1992).

[83] F. Bassani, K. Saminadayar, S. Tatarenko, K. Kheng, R. T. Cox and N. Magnea, J. Cryst. Growth **117**, 391 (1992).

[84] F. Bassani, S. Tatarenko, K. Saminadayar, N. Magnea, R. T. Cox, A. Tardot and C. Grattepain, J. Appl. Phys. **72**, 2927 (1992).

[85] D. Hommel, A. Waag, S. Scholl and G. Landwehr, Appl. Phys. Lett. **61,** 1546 (1992).

[86] F. Bassani, S. Tatarenko, K. Saminadayar and C. Grattepain, Mater. Sci. Eng. B **16,** (1993).

[87] A. Waag, S. Scholl, K. von Schierstedt, D. Hommel, G. Landwehr and G. Bilger, J. Cryst. Growth **129**, 243 (1993).

[88] A. Waag, Th. Litz, F. Fischer, H. Heinke, S. Scholl, D. Hommel and G. Landwehr, J. Cryst. Growth **138**, 437 (1994).

[89] D. Hommel, S. Scholl, T. A. Kuhn, W. Ossau, A. Waag and G. Landwehr, Mater. Sci. Eng. B **16**,178 (1993).

[90] A. Waag, F. Fisher, J. Gerschutz, S. Scholl, and G. Landwehr, J. Appl. Phys. **75**, 1369 (1994).

[91] G. Karczewski, J. Jaroszynski, M. Kutrowski, A. Barcz, T. Wojtowicz and J. Kossut, Acta Phys. Pol. A **92**, 829 (1997).

[92] F. Fisher, A. Waag, G. Bilger, Th. Litz, S. Scholl, M. Schmitt, G. Landwehr, J. Cryst. Growth **141**, 93 (1994).

[93] R. N. Bicknell, N. C. Giles and J. F. Schetzina, Appl. Phys. Lett. **49**, 1735 (1986).

[94] K. Kitagawa, T. Mishima and K. Takahshi, J. Electrochem. Soc. **127**, 937 (1981).

[95] R. L. Harper, S. Hwang, N. C. Giles, J. F. Schetzina, D. L. Dreifus and T. H. Myers, Appl. Phys. Lett. **54**, 170 (1989).

[96] J. Han, T. S. Stavrinedes, M. Kobayashi, R. L. Gunshor, M. M. Hagerott and A. V. Numikko, Appl. Phys. Lett. **62**, 840, (1993).

[97] K. A. Dhese, P. Devine, D. E. Ashenford, J. E. Nicholls, C. G. Scott, D. Sands and B. Lunn, J. Appl. Phys. **76**, 5423 (1994).

[98] T. Baron, K. Saminadayar and N. Magnea, J. Appl. Phys. **83**, 1354 (1998).

[99] I. Solomon, Solid State Commun. **20**, 215 (1976).

[100] D. J. Lepine, Phys. Rev. B **6**, 436 (1972).

[101] E. Johnston-Halperin, D. Lofgreen, R. K. Kawakami, D. K. Young, L. Coldren, A. C. Gossard and D. D. Awschalom, Phys. Rev. B **65**, 041306 (2002).

[102] M. Kohda, Y. Ohno, K. Takamura, F. Matsukura, H Ohno, Jpn. J. Appl. Phys. **40**, L1274 (2001).

[103] P. Van Dorpe, Z. Liu, W. V. Roy, V. F. Motsnyi, M. Sawicki, G. Borghs, J. De Boeck Appl. Phys. Lett. **84** (18), 3495 (2004).

[104] L. Esaki, P. Stiles, and S. von Molnar, Phys. Rev. Lett. **19,** 852, (1967).

[105] T. Kasuya and A. Yanase, Rev. Mod. Phys. **40**, 684, (1968).

[106] E. L. Nagaev, "*Physics of Magnetic Semiconductor*" (Mir, Moscow, 1983).

[107] S. von Molnar, S. Methfess, J. Appl. Phys. **38**, 959 (1967).

[108] J. C. Egues, Phys. Rev. Lett. **80**, 4578 (1998).

[109] L. Borda, G. Zarand, W. Hofstetter, B. I. Halperin, J. von Delft, Phys. Rev. Lett. **90**, 026602 (2003).

[110] M. M. Deshmukh and D. C. Ralph, Phys. Rev. Lett. **89**, 266803 (2002).

[111] P. Recher, E. V. Sukhorukov, D. Loss, Phys. Rev. Lett. **85**, 1962 (2000).

[112] D. P. DiVincenzo, Fortschr. Phys. **48**, 771 (2000).

[113] R. H. Silsbee, Bull, Magn. Reson. **2**, 284 (1980).

[114] M. Johnson, and R. H. Silsbee, Phys. Rev. Lett. **55**, 1790 (1985).

[115] S. Tiwari, "*Compound Semiconductor Device Physics*" (Academic Press, San Diego, 1992).

[116] M. Johnson, R. H. Silsbee, Phys. Rev. B **35**, 4959 (1987).

[117] C. P. Wen, B. Hershenov, H. von Philipsborn, H. L. Pinch, IEEE Trans. Magn**. 4**, 702 (1968).

[118] Y. Ohno, I. Arata, F. Matsukura, K. Ohtani, S. Wang, and H. Ohno, Appl. Surface Sc. **159-160**, 308 (2000).

[119] F. J. Teran, L. X. Zhao, A. Patane, R. P. Campion, C. T. Foxon, L. Eaves, B. L. Gallagher, Appl. Phys. Lett. **83**, 866 (2003).

[120] F. Tsui, L. Ma, L. He, Appl. Phys. Lett. **83**, 954 (2003).

[121] S. van Dijken, X. Jiang, and S. S. P. Parkin, Phys. Rev. Lett. **90**, 197203 (2003).

[122] X. Jiang, R. Wang, S. van Dijken, R. Shelby, R. Macfarlane, G. S. Solomon, J. Harris, and S. S. P. Parkin, Phys. Rev. Lett. **90**, 256603 (2003).

[123] G. E. W. Bauer, A. Brataas, and Y. Tserkovnyak, B. J. van Wees, Appl. Phys. Lett. **82**, 3928 (2003).

[124] M. Johnson, Scince **260**, 320 (1993).

[125] C. Y. You, S. D. Bader, J. Appl. Phys. **87**, 5215 (2000).

[126] A. K. Zvezdin, A. S. Mischenko, and A. V. Khval'kovskii, Zh. Tekhn. Fiz. **48**, 53 (2003).

[127] K. Ono, H. Shimada, S. Kobayashi, and Y. Outuka, J. Phys. Soc. Jpn. **65**, 3449 (1996).

[128] J. Barnas, A. Fert, Phys. Rev. Lett. **80**, 1058 (1998).

[129] M. Ciorga, M. Pioro-Ladriere, P. Zawadzki, P. Hawrylak, and A. S. Sachrajda, Appl. Phys. Lett. **80**, 2177 (2002).

[130] A. N. Korotkov, and V. I. Safarov, Phys. Rev. B **59**, 89 (1999).

[131] J. Martinek, J. Barnas, S. Maekawa, H. Schoeller, and G. Schon, Phys. Rev. B **66**, 014402 (2002).

[132] J. Gregg, W. Allen, N. Viart, R. Kirschman, C. S. J.-P. Schille, M. Gester, S. Thompson, P. Sparks, V. Da Costa, K. Ounadjela, and M. Skvarla, J. Magn. Mater. **175**, 1 (1997).

[133] D. J. Hilton, C. L. Tang, Phys. Rev. Lett. **89**, 146601 (2002).

[134] W. Shockley, "*Electron and holes in Semiconductors*" (Van Nostrand Princeton, 1950).

Chapter 2. Experimental Techniques

2.1 Details of the MBE process

In the present work all structures investigated were grown in the EPI-620 MBE system consisted of two main chambers. The first one is the load-lock ultra high vacuum (UHV) chamber (typical pressure 10^{-10}-10^{-9} torr), which uses for loading substrates without breaking the vacuum environment. The second one is the growth chamber with a typical pressure about 10^{-10} torr inside it. Both of these chambers are connected via the UHV valve. The UHV inside the MBE system is achieved using cryo- and turbo molecular pumps (with a pumping speed of 1500 l/s), which are connected directly to these chambers. In addition, one should notice that the growth chamber is cooled down with liquid nitrogen. The sources and the growth environment need to be surrounded by liquid-nitrogen-cooled cryopanels to minimize unintentional impurity incorporation in the deposited layers from the residual background, while the whole system is confined within a UHV environment. Molecular beams are being generated from six thermal elemental effusion cell sources of high purity materials: Cd, Te, Mn, Mg, Zn and ZnI2 (used for *n*-type doping) which were installed in the growth chamber. For *p*-type doping, a RF-plasma source of excited nitrogen plasma has been used. One should notice that this latter source has a special water-cooling system and ultra pure nitrogen gas (10^{-6}) line.

In the present thesis all samples were fabricated in Cd overpressure atmosphere. The beam equivalent pressure ratio P(Cd)/P(Te) or P(Cd+X)/P(Te) or P(Cd+X+Y)/P(Te) (where X and Y are Zn or Mn or Mg) of molecular fluxes was kept at a value of 1.1 during the whole growth procedure. The substrate temperature during the growth process was kept about 250-270°C which results in the growth rate of 0.6-0.8 μm/h. To control the doping level in *n*-type material the temperature of ZnI_2 effusion cell was varied from 160^0C to 190^0C. This changes the concentration of electrons from 1.5×10^{17} cm^{-3} to 3×10^{18} cm^{-3}. On the other hand, for *p*-type doping the RF power was usually changed from 150 W to 450 W which results in the doping level of 1.6×10^{17} cm^{-3} and 8×10^{18} cm^{-3}, respectively.

2.2 Influence of lattice mismatch on the sample quality

High quality (100)-oriented semi-insulating or n^+ Si-doped GaAs crystals were used as

a substrate in the present work. Prior to the growth process, the protective oxide layer has been removed from the substrate by thermal annealing. During the thermal treatment the surface of the GaAs substrate was controlled by the RHEED technique.

In heteroepitaxial systems, where a close lattice match is achieved over a limited range of compositions, the quality of the epitaxial layers depends critically on the degree of the lattice parameter mismatch and the composition uniformity over the substrate area. Depending on the alloy system, the maximal values of the lattice mismatch that can be accommodated by elastic strain in layers lie in the range:

$$\delta = (a_{epi} - a_{sub})/a_{sub} \leq 1 \text{ to } 2 * 10^{-3}, \qquad (2.1)$$

where a_{epi} and a_{sub} represent the epitaxial layer and substrate lattice constants, respectively.

As mentioned above, in the present thesis the main attention will be focused on CdTe which is one of the basic compounds of II-VI group semiconductors with numerous technological applications. One should also notice that GaAs was usually used as a substrate on which all structures investigated have been fabricated. The lattice mismatch between CdTe (lattice constant a = 6.48 Å) and GaAs (lattice constant a = 5.653 Å) is very large 14.6%.

For such large lattice mismatch, extensive arrays of misfit dislocations are generated at the interface and propagate throughout the layer. There are several techniques to diminish the effects of lattice mismatch:

a) Growth of a continuously graded buffer layers

b) Step graded growth, resulting in partial confinement of the misfit dislocations at intermediate interfaces

c) Growth of superlattice dislocations barriers on top of graded buffer layers

d) Growth of homogeneous buffer layer

The use of several micrometers thick buffer layer between substrate and the structure leads to significant improvement of the sample stability, making a degradation process much less essential than in samples with thin or without buffer layers. Following this idea, the homogeneous undoped CdTe buffer layer was grown on the top of the substrate to improve the quality of the structures investigated in the present work. The thickness of the buffer layer was typically in the range of 4-5 μm.

2.3 MBE growth process using flux monitor technique

When the magnetic transistor is fabricated one of the main problems is linked with formation of electrical contacts to the emitter and base regions which are usually buried and there is no direct way in order to form such contacts. The situation is even more complicated, because the thickness of the base region is typically very small (about hundreds nanometers). In this case, in order to make a good Ohmic contact it is necessary to etch the upper layers, what is very long and laborious process. Thus, instead of etching we use the flux monitor during the MBE growth procedure which allows us to create a way out for possible electrical contacts immediately during the process of the sample fabrication. The essence of this technique is illustrated in Fig. 2.1.

Molecular beam epitaxy implies that the flow of components from the source to the substrate is in the molecular not hydrodynamic flow region. Thus, the beams can be considered as unidirectional with negligible interaction within them. A mechanical shutter, which is located in front of the effusion cell, can stop the beam before it reaches the substrate. Moreover, the shutter can be fixed to the flux monitor, and as a consequence, this allows to fabricate the structures with very small areas, which could have uncontrolled composition of the different species. In this case the shutter should be placed as close to the surface as possible. On the other hand, this can lead to disturbance of temperature of the substrate and, accordingly, the growth condition can change rapidly as well. Thus, the position of the shutter relative to the substrate should be optimized avoiding the undesirable effects such as, for example, inhomogeneity of the structure. Covering with the shutter the necessary part of the structure (as shown in Figs. 2.1 (a) and (c)) the *n-p-n* spin transistors with a magnetic base and nonmagnetic emitter and collector regions can be grown.

It is necessary to note that the substrate was not being rotated during the growth process of the *n*-type region while it was being rotated during the growth of the *p*-type region. However, this fact has a minimal influence on the quality of the grown structures.

2.4 Low-temperature measurements in the magnetic field

In the present work all magneto-optical and magneto-transport measurements were carried out using a superconducting magnet, which consists of a concentric coil made from NbTi wire and creates a magnetic field up to 9 T, in the temperature range from 1.4 K to 300 K.

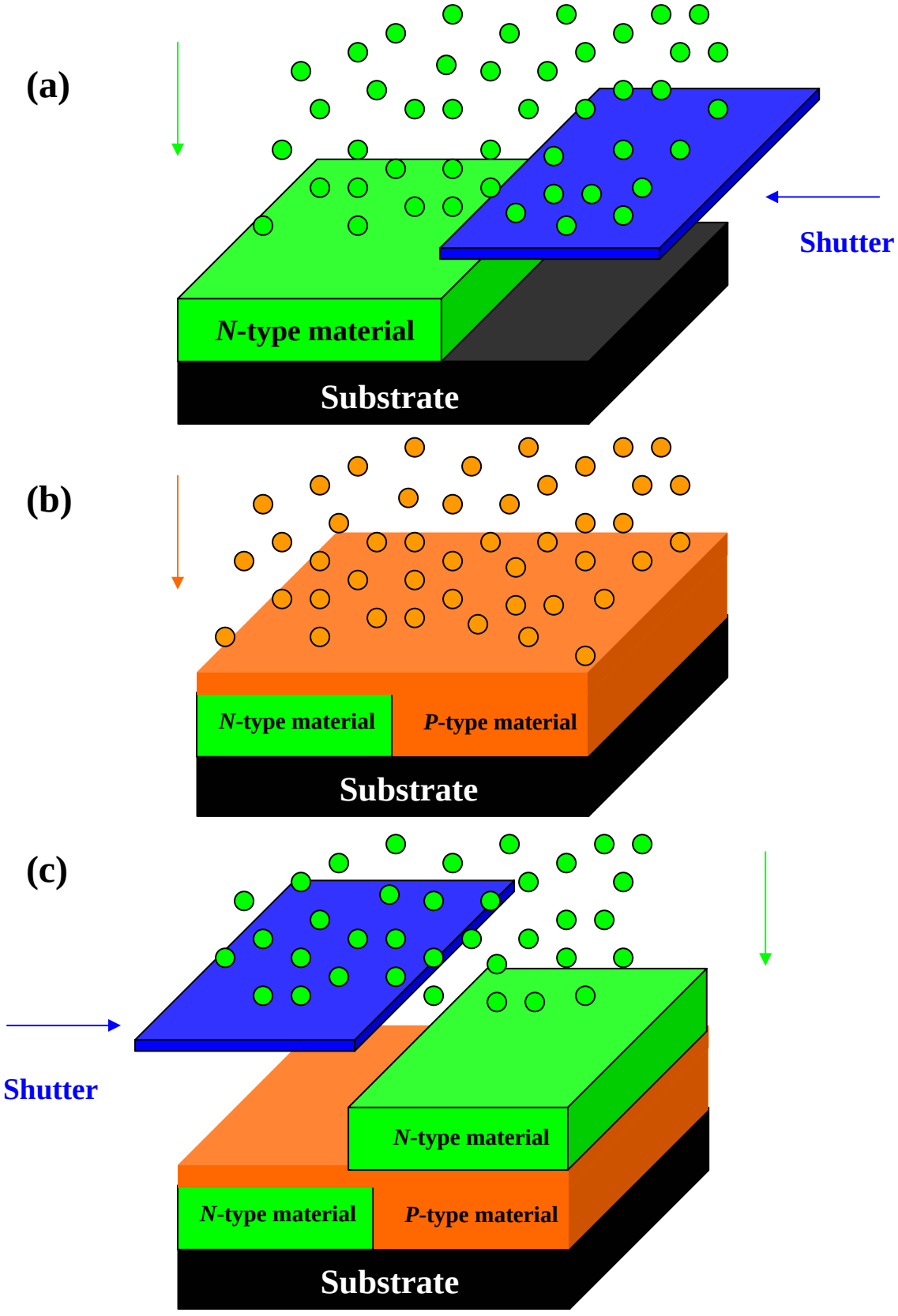

Figure 2.1 A scheme of fabrication of a *n-p-n* magnetic transistor by the MBE technique with the flux monitor.

The concentric coil is located in liquid He^4 cryostat. It is made of a nonmagnetic metal and consists of different concentric separated chambers. The outermost chamber is vacuum-pumped (about 10^{-6} bar) in order to make a good thermal insulation. The next chamber is used for cooling down with liquid nitrogen, whereas just behind the third vacuum-pumped chamber the tank for liquid helium is located.

Only tail of the cryostat goes to the bore of the magnet. During measurements the sample was mounted on the sample holder fixed in a way to be precisely in the center of the magnetic field.

Because the He recovery line has a slight overpressure against the ambient atmosphere, the He bath temperature is about T = 4.2 K. By pumping the He gas and reaching a pressure of about 1 mbar temperature drops to 1.3 K or 1.4 K. Below the λ-point (T = 2.17 K) helium changes its properties and becomes superfluid. For our optical measurements it is important that the He liquid becomes smooth and transparent in the superfluid phase.

In order to reach higher temperatures than 4.2 K we used a heater consisting of a copper tube, containing the sample. A Manganin wire ($Cu_{0.86}Mn_{0.12}Ni_{0.02}$) was antiparallelly wound called bifilar, around the tube, i.e., the current which is sent through the wire for heating purposes turns first clockwisely and then counterclockwisely, so that the two produced magnetic fields cancel each other. In order to get a higher temperature we put the sample in a closed tube filled with helium gas of a low pressure and sent a current through the heater. The measurements were carried out when the system had reached the thermal equilibrium.

In order to determine the temperature a gallium-aluminum-arsenide (GaAlAs) diode glued on the sample holder (about 2 cm from the sample) was used.

2.5 Transport measurements

The electrical parameters of magnetic diodes and magnetic bipolar transistors were determined from capacitance-voltage (*C-V*) and current-voltage (*I-V*) characteristics measured at different values of magnetic field in the temperature range from 1.4 K to 300 K. The pumped ^{4}He system with a superconducting magnet, Keithly 6221 DC and AC current source, and Keithly 2000 multimeter have been used for the magneto-transport measurements. The capacitance-voltage curves were recorded using Hewlett Packard 4275A

capacitance analyzer, which allows to measure capacitance in the range from 0.01 fF to 199.99 μF at different biases by superimposing an ac voltage on the dc voltage. In the present work, the bias applied to the structure varies in the range from -3 V to 1 V in steps of 0.01-0.1 V. The amplitude and the frequency of the ac voltage were 10 mV and 1 MHz, respectively. The current-voltage measurements were carried out using Keithley 6487 Picoammeter/Voltage source. The measuring range for current was from 2 nA to 20 mA with 5.5 digit default resolution, which let to register the current value from 10 fA. Similar to the C-V measurements the bias changes in the range from -3 V to 1 V in steps of 0.01-0.1 V. The sample temperature was detected by a gallium-aluminum-arsenide (GaAlAs) diode. The auto-tuning temperature controller LakeShore 340 was used to monitor the temperature. The accuracy of detection was ± 0.001 K.

2.6 Photoluminescence measurements

Photoluminescence (PL) measurements were performed using a 532 nm line of an semiconductor Nd:YAG-laser as an excitation source. For transmission of the excitation light and detection of the signal a single 600 μm thick optical fibre has been located between the sample and the standard optical set-up. The whole experimental set-up is depicted in Fig. 2.2.

As shown in Fig. 2.2 the excitation beam of the Nd:YAG-laser is focused with a microscope objective (collimator) onto the entrance of the optical fibre. In the cryostat, the fibre was fixed above the sample surface in order to avoid any movement due to the magnetic field. The continuous laser excitation was reflected at a small mirror and focused with a lens on a sample. The collected light beam was passed through the quarter wave plate and linear polarizer and was focused onto the entrance of the optical fibre. It should be emphasized that another fibre was used to detect the luminescence signal from the sample. The polarization of the luminescence was analyzed inside the cryostat using a combination of a foil quarter wave plate and a linear polarizer. Both σ^+ and σ^- components were obtained by reversing the sign of the magnetic field. The luminescence was dispersed in a monochromator and detected using CCD camera cooled with liquid nitrogen. A computer records the signal.

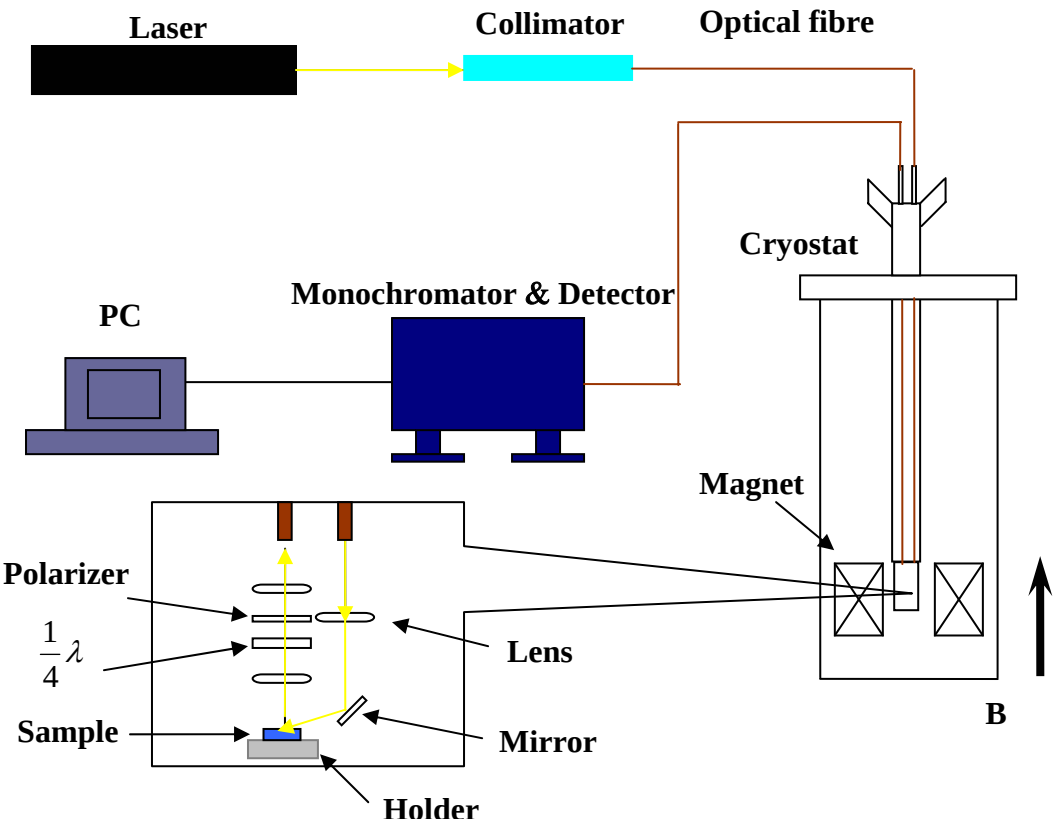

Figure 2.2 Schematic diagram of the magneto-Photoluminescence set up.

2.7 Electroluminescence measurements

Electroluminescence (EL) measurements were performed using the source of the electric current Arbitrary Waveform Generator Agilent 33250A, which can form different shapes of the output signal, with the frequency range up to 80 MHz. In the present investigation, trapezium form pulses with width of 300 μs and repetition frequency of 2 kHz were mainly used. The signal from the generator is given onto the input of amplifier circuit and then onto the sample. This circuit allows using the higher values of the forward and reverse bias (24 V and 16 V, correspondingly) comparing with the ones which could be obtained from the the Arbitrary Waveform Generator (10 V in both directions). Due to very high resistance at low temperatures, which is one of the inseparable features of the whole family of CdTe materials used in this work, the increase of the possible bias is very important, because the threshold for light emission process can be observed only at a high current level of about 40-200 mA. The collected light beam from the sample passes through a quarter wave plate and a linear polarizer. Finally it is focused onto the entrance

of an optical fibre as in the case of PL measurements and, then, the EL signal is dispersed in monochromator and detected using a CCD camera. The experimental set-up is depicted in Fig. 2.3.

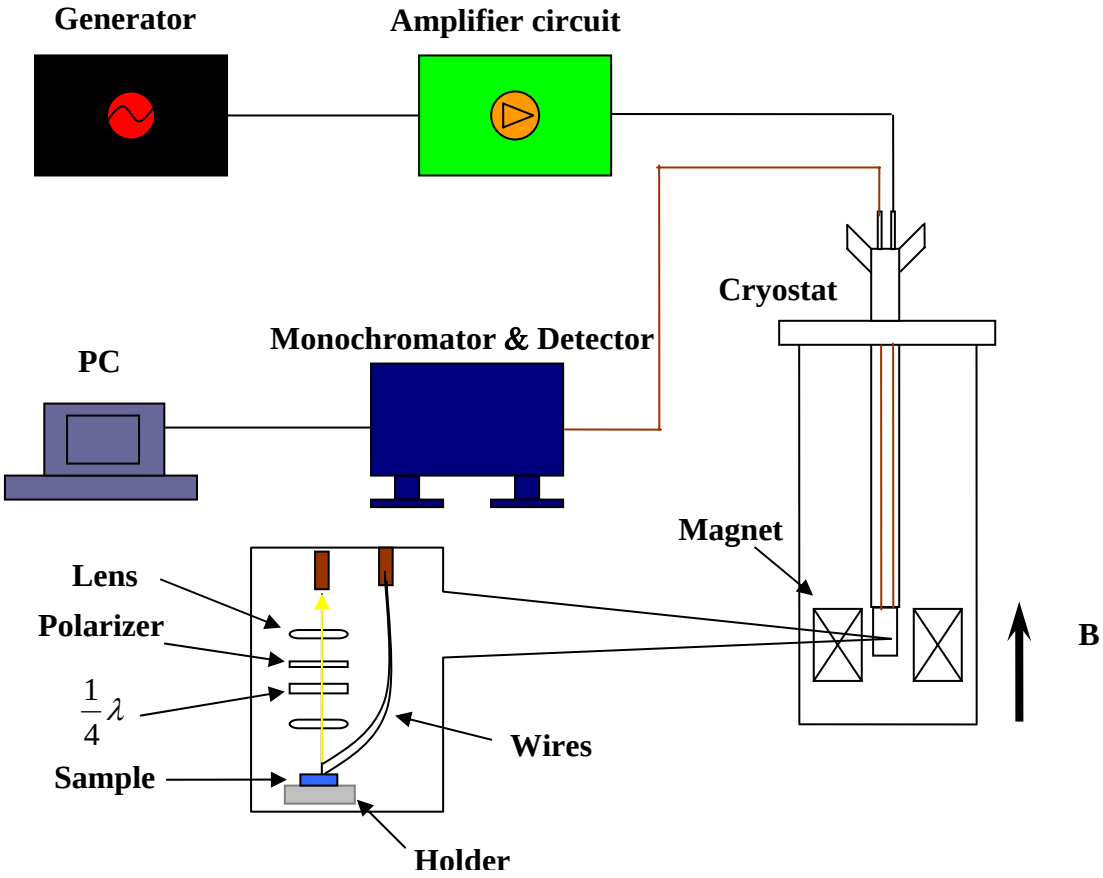

Figure 2.3 Schematic diagram of the Electroluminescence set up.

2.8 Hall effect measurements

Experimental determination of transport properties of a semiconductor requires some significant deviations from an ideal model. First of all, one cannot directly measure the electric field or the current density inside a sample. The current density is usually determined from the total excitation current and geometry of the sample. Electric field is determined by measuring voltage differences between electrical contacts on the surface of the sample. Electrical contacts are made of conductive material and they usually have a higher conductivity than the sample material itself. Electric current therefore tends to flow through the contacts rather than the sample, distorting the current density and electric field in the

sample from the ideal situation. Excitation current flowing through the contacts used to measure voltage differences reduces both current density in the vicinity and the Hall field. If a contact extends across the sample in the same direction as the Hall field, it can conduct current from one side of the sample to the other, shorting out the Hall voltage and leading to an underestimate of the Hall coefficient. Finally, if pairs of contacts used in a voltage measurement are not aligned properly either perpendicular or parallel to the excitation current density, then the voltages measured will not correctly determine the perpendicular or parallel component of the electric field. To minimize these geometrical problems, one must take care with the size and placement of electrical contacts to the sample. There are also many intrinsic physical mechanisms that alter current density and electric field behavior in a real material. Most of them relate to the thermoelectric behavior of the material in or out of a magnetic field. Some of these effects can be minimized by controlling temperature in the sample's vicinity to minimize thermal gradients across it. In addition, most errors introduced by intrinsic physical mechanisms can be canceled by reversing either the excitation current or the magnetic field and averaging measurements. Thus, all of this should be taken into account before the transport measurements can be performed.

Hall effect measurements commonly use two sample geometries: (a) long narrow Hall bar geometries and (b) nearly square or circular van der Pauw geometries. However, in both cases Hall voltage is developed perpendicular to a current and an applied magnetic flux.

In the present work we used six-contact 1-2-2-1 Hall bar geometry (Fig. 2.4).

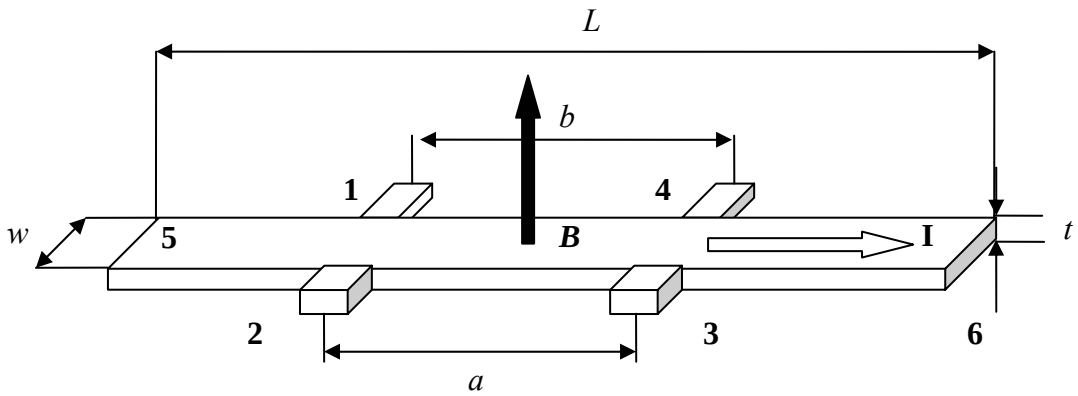

Figure 2.4 Six contact 1-2-2-1 Hall bar geometry.

Contact separations *a* and *b* on each side of the sample are equal with contacts located opposite one another. In this case, contact pairs are placed symmetrically about the midpoint of the sample long axis.

The Ohmic contacts were formed by annealing indium dots at 170^0C for about 20-30 s. All magneto-transport measurements were performed in perpendicular configuration, when direction of the magnetic field is perpendicular to the growth direction.

Chapter 3. Magnetic diodes

3.1 General concept of magnetic diodes

As mentioned above, Zutic and Fabian proposed two novel types of spintronic devices: magnetic *p*-*n* diode and magnetic bipolar transistor (MBT) [1-7].

The concept of the magnetic *p*-*n* junction is rather simple: one side of the junction (*n*- or *p*-type side) is made of a magnetic material exhibiting a giant spin splitting in the presence of an external magnetic field, while the other side of the junction (*p*- or *n*-type side, respectively) is made of a conventional, nonmagnetic semiconductor. Zutic and Fabian expected that due to the giant spin splitting which appears in the magnetic part of the *p*-*n* junction the following effects may appear: generation of a spin-polarized current, spin amplification, voltage control of spin polarization, and a significant extension of spin diffusion range. Additionally, some other phenomena can be also observed in magnetic diodes: exponential giant magnetoresistance, spin-valve effect, and spin-voltaic effect. However, the main condition for observation of these effects is the presence of nonequilibrium spins in the system [1-5].

Among various effects expected to show up in magnetic *p*-*n* junctions the magneto-voltaic effect deserves a particular attention. There are two reasons for that. Firstly, this effect was expected to appear only in magnetic diodes. Secondly, the experimental observation of the spin-voltaic effect should be rather simple.

According to Zutic and Fabian, the magneto-voltaic effect is an analogue of the well known photovoltaic effect, in which a strong current generation appears upon illumination of the junction area by the over-the-gap radiation. This strong photocurrent flows through the junction even when the diode is not electrically biased [8]. In the case of the magneto-voltaic effect one expects significant changes of the dark current flowing through a non-biased magnetic junction upon applying of the magnetic field. In this case the magnetic field influence on the dark current inducing a change of the effective potential barrier height of the *p*-*n* junction [5].

Inspired by the theoretical predictions of Zutic and Fabian, the first part of my work is devoted to construction and characterization of electrical and optical properties of magnetic *p*-*n* junctions made of II-VI diluted magnetic semiconductor (CdMnTe). The main goal is to verify in an experimental way the possibility of operation of such magnetic devices.

Particularly, the main focus will be concentrated on the experimental observation of the magneto-voltaic effect.

3.2 Practical realization of magnetic diodes

3.2.1 Schematic design of magnetic diode structures

In order to check both possible configurations of the magnetic diode in which either *n*- or *p*-type region is magnetic we fabricated two types of magnetic *p*-*n* junctions using the MBE technique. The first type of magnetic diodes, shown in Fig. 3.1 (a), consists of a magnetic *n*-type layer and a nonmagnetic *p*-type region. In this case magnetic CdMnTe was doped by iodine donors and a nitrogen-plasma doped CdZnTe layer plays as the nonmagnetic layer. In the second series of the magnetic *p*-*n* diode the *n*-type region was nonmagnetic (iodine doped CdTe) whereas the *p*-type region was magnetic (CdMnZnTe:N) as shown in Fig. 3.1 (b).

It is worthy to notice, that in both types of magnetic diodes the *p*-type region was located at the top of the structure. Such design of the diode has several advantages. First of all, without any further preparation as-grown *p*-type surface is ready for metallization and creation of Ohmic contacts. Secondly, *p*-type doping requires breaking of the ultra high vacuum in the growth chamber, so it should be made as the last step in any growth procedure. Thirdly, introduction of 9% of Zn into the *p*-type region significantly increases the lattice mismatch between layers. Thus, as clearly follows from these considerations it is the best to have the *p*-type region from the top of the structure.

Besides two series of magnetic diodes, sets of structures containing an intrinsic region between *p*- and *n*-type layers, i.e., *p*-*i*-*n* diodes, and magnetic or nonmagnetic quantum well (QW), i.e. light sources have been also grown and investigated in the present work. The *p*-*i*-*n* diodes and *p*-*n* junctions with a magnetic or nonmagnetic quantum well were fabricated in a similar way to the structures shown in Fig. 3.1 (b). However, an intrinsic layer of undoped CdMnTe (or QW) was introduced between the nonmagnetic *n*-type (CdTe) and *p*-type (CdZnTe) regions.

For the sake of clarity, all parameters of the magnetic *p*-*n* and *p*-*i*-*n* junctions grown and investigated within this thesis are combined in Table 3.1.

Samples	Concentration of Mn, %	*P*-type material	*N*-type material	Intrinsic layer width, Å	Concentration of electrons in *N*-type side (n_e), cm^{-3}	Concentration of holes in *P*-type side (n_h), cm^{-3}
N1	1	Nonmagnetic	Magnetic	No	1.5×10^{17}	2×10^{18}
N2	1	Nonmagnetic	Magnetic	No	2.75×10^{17}	2×10^{18}
N3	1	Nonmagnetic	Magnetic	No	3.7×10^{17}	2×10^{18}
N4	1	Nonmagnetic	Magnetic	No	7×10^{17}	2×10^{18}
N5	1	Nonmagnetic	Magnetic	No	1.2×10^{18}	2×10^{18}
N6	1	Nonmagnetic	Magnetic	No	3×10^{18}	2×10^{18}
N7	1	Nonmagnetic	Magnetic	No	7×10^{17}	1.6×10^{17}
N8	1	Nonmagnetic	Magnetic	No	7×10^{17}	3.2×10^{17}
N9	1	Nonmagnetic	Magnetic	No	7×10^{17}	8.7×10^{17}
N10	1	Nonmagnetic	Magnetic	No	7×10^{17}	1.5×10^{18}
N11	1	Nonmagnetic	Magnetic	No	7×10^{17}	2×10^{18}
N12	1	Nonmagnetic	Magnetic	No	7×10^{17}	5.3×10^{18}
N13	1	Nonmagnetic	Magnetic	No	7×10^{17}	8×10^{18}
N14	1	Magnetic	Nonmagnetic	No	7×10^{17}	8.7×10^{17}
N15	5	Magnetic	Nonmagnetic	No	7×10^{17}	8.7×10^{17}
N16	10	Magnetic	Nonmagnetic	No	7×10^{17}	8.7×10^{17}
N17	15	Magnetic	Nonmagnetic	No	7×10^{17}	8.7×10^{17}
N18	1	Nonmagnetic	Magnetic	No	7×10^{17}	8.7×10^{17}
N19	5	Nonmagnetic	Magnetic	No	7×10^{17}	8.7×10^{17}
N20	10	Nonmagnetic	Magnetic	No	7×10^{17}	8.7×10^{17}
N21	15	Nonmagnetic	Magnetic	No	7×10^{17}	8.7×10^{17}
N22	5	Nonmagnetic	Nonmagnetic	Yes, 200 (Magnetic)	7×10^{17}	8.7×10^{17}
N23	5	Nonmagnetic	Nonmagnetic	Yes, 400 (Magnetic)	7×10^{17}	8.7×10^{17}
N24	5	Nonmagnetic	Nonmagnetic	Yes, 600 (Magnetic)	7×10^{17}	8.7×10^{17}
N25	5	Nonmagnetic	Nonmagnetic	Yes, 800 (Magnetic)	7×10^{17}	8.7×10^{17}
N 26	10	Nonmagnetic	Nonmagnetic	Yes, 400 (Magnetic)	7×10^{17}	8.7×10^{17}
N28	1 (Barrier 500Å)	Nonmagnetic	Nonmagnetic	Yes, 100 (Magnetic QW)	7×10^{17}	8.7×10^{17}
N30	0 (Barrier 500Å)	Nonmagnetic	Nonmagnetic	Yes, 100 (Nonmagnetic QW)	7×10^{17}	8.7×10^{17}

Table 3.1 The list of the magnetic *p-n* and *p-i-n* junctions grown and investigated within this thesis.

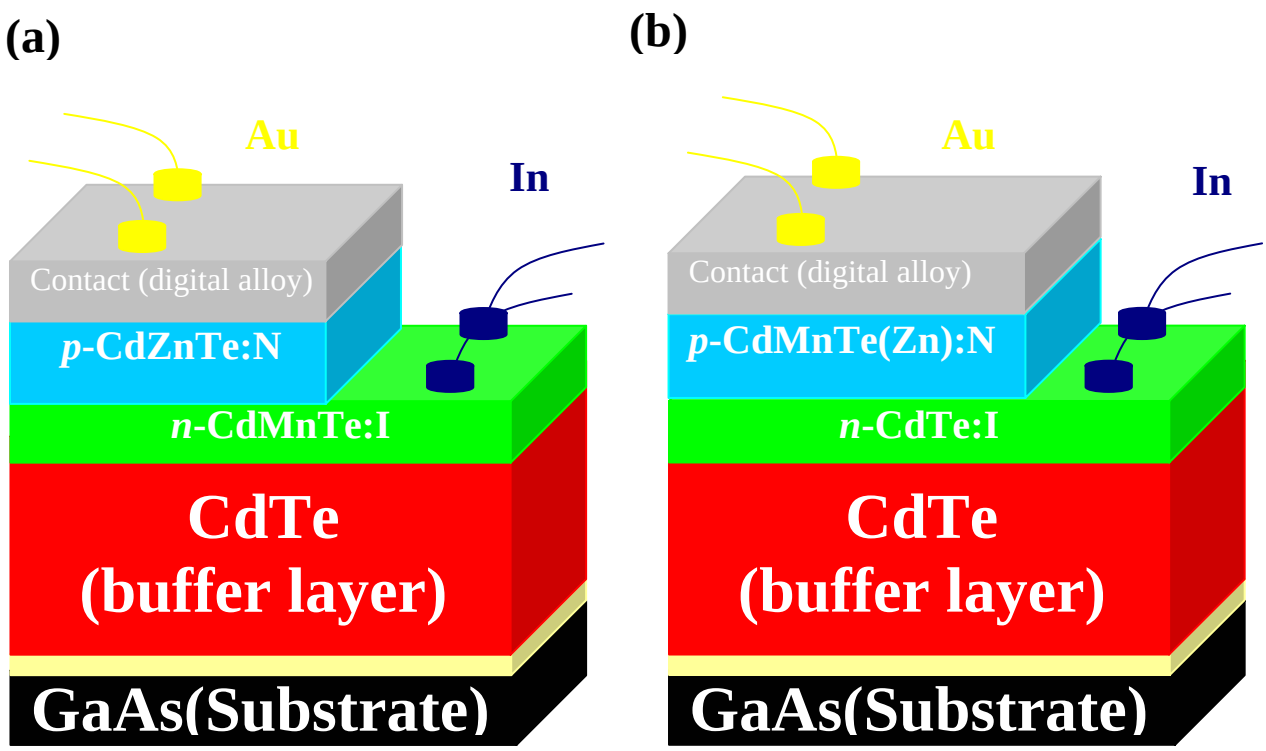

Figure 3.1 The schematic layer structure of the magnetic *p-n* junction with the magnetic *n*-type and nonmagnetic *p*-type regions (a) and with the nonmagnetic *n*-type and magnetic *p*-type regions (b).

3.2.2 Details of the MBE growth procedure

All diode structures have been grown on (100) oriented GaAs crystals. We used both n^+ silicon doped and semi-insulating undoped GaAs substrates. In order to minimize a number of defects in the junction area 4.2 μm thick undoped buffer layer of CdTe was grown. Afterwards a CdTe or $Cd_{1-x}Mn_xTe$ layer doped by iodine was deposited to create the *n*-type region of the *p-n* junction. The *p*-type region was formed by nitrogen plasma deposition into $Cd_{0.91-x}Zn_{0.09}Mn_xTe$ or $Cd_{0.91}Zn_{0.09}Te$ layers. The introduction of 9% of Zn into the *p*-type region significantly increases the effectiveness of the *p*-type doping in CdTe-related semiconductors [9]. The thickness of each doped layer was 2.1 μm. The substrate was kept at 250^0C during the whole growth process. Both kinds of diodes shown in Fig. 3.1 were grown with various Mn contents, namely, x = 1%, 5%, 10%, and 15%, respectively. The *p*-type layers were doped by nitrogen from the radio frequency (RF) plasma source using ultra-pure N_2 gas, whereas ZnI_2 (5N) was used as a solid source of iodine donors for the *n*-type doping. Temperature of ZnI_2 cell was kept in the range from 160^0C to 190^0C to get diodes with

different electron concentration from 1.5×10^{17} cm^{-3} to 3×10^{18} cm^{-3} in the *n*-type region. For the *p*-type doping, the acceptor concentration was controlled by the power of the RF radiation, which changes in the range from 150 W to 450 W. This corresponds to the hole concentration changing in the range 1.6×10^{17} cm^{-3}-8×10^{18} cm^{-3}. The carrier concentration was evaluated from the Hall measurements carried out on the reference sample grown using identical conditions.

For magneto-optical measurements *p*-*n* junctions with magnetic or nonmagnetic QW have been used. In this case, 100 Å thick quantum well consisted of $Cd_{0.99}Mn_{0.01}Te$ or CdTe and embedded between $Cd_{0.80}Mg_{0.20}Te$ barriers have been fabricated on 2.1 μm thick I-doped CdTe epilayer. The thickness of barriers was 500 Å. The width of the quantum well was chosen to be 100 Å to ensure separation between light and heavy hole levels.

The *p*-*i*-*n* diode structures consist of 0.72 μm thick I-doped CdTe which plays as the *n*-type region and 0.72 μm thick N-doped $Cd_{0.91}Zn_{0.09}Te$ which is the *p*-type region. The *p*- and *n*-type regions were separated by an intrinsic $Cd_{1-x}Mn_xTe$ layer. The width of the intrinsic layer was varied in these samples in the range from 200 Å to 800 Å. Other growth parameters such as substrate temperature, temperature of the ZnI_2 source, and the RF power were kept constant and equal 250^0C, 175^0C (n_e = 7×10^{17} cm^{-3}), and 250 W (n_h = 8.7×10^{17} cm^{-3}), respectively. The Mn content was 5% and 15%. Similar to the case of magnetic diodes 4.2 μm thick undoped buffer layer of CdTe has been grown directly on the top of the (100) oriented semi-insulating GaAs substrate.

3.2.3 Formation of Ohmic contacts

The Ohmic contact is defined as a contact between a metal and semiconductor, which will not add a significant parasitic impedance to the structure on which it is used, and it will not sufficiently change the equilibrium carrier densities within the semiconductor to affect the device characteristics. The Ohmic contact has a linear and symmetrical current-voltage characteristic [10]. Such behavior of the *I*-*V* curve is explained by the absence of the potential barrier between metal and semiconductor (from here is symmetry) and occurred an infinitely large surface recombination velocity (hence linearity).

In order to enable any electrical measurements on the *p*-*n* diode structures the Ohmic contacts to the *n*- and *p*-type regions of the diode has to be made. However, if the contacts to the *n*-type region can be directly fabricated by soldering indium to *n*-type CdTe or CdMnTe

epilayers, there are some difficulties to form an Ohmic contact to the *p*-type CdTe-based region. In the present work, in analogy to Ref. [11], in which good quality Ohmic contacts to *p*-type ZnTe were fabricated we proposed two methods of formation of Ohmic contacts to the *p*-type region of CdTe-based magnetic diodes.

The first method is based on the formation of CdZnTe epilayers with an increasing Zn content up to formation of pure ZnTe [12]. This contact layer with continually varying Zn concentration was heavily *p*-type doped. The Zn concentration gradient was achieved by lowering temperature of the Cd cell and increasing temperature of the Zn cell in the MBE process.

The second method for fabrication of low-resistance Ohmic contacts to *p*-type CdZnTe is very similar to the previous one. However, instead of varying Zn content, we employed the "digital alloy" method [13]. The main idea of this method is in fabrication of a multilayer structure consisting of 20 layers (each of them is 20 Å thick). The first layer just next to the *p*-type CdZnTe region of the *p*-*n* junction contains 19 Å thick CdZnTe and 1 Å thick ZnTe. The next layer consists of 18 Å thick CdZnTe and 2 Å thick *p*-ZnTe. This procedure is being repeated until 20 Å thick pure ZnTe is not formed on the top of the structure. One should notice that during the growth the N-plasma cell should be opened. Thus, on the most-top of heavily N-doped ZnTe layer an Ohmic contact can be formed by magnetron sputtering of a gold-palladium alloy (85% gold and 15% palladium).

Graded transitions in composition, either continuous or discrete, across an interface between two different materials, help to redistribute thermal stresses, thereby limiting the stresses at critical locations and, thus, suppressing the onset of permanent (plastic) deformation, damage, or cracking. Graded transitions can also reduce stress concentrations at the intersection between an interface and a free surface [14, 15].

Finally, as mentioned above, a good quality Ohmic contact to *n*-type CdTe or CdMnTe can be directly fabricated by soldering indium to this region. However, in the present case this region is buried below the *p*-type region. Thus, a part of the *p*-type region, as shown in Fig. 3.1, should be removed by etching in the methanol solution with 0.5% bromine (Br_2-CH_3OH) during 25 seconds. To protect the other part of the *p*-type region the vacuum grease "Apiezon N" was used as a mask. After etching, this mask was removed by rinsing in the C_2HCl_3 solution. Afterward an Ohmic contact to the *n*-type CdTe or CdMnTe epilayer is directly formed by annealing indium dots at 170^0C for about 20-30 s. It is necessary to note that if n^+ GaAs wafer is used as a substrate, the contacts can be directly fabricated to this wafer.

To determine the resistance of contacts the three-contact method, which allows unambiguously define the quality of the Ohmic contact has been used [16]. From such measurements, we found that the resistance of contacts formed to *p*-type CdZnTe by the gradient method were in the range of 250-290 Ω, whereas it changes in the range of 13-18 Ω for the "digital alloy" method. One should notice that the resistance of contacts formed to the *n*-type material is much less and changes in the range 0.05-0.1 Ω.

Figure 3.2 shows current-voltage characteristics of Ohmic contacts fabricated to *n*-type CdTe (a) and to *p*-type CdZnTe by the "graded layer" (b) and "digital alloy" (c) methods. These measurements were performed between pairs of coplanar contact pads for both *n*- and *p*- type regions of the diode as shown in Fig. 3.1. As seen in Fig. 3.2 the current changes linearly as a function of the bias applied to this structure and this clearly indicates the Ohmic characteristic of all contacts prepared.

3.3 Electrical characterization of magnetic diodes

The electrical parameters of magnetic *p*-*n* and *p*-*i*-*n* junctions were determined from capacitance-voltage (*C*-*V*) and current-voltage (*I*-*V*) measurements. These measurements were performed with (up to 9 T) and without magnetic field applied at different temperatures varying in the range from 1.6 K to 300 K.

Figure 3.3 (a) shows typical plots of current versus voltage obtained for the magnetic *p*-*n* junction with magnetic *p*-type ($Cd_{0.86}Zn_{0.09}Mn_{0.05}Te$) and nonmagnetic *n*-type (CdTe) regions. The *I*-*V* characteristics for the diode with magnetic *n*-type ($Cd_{0.95}Mn_{0.05}Te$) and nonmagnetic *p*-type ($Cd_{0.91}Zn_{0.09}Te$) regions are shown in Fig. 3.3 (b). The measurements were performed in the absence of magnetic field and in the range from 50 K to 300 K.

All these curves are characterized by the sharp turn-on of the current at about 1 V and the high reverse leakage current at room temperature. In addition, the shape of the *I*-*V* characteristics does not depend on Mn content and type of the substrate. However, the *I*-*V* curves for positive values of the bias can be divided into three distinct regions. Region 1 (from 0 V to 0.35 V) is nonlinear due to the non-exponential behavior of the diode at low voltages. Region 2 (from 0.35 V to 0.8 V) is linear, while in region 3 (from 0.8 V to 1 V) the diode current is governed by a series resistance. The series resistance is known to influence on current flowing through the diode mostly at high voltages where the plot becomes relatively flat (Fig. 3.3 (a)) [17].

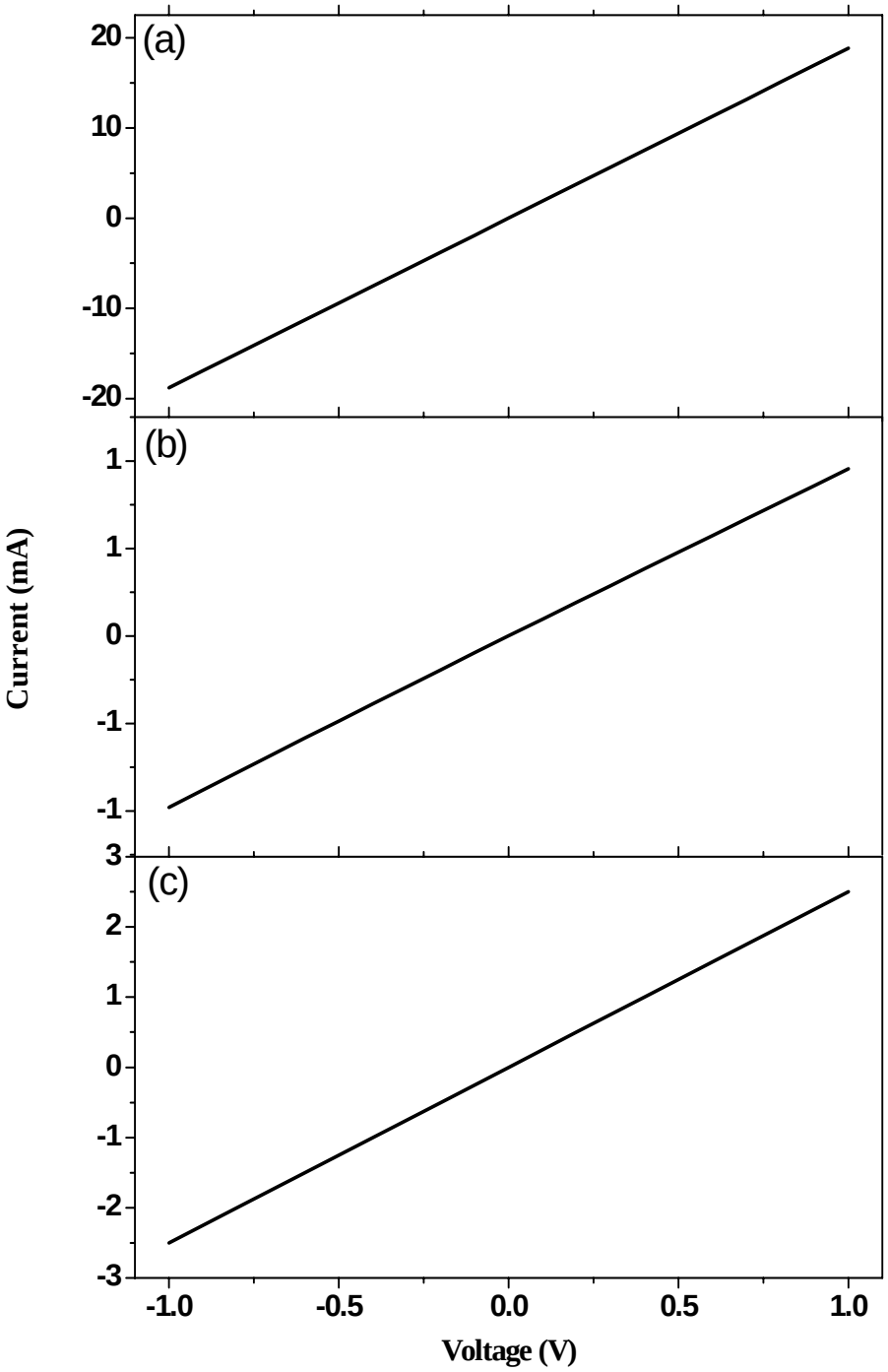

Figure 3.2 Current-Voltage characteristics of Ohmic contacts fabricated to *n*-type CdTe (a) and to *p*-type CdZnTe by the "graded layer" (b) and "digital alloy" (c) methods. The measurements were performed at room temperature.

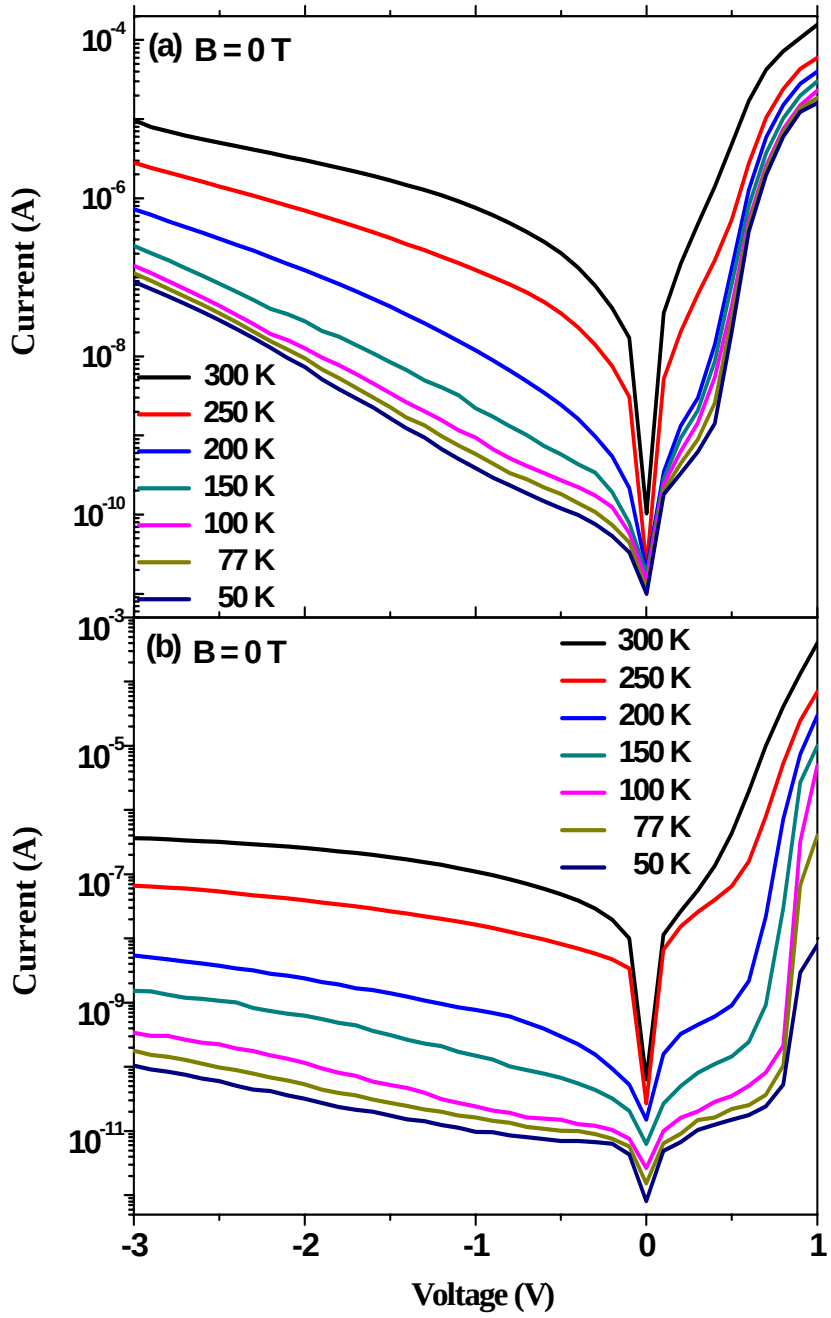

Figure 3.3 Logarithmic plots of Current-Voltage (*I-V*) characteristics of the magnetic *p-n* junction with magnetic *p*-type and nonmagnetic *n*-type regions (a). *I-V* characteristics of the magnetic diode with magnetic *n*-type and nonmagnetic *p*-type regions are shown in (b).

The series resistance may be attributed to metal-semiconductor Ohmic contact resistance, bonding-wire resistance and/or bulk resistance of *n*- and *p*-type materials especially in a case of II-VI semiconductors, which belong to high resistance materials, particularly at low temperatures. Due to series resistance, it is very difficult to determine accurately the diode parameters, because it could significantly affect all of them by introducing big errors to their real values [18]. Thus, in order to determine the diode parameters more accurately *I-V* characteristics measured at low voltages and high temperature should be used.

Using eq. (1.22) (see chapter 1) the value of the ideality factor – *n* was calculated in the region 1 (small forward bias and low current levels) at room temperature. It was found 1.86 for the structure with magnetic *p*-type and nonmagnetic *n*-type regions and 1.79 for the structure with nonmagnetic *p*-type and magnetic *n*-type regions. From this one can conclude that the recombination current dominates in both types of the magnetic *p-n* junctions [10]. At the same time, the ideality factor extracted from the region 2 in Fig. 3.3 is lower comparing with that evaluated from the region 1. These values were evaluated to be 1.23 for the diode with magnetic *p*-type region and 1.04 for the diode with magnetic *n*-type region. This clearly shows that the diffusion current dominates in this region [10]. However, as clearly follows from the obtained results the ideality factor is above unit in both cases and, moreover, it can be varied in different regions of the *I-V* characteristics. This is believed to be associated with two prominent effects.

The first one is related to the series resistance [10]. For both low and medium current levels (regions 1 and 2), $I \times R_S$ drop across the neutral region is usually small comparing with *kT/q*, where *I* is the forward current and R_S is the series resistance. This $I \times R_S$ drop reduces the bias across the depletion region and, therefore, current becomes:

$$I = I_0 \exp\left(\frac{q(V - IR_S)}{kT}\right) = I_0 \exp\left(\frac{qV}{kT}\right) / \exp\left(\frac{qIR_S}{kT}\right), \qquad (3.1)$$

As seen from this equation the ideal diffusion current is reduced by a factor of $\exp\left(\frac{qIR_S}{kT}\right)$.

From *I-V* characteristics measured at 50 K (Fig. 3.3) the series resistance of the magnetic *p-n* junction with magnetic *p*-type and nonmagnetic *n*-type regions was found to be about $25\,M\Omega$ ($6.7\,K\Omega$ at room temperature). This magnitude slightly changes in a case of the magnetic diode with magnetic *n*-type and nonmagnetic *p*-type regions. It was found about

$34\,M\Omega$ ($2.6\,K\Omega$ at room temperature) in this case. One should notice that the series resistance increases, when temperature decreases. Thus, high series resistance leads to a drastic decrease of current flowing through the *p*-*n* junction. This results in that the magneto-transport measurements become impossible to be performed at temperature lower than 50 K.

The second effect which could influence the ideality factor is linked with the high electron injection phenomena. At high currents (region 3), the injected minority carrier density (for example, holes in *n*-type region p_n) is comparable to the majority concentration (electrons in *n*-type region n_n), i. e. $p_n = n_n$. This is the high injection condition. Using equations, which describe generation-recombination processes in the depletion region of the diode [10] and an expression for the carrier density at the boundary of the depletion region [10], the following formula can be obtained:

$$p_n = n_i \exp(\frac{qV}{2kT}), \qquad (3.2)$$

where n_i is intrinsic carrier density, T is the absolute temperature, k_B is Boltzmann's constant, q is magnitude of electronic charge, V is applied bias.

Using this as a boundary condition, current becomes proportional to $exp\ (\frac{qV}{2kT})$. Therefore, in this case current increases at the slower rate comparing with that at low and medium current densities.

Figure 3.4 shows the temperature dependence of ideality factors obtained from the forward *I*-*V* characteristics at low voltages (region 1). As seen in this figure the ideality factor is close to 2 in the range of 250-300 K. However, it increases when temperature decreases for both diode configurations presented. We believe that this can be a result of the following recombination effects. The first one is related to the presence of deep level defects in the depletion layer of the diode [19]. Indeed, it is impossible to avoid imperfections in the crystal lattice even using the MBE system for the growth of such structures. The second effect is linked with the surface recombination at the depleted surface and/or the interfacial recombination through interface states at the junction [20, 21]. In addition, the ideality factor can be also increased by the presence of a thin insulating layer or a shallow doped layer of opposite conductivity type in semiconductor [22]. Similar effect can be expected due to the higher series resistance observed at the lower temperature.

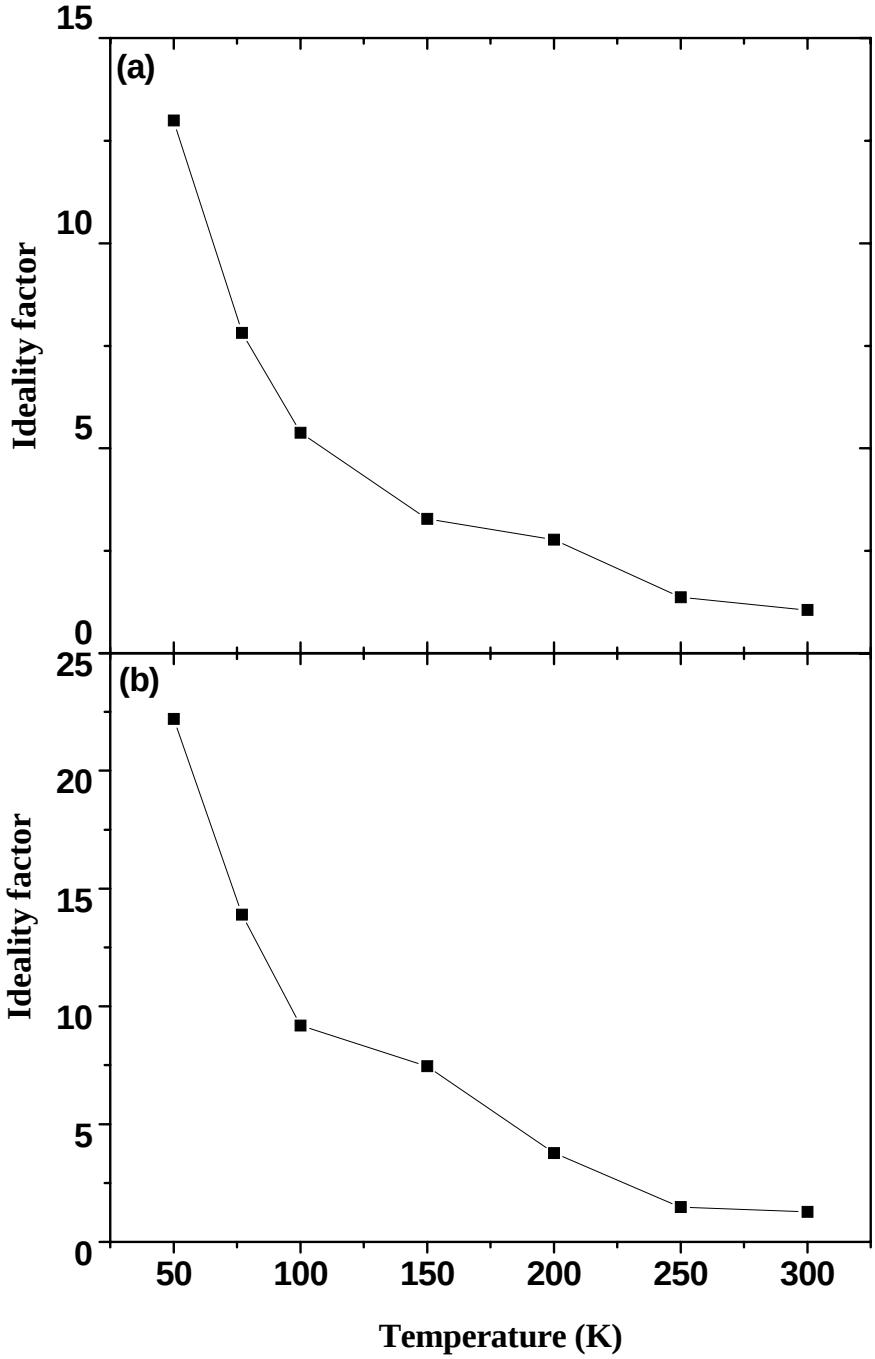

Figure 3.4 Temperature dependence of ideality factors obtained from the *I*-*V* characteristics for the small voltages in two cases: (a) the magnetic *p*-*n* junction with magnetic *p*-type and nonmagnetic *n*-type regions and (b) the magnetic *p*-*n* junction with magnetic *n*-type and nonmagnetic *p*-type regions. All measurements were performed in the absence of magnetic field.

Finally, another characteristic feature of magnetic diodes can be extracted from the *I-V* characteristics shown in Fig. 3.3. As seen in this figure an obvious plateau is observed at around 0.2 V-0.6 V. This plateau becomes more prominent with decreasing temperature. However, it is destroying when the higher bias is applied. This phenomena can be attributed to inhomogeneities of the potential barrier height which give rise to a large current and, thereby, making the series resistance to be effective even at moderate voltages [23, 24].

3.4 Capacitance-voltage characteristics of magnetic diodes

Figure 3.5 (a) shows plots of the capacitance versus voltage applied to the magnetic *p-n* junction with magnetic *p*-type ($Cd_{0.86}Zn_{0.09}Mn_{0.05}Te$) and nonmagnetic *n*-type (CdTe) regions. The *C-V* characteristics for the diode with magnetic *n*-type ($Cd_{0.95}Mn_{0.05}Te$) and nonmagnetic *p*-type ($Cd_{0.91}Zn_{0.09}Te$) regions are shown in Fig. 3.5 (b). The measurements were carried out in the absence of magnetic field in the temperature range from 50 K to 300 K.

The main feature of the *C-V* characteristics is an increase of the capacitance with decreasing the reverse bias applied to the diode. As shown in chapter 1 when the reverse bias *V* is applied to the diode the depletion layer extends to a depth *x* below the surface. According to equations (1.23) and (1.24), if *V* is increased by a small amount ΔV the depletion layer extends further to the bulk by Δx, and, thus, decreasing the capacitance by ΔC. When the junction is forward biased, there is an additional significant contribution to junction capacitance from the rearrangement of the stored charges in the neutral regions. This is called the diffusion capacitance which increases with a direct current level. This is also observed in Fig. 3.5. The parameters of the diode, such as the depletion layer capacitance and built-in potential (V_{bi}) can be determined from a plot of $1/C^2$ (in a case of uniform material) or $1/C^3$ (in a case of non-uniform material) versus the applied bias. The magnitude of the diffusion potential (built-in potential), which is used for determination of the barrier height of the magnetic *p-n* junction (see equations (1.19) and (1.19a)) was evaluated in the following way. Plotting $1/C^2$ or $1/C^3$ as a function of the applied bias and extrapolating the straight line to the crossing point with the abscissa axis one can directly obtain the diffusion potential. It is necessary to note that a large current can flow across the junction, which is forward biased. This corresponds to a large number of mobile carriers which are presented within the neutral region. The incremental change of these mobile carriers with respect to the bias contributes an additional term (the diffusion capacitance). That is why the parameters used for characterization of the *p-n* junction are usually extracted from the reverse *C-V* characteristic.

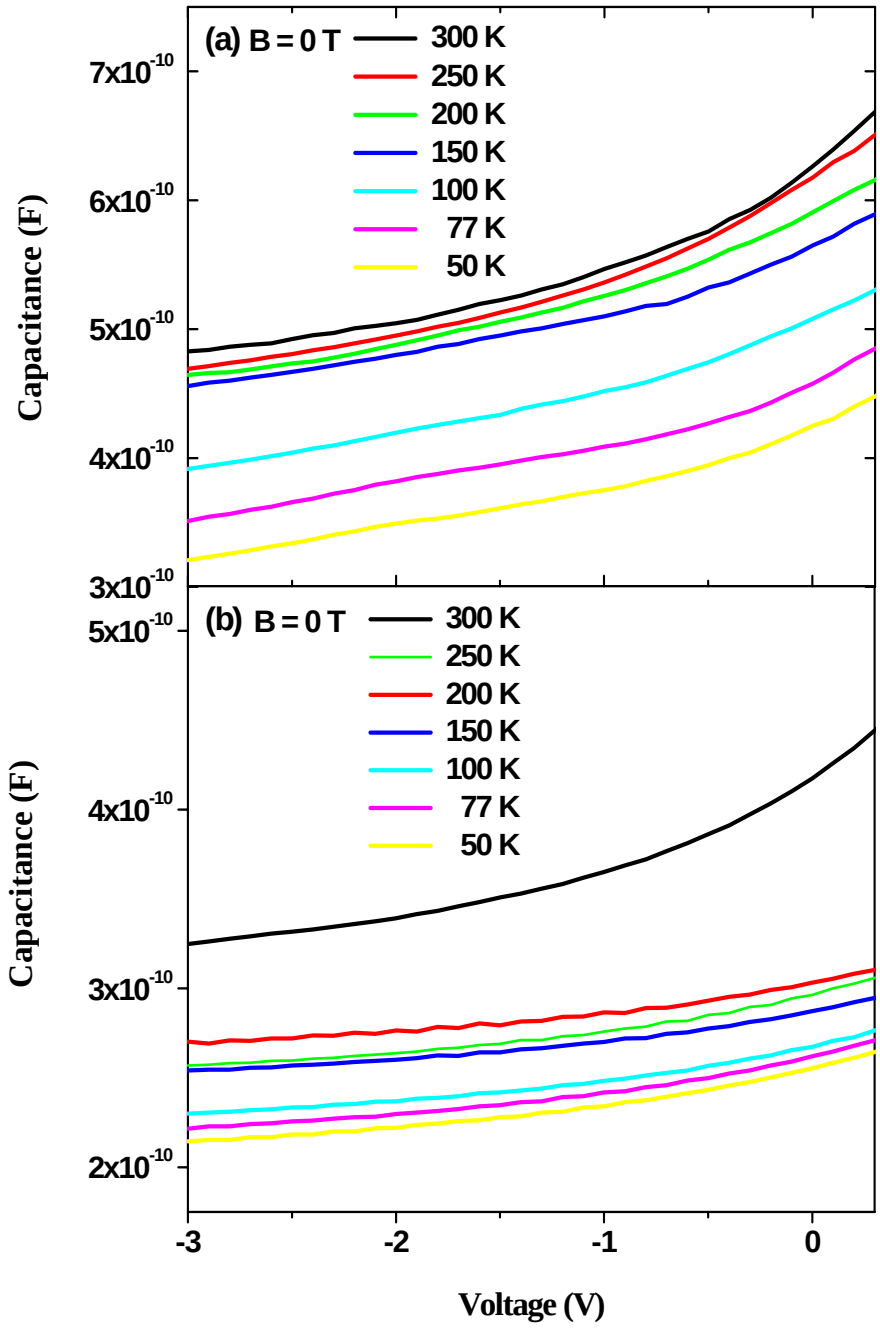

Figure 3.5 Capacitance-Voltage characteristics of the magnetic *p*-*n* junction with magnetic *p*-type and nonmagnetic *n*-type regions (a). Similar characteristics of the magnetic diode with magnetic *n*-type and nonmagnetic *p*-type regions are shown in (b). All measurements were performed in the absence of magnetic field.

Figure 3.6 shows plots of $1/C^2$ and $1/C^3$ versus the reverse bias applied to the magnetic *p*-*n* junction with magnetic *p*-type and nonmagnetic *n*-type regions (a, b) and magnetic *n*-type and nonmagnetic *p*-type regions (c, d). The straight line in this figure is the extrapolation of the linear region to the crossing point with the abscissa axis.

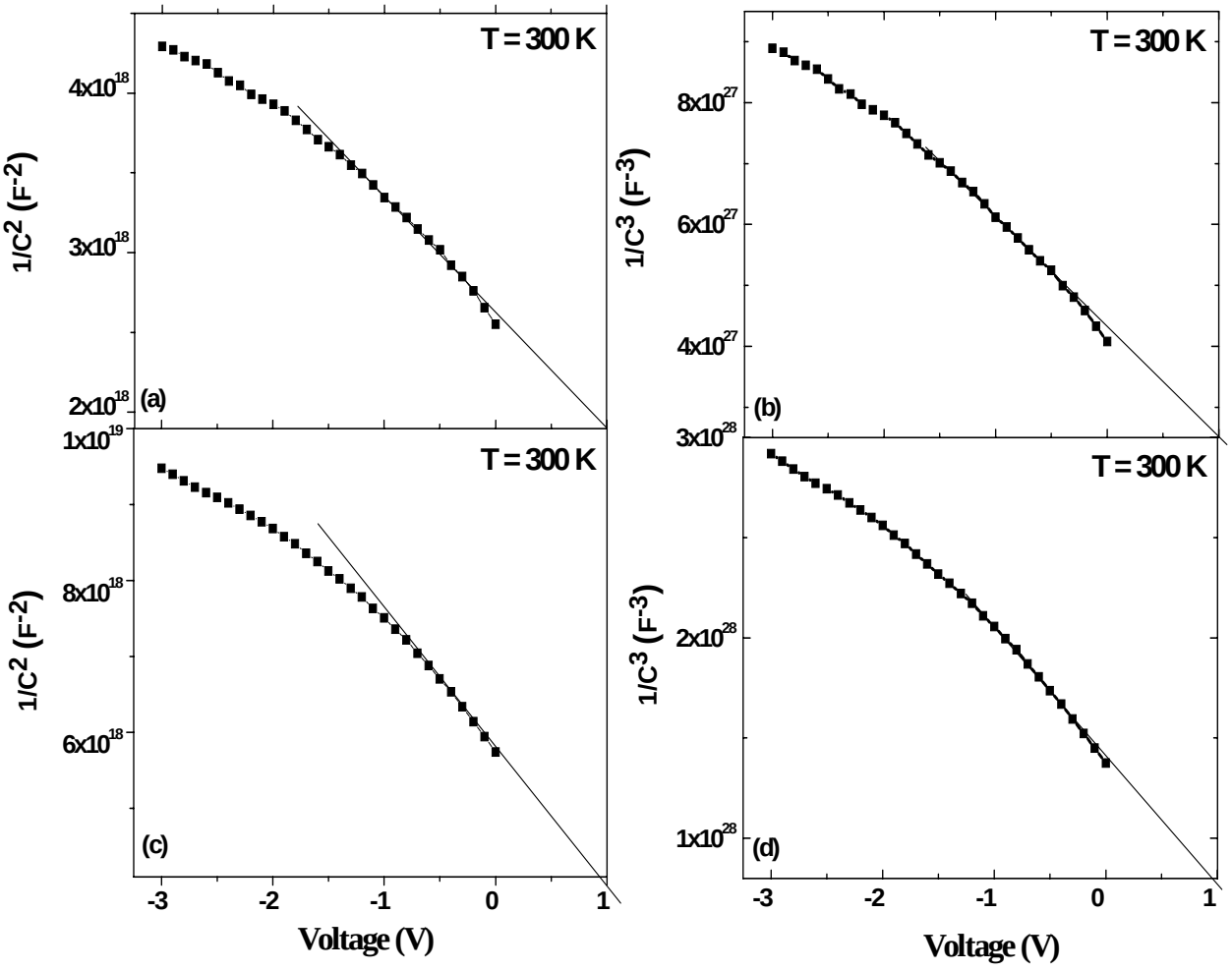

Figure 3.6 Plots of $1/C^2$ and $1/C^3$ as a function of the bias applied to the magnetic *p*-*n* junction with magnetic *p*-type and nonmagnetic *n*-type regions (a) and (b). Similar plots for the magnetic diode with magnetic *n*-type and nonmagnetic *p*-type regions are shown in Figs. (c) and (d). The straight line in this figure is the extrapolation of the linear region of these curves to the crossing point with the abscissa axis. All measurements were performed in the absence of magnetic field.

As seen in Fig. 3.6 both $1/C^2$ and $1/C^3$ do not depend linearly on the applied bias. This can be related to the following effects. First of all, the presence of the lightly doped region at

the heterointerface of the magnetic *p-n* junction can significantly distort the linear dependence, which is expected to be observed for an ideal semiconductor diode. Also such distortion can be caused by an impurity distribution between abrupt and linear gradient at the junction, which is often observed in the samples grown by the MBE technique. On the other hand, such nonlinearity might also indicate the presence of the excess capacitance in the active region. Indeed, due to the etching of the samples in Br_2-CH_3OH solution the cadmium deficiency can be observed. This could lead to the interface states, which introduce the excess capacitance and correspondingly, non-linearity observed in Fig. 3.6. Similar effect was observed, for example, in Ref. [25].

Figure 3.7 shows zero bias potential barrier height calculated from the forward *I-V* and reverse *C-V* characteristics, which are plotted as a function of temperature. The magnetic *p-n* junction has magnetic *p*-type ($Cd_{0.86}Zn_{0.09}Mn_{0.05}Te$) and nonmagnetic *n*-type (CdTe) regions (a), whereas it consists of magnetic *n*-type ($Cd_{0.95}Mn_{0.05}Te$) and nonmagnetic *p*-type regions ($Cd_{0.91}Zn_{0.09}Te$) in (b).

As seen in Fig. 3.7 the barrier height decreases significantly when temperature decreases for both types of the *p-n* junctions. This is consistent with equations (1.19) and (1.19a), which describe the built-in potential in an ideal diode. Another important thing, which should be paid attention on is that different values of the potential barrier height were determined from the *I-V* and *C-V* measurements. However, this discrepancy can be explained by existence of an additional capacitance at a metal/semiconductor contact due to an interfacial dielectric layer and/or deep trap states in this semiconductor. Another possible explanation is linked with inhomogeneities of the potential barrier height. The current in the *I-V* measurements is dominated by the one, which flows through the region of low potential barrier height (PBH). Since the low PBH patch is pinched off, the effective PBH of the patch is the potential at the saddle point. Hence, the measured *I-V* barrier height is significantly lower than the weighted arithmetic average of the PBH's. On the other hand, the barrier height evaluated from the *C-V* characteristics, is influenced by the distribution of charge at the depletion region boundary. This charge distribution follows the weighted arithmetic average of the PBH inhomogeneity; hence, in this case the barrier height is close to the weighted arithmetic average of the PBH's. This could lead to the significant difference in the values of the barrier height obtained from the *I-V* and *C-V* measurements. It should be noted that since the low PBH patches are more effectively pinched off when the semiconductor doping is low, the discrepancies between *I-V* and *C-V* measurements should be less at the lower doping levels [26]. Similar effects were observed by Sullivan *et. al.* [27].

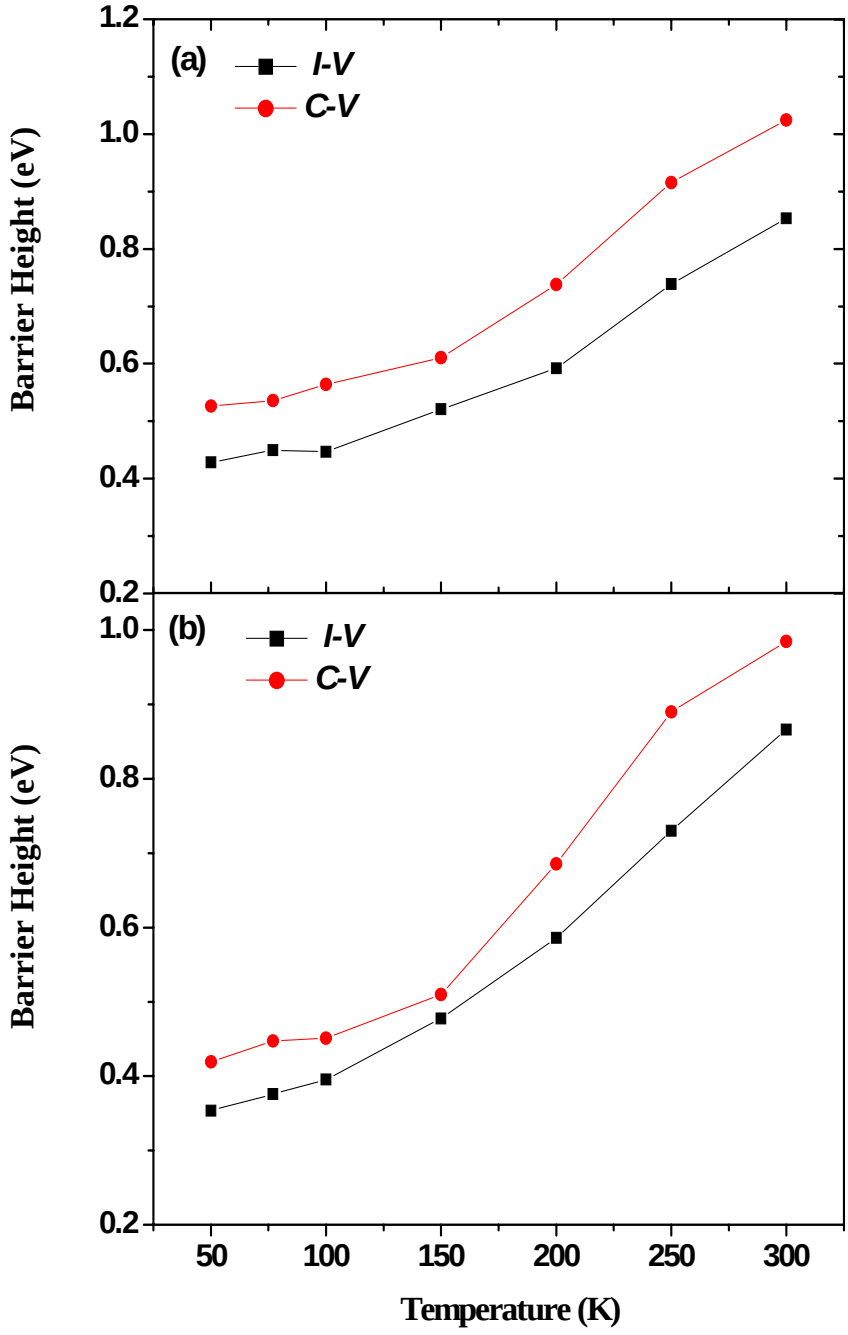

Figure 3.7 The potential barrier height as a function of temperature for the magnetic *p*-*n* junction with magnetic *p*-type and nonmagnetic *n*-type regions (a) and for the magnetic *p*-*n* junction with magnetic *n*-type and nonmagnetic *p*-type regions (b).

3.5 The *I-V* characteristics of the magnetic *p-n* junction in the presence of magnetic field

At low temperature the magnetic field causes the giant Zeeman splitting of energy bands in the DMS structure. Due to these different heights of the potential barriers for spin-down and spin-up electrons can be also observed in magnetic diodes. In the present case the barrier for spin-down electrons is smaller than that for spin-up electrons. Applying forward bias one can also significantly reduce the barrier for both spin orientations of electrons. Moreover, the forward bias allows that only spin-down electrons are able to move towards the *p*-type material and therefore, a current change in the *p-n* junction can be observed using the *I-V* measurements. However, when the applied forward bias is high enough reaching its critical value spin-up electrons become able to overcome the potential barrier and participate in the conductivity process as well. The magnitude of such critical value depends reversely on the magnetic field applied to the structure. Thus, one can expect that measuring the *I-V* characteristics at different values of the magnetic field electrons with different spin orientations participating in the conductivity process can be detected.

However, current passing through the *p-n* junction is only about 10^{-12}-10^{-11} A at about 50 K. Such low current is very close to the detection limit of the technical equipment used in the present work. As a result we are not able to measure the *I-V* characteristics below approximately 50 K. To reduce the resistance of the *p-n* junction and have possibility to perform low-temperature magneto-transport measurements we increased the doping level of both *n*- and *p*-type regions of the diode. However, according to equation (1.19) the potential barrier height also increases in this case. In the following we will show that this is very undesirable effect. Taking into account these considerations we found that a maximal doping level, which corresponds to the lowest height of the potential barrier is 7×10^{17} cm^{-3} and 8.7×10^{17} cm^{-3} for electrons and holes, correspondingly.

In this analysis we concentrate our attention on electrons because holes lose their spin orientation very quickly as a result of strong spin–orbit coupling in the valence band and due to this their practical application for the spintronics is impeded [28].

Figure 3.8 (a) shows *I-V* characteristics obtained for the magnetic *p-n* junction with magnetic *n*-type ($Cd_{0.95}Mn_{0.05}Te$) and nonmagnetic *p*-type regions ($Cd_{0.91}Zn_{0.09}Te$). *I-V* characteristics for the magnetic *p-n* junction with magnetic *p*-type ($Cd_{0.86}Zn_{0.09}Mn_{0.05}Te$) and nonmagnetic *n*-type (CdTe) regions are presented in Fig. 3.8 (b). All measurements were performed without and with (8 T) magnetic field applied at 50 K.

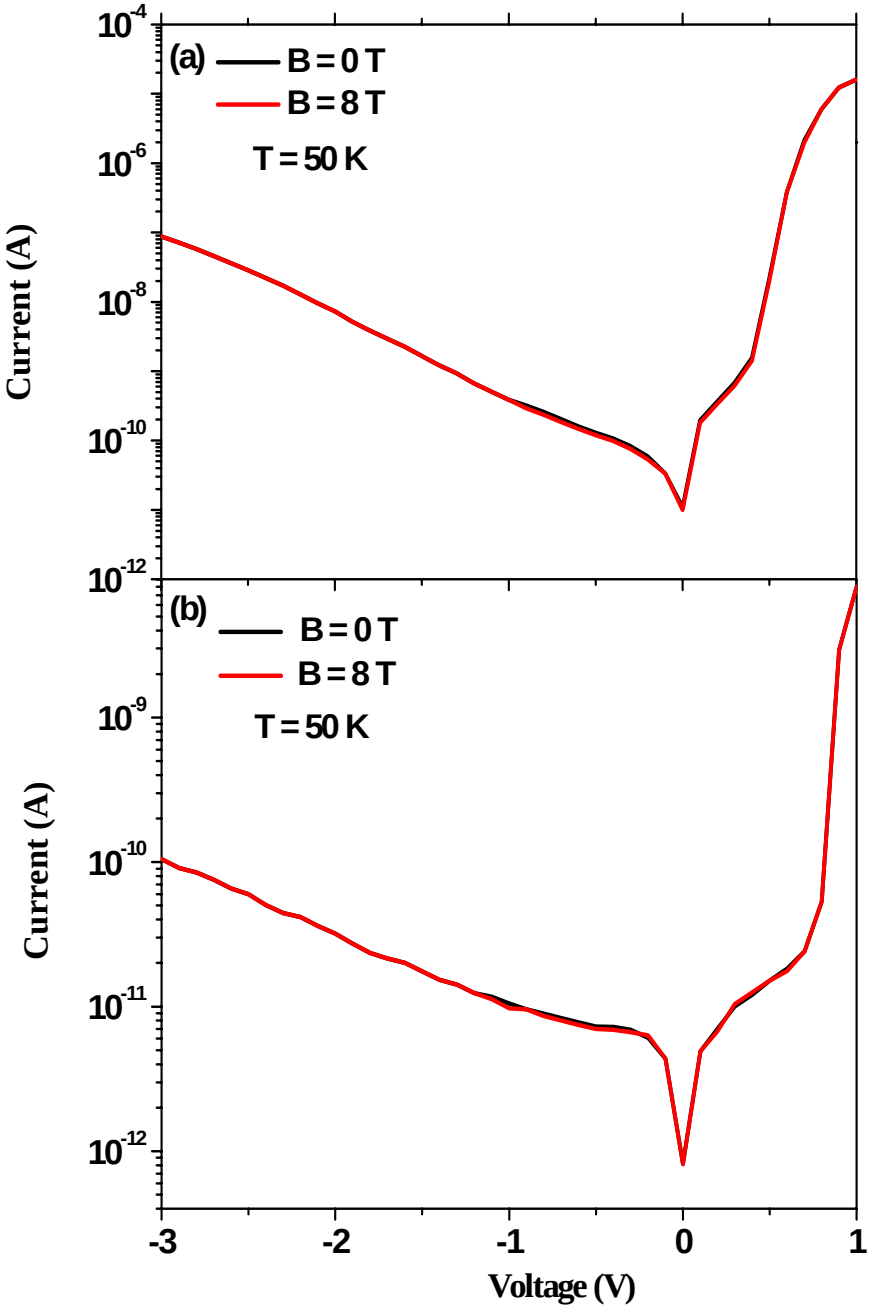

Figure 3.8 The logarithmic plots of current-voltage characteristics of the magnetic *p*-*n* junction with magnetic *n*-type and nonmagnetic *p*-type regions (a) and with magnetic *p*-type and nonmagnetic *n*-type regions (b). The measurements were performed without and with (B = 8 T) magnetic field applied at T = 50 K.

As seen in Fig. 3.8, the *I-V* characteristics do not depend on the magnetic field applied to the structures. Using Brillion function (see chapter 1, equation (1.10)), we calculated the value of the conduction band spin splitting of DMS at 50 K. The calculations were carried out for magnetic diodes with different magnetic impurity content: 1%, 5%, 10% and 15%, respectively. One should emphasize that the magnetic field of 8 T was assumed to be applied in all these calculations. The results of such calculations demonstrate that in the case of the magnetic *p-n* junction with the maximum content of the magnetic impurity (15%) the spin splitting of the conduction band was only 2.74 meV at 50 K, whereas it was found 10.4 meV at 4.2 K and 11.5 meV at 1.4 K, respectively. Then, as clearly follows from these calculations the probability to observe the magnetic effects predicted by Zutic and Fabian (see chapter 1) should be a factor of about 4-5 larger at 1-4 K than that at 50 K. Thus, the absence of influence of the magnetic field on the *I-V* characteristics of the magnetic *p-n* diode is in a good agreement with our calculations. However, due to the freeze-out effect we still cannot perform transport measurements at temperature below than 50 K even taking into account that the highest possible doping level in both *n*- and *p*-type regions of the magnetic diode has been used. Therefore, as the next step we decided to use circular polarized light which could help us to overcome the obstacle linked with the freeze-out effect.

3.6 The *I-V* characteristics of the illuminated magnetic *p-n* junction in the present of magnetic field

When *p-n* junction is illuminated by photons having energy $h\nu \geq E_g$ an added generation rate g participates in the overall current flow. The absorption of photons leads to the formation of excess electrons in the *n*-type region and excess holes in the *p*-type region of the device, generating an open circuit voltage drop V_{oc} across the *p-n* junction. The optically induced voltage splits the quasi-Fermi levels F_n and F_p by the amount $qV_{oc.}$ For an open-circuit ideal junction (I = 0), the developing voltage due to the photovoltaic effect will be given by the following equation:

$$V_{oc} = \frac{kT}{q}\ln\left(\frac{L_p + L_n}{\left(\frac{L_p p_n}{\tau_p} + \frac{L_n n_p}{\tau_n}\right)} g + 1\right), \qquad (3.3)$$

where L_p, L_n are the minority carrier diffusion length, τ_p, τ_n are the minority carrier lifetimes, and p_n, n_p are the minority carrier densities [29,30].

Based on the "quasi-equilibrium" approximation, analytical expression for *I-V* characteristics in illuminated *p-n* junction are given by the following equations:

$$I_{fwd} = I_S(\exp(\frac{qV_{fwd}}{kT}) - 1) - qA(L_n + L_p)g \tag{3.4}$$

$$I_{rev} = I_S + qA(L_n + L_p)g\,, \tag{3.5}$$

where I_{fwd} and I_{rev} are the forward and reverse net-flowing currents respectively, I_S is the saturation current in the dark, V_{fwd} is the applied forward bias, k is the Boltzmann constant, T is the junction absolute temperature, q is the electronic charge, A is the area of the device, L_p and L_n are the minority carrier diffusion lengths for holes and electrons, respectively, and g is the optically induced generation rate for holes in the valence band and electrons in the conduction band.

According to equation (3.4), in the forward biased *p-n* junction, the illumination produces a photocurrent component that reduces the net current flow (i.e., under given forward bias settings, less current flows in an illuminated device compared to the corresponding current that flows in the dark). In the reverse biased *p-n* junction equation (3.5), the produced photocurrent adds to the net current flow (i.e., the current that flows in a reverse biased illuminated device, equals the dark saturation current increased by the amount of the produced photocurrent).

However, often a discrepancy from the "quasi-equilibrium" approximation can be observed. As an example, the presence of recombination centers in the junction area could significantly distort the analysis [31]. Such centers may be distributed either in the bulk or over the surface, and usually they introduce deep electronic states into the band-gap of a semiconductor. Having levels in the band-gap they can contribute to the overall current flow across the barrier and, thus, significantly affect the forward and reverse *I-V* characteristics.

In the present work the magnetic *p-n* junction was illuminated by He-Ne laser beam with the wavelength of 632.8 nm and the input power density P = 30 mWcm^{-2}. The light from the laser was circularly polarized. The polarization of this light can be changed by direction of the magnetic field applied. Positive values of the magnetic field were established to

correspond to the right circular polarization (σ^+) whereas negative values of the magnetic field were found to correspond to the left circular polarization (σ^-). This assignment has been made using photoluminescence data of a reference sample. The reference sample was 100 Å thick single magnetic quantum well $Cd_{0.95}Mn_{0.05}Te$ embedded between $Cd_{0.70}Mg_{0.30}Te$ barriers. The intensity ratio between σ^+ polarization and σ^- polarization was 97% at T = 4.2 K. The magnetic field was 2 T in this case.

Figure 3.9 (a) shows *I-V* characteristics obtained for the magnetic *p-n* junction with magnetic *p*-type ($Cd_{0.86}Zn_{0.09}Mn_{0.05}Te$) and nonmagnetic *n*-type (CdTe) regions and recorded without and under illumination using spin-polarized light. Similar characteristics recorded for the magnetic *p-n* junction with magnetic *n*-type ($Cd_{0.95}Mn_{0.05}Te$) and nonmagnetic *p*-type ($Cd_{0.91}Zn_{0.09}Te$) regions are presented in Fig. 3.9 (b). All measurements were performed in the absence of magnetic field at T = 50 K.

As seen in Fig. 3.9 under illumination current increases about 5 orders of magnitude comparing with the value of dark current for the *p-n* junction with magnetic *p*-type region. A similar increase of the current (about 4-5 orders of magnitude) has been also observed in the diode with magnetic *n*-type region. Moreover, in a good agreement with equations (3.4) and (3.5) the reverse bias current also increases under illumination using the laser beam. On the other hand, a significant drop of the forward bias current was observed at about V_{oc} = 0.65 V in the magnetic *p-n* junction with magnetic *p*-type region, whereas a similar drop was detected at about 0.25 V in the diode with magnetic *n*-type region. A further increase of bias above V_{oc} results in a classical exponential behavior of current component observed before its saturation at about 0.8 V. This behavior is believed to be due to influence of a series resistance and/or high injection effects on the *I-V* characteristics of the magnetic diodes.

Figure 3.10 shows the *I-V* characteristics of the magnetic *p-n* junction with magnetic *p*-type ($Cd_{0.86}Zn_{0.09}Mn_{0.05}Te$) and nonmagnetic *n*-type (CdTe) regions recorded in the presence of magnetic field. Similar characteristics for the magnetic diode with magnetic *n*-type ($Cd_{0.95}Mn_{0.05}Te$) and nonmagnetic *p*-type ($Cd_{0.91}Zn_{0.09}Te$) regions are presented in Fig. 3.11. In both cases, during the measurements the diodes were kept under illumination using the right and left polarized light. For the sake of clarity, only curves measured at three different temperatures (4.2 K, 77 K and 300 K) and kept at two different values of the magnetic field (0 T and 2 T) are shown in these figures.

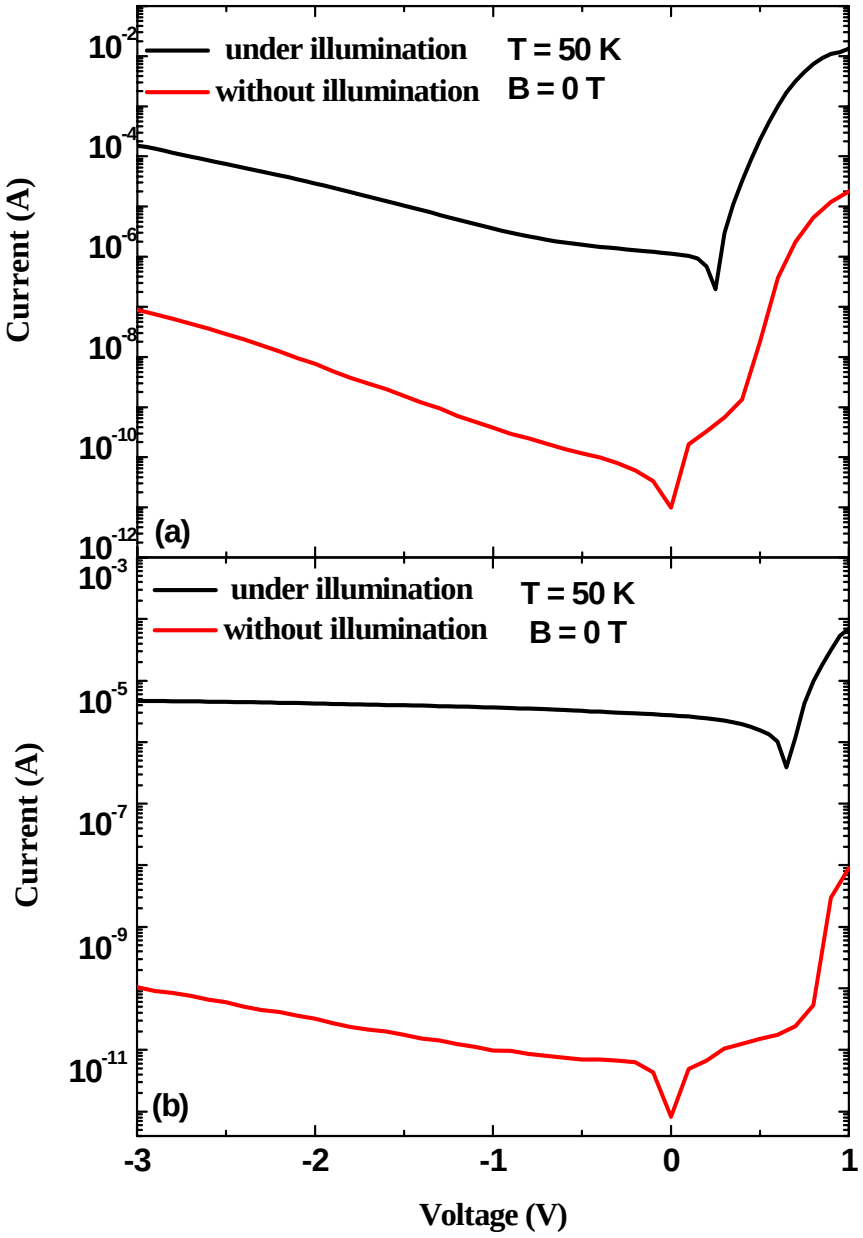

Figure 3.9 Current-Voltage characteristics of illuminated magnetic *p*-*n* junction with magnetic *n*-type and nonmagnetic *p*-type regions (a) and with magnetic *p*-type and nonmagnetic *n*-type regions (b). For comparison, similar characteristics of unilluminated magnetic *p*-*n* junctions are also presented.

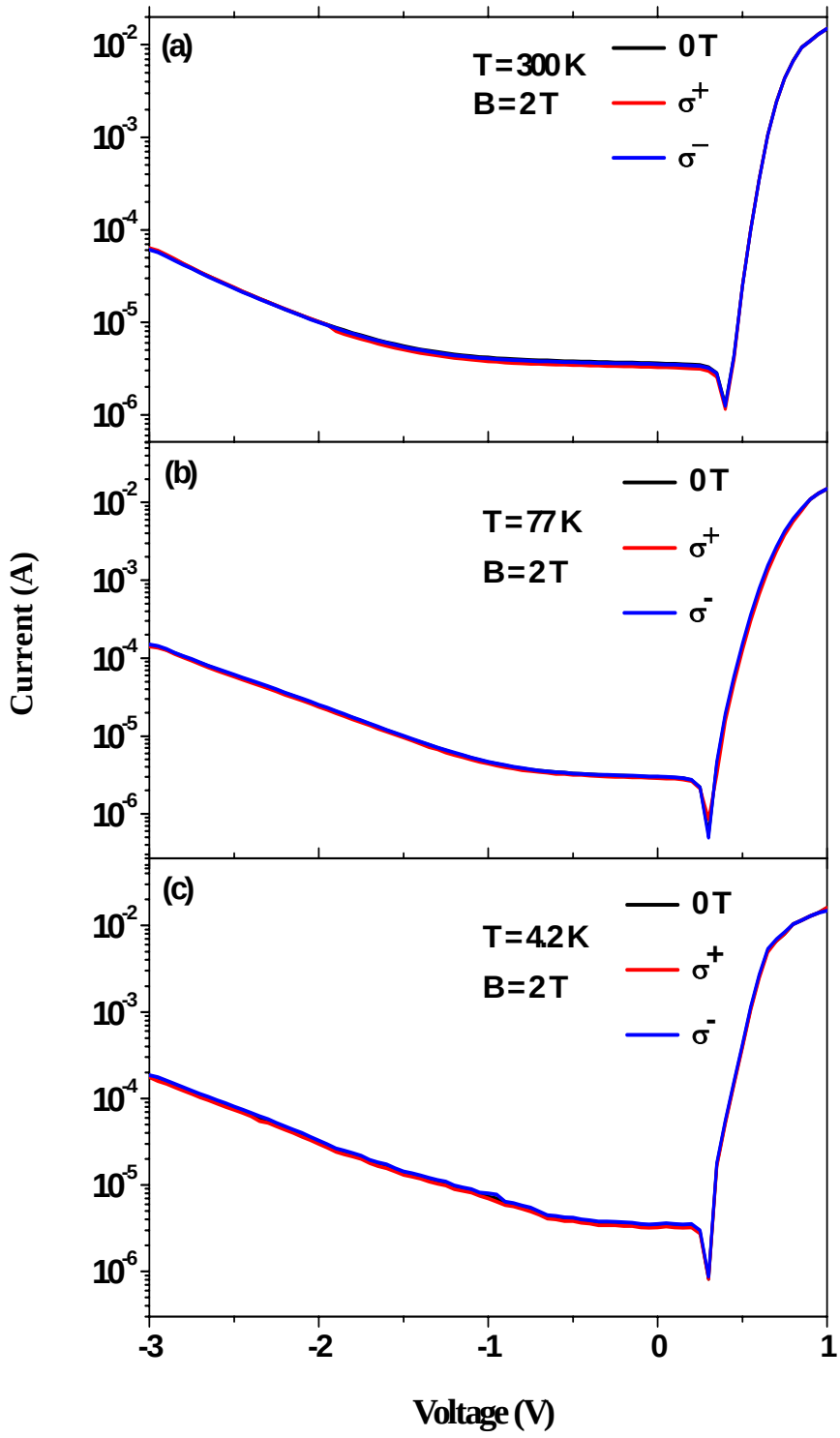

Figure 3.10. Current-Voltage characteristics of the magnetic *p-n* junction with magnetic *p*-type and nonmagnetic *n*-type regions. The measurements were performed at 4.2 K (a), 77 K (b) and 300 K (c). The magnetic field applied to the diode was B = 0 T and 2 T.

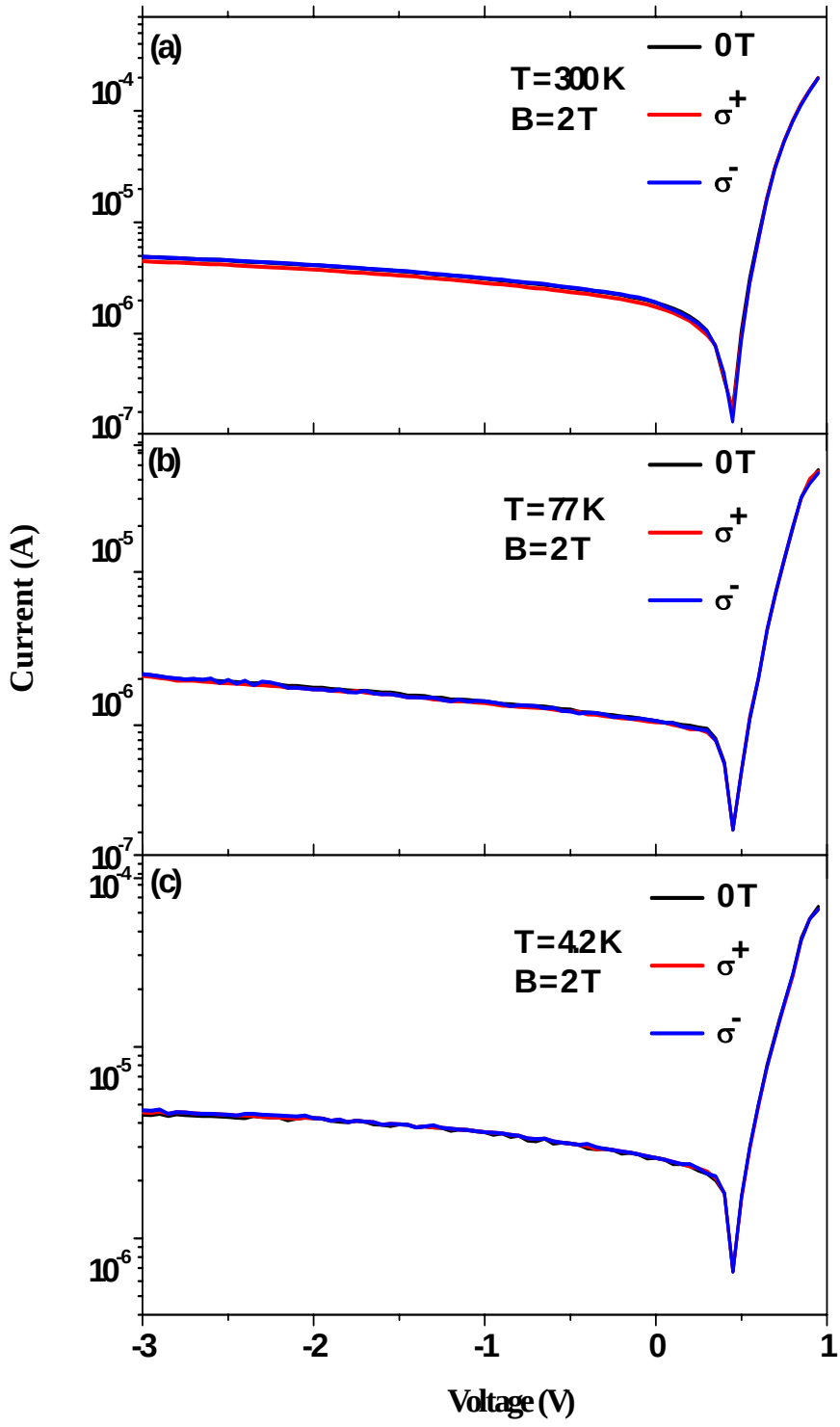

Figure 3.11. Current-Voltage characteristics of the magnetic *p-n* junction with magnetic *n*-type and nonmagnetic *p*-type regions. The measurements were performed at 4.2 K (a), 77 K (b) and 300 K (c). The magnetic field applied to the diode was B = 0 T and 2 T.

As seen in Figs. 3.10 and 3.11, no considerable changes have been observed in the *I-V* characteristics upon varying the polarization of light and magnetic field at T = 4.2 K. Similar conclusions have been also obtained for the higher values of the magnetic field not shown in these figures. Moreover, no changes in the *I-V* characteristics have been observed in the samples with different Mn content and different types of the substrate used.

Finally, in order to remove or, at least, minimize the effects linked with temperature fluctuations similar *I-V* characteristics have been recorded in the diode illuminated with a minimal light intensity of the laser beam at T = 4.2 K.

Figure 3.12 shows the *I-V* characteristics of the magnetic *p-n* junction with magnetic *p*-type and nonmagnetic *n*-type regions. The measurements were performed with (blue and red curves) and without (black curve) magnetic field applied at T = 4.2 K. The neutral density filter was used to obtain the lowest intensity of the laser light. Behind this filter the density of power was less than 1 $mWcm^{-2}$. As seen in Fig. 3.12 a minimal intensity of the circularly polarized light leads to that the open-circuit voltage shifts towards its lower values ($V_{oc} \approx 0.01$ V) comparing with those observed for the higher excitation power used. However, even in this case no changes in the *I-V* characteristics have been observed when the magnetic field was applied to the structure.

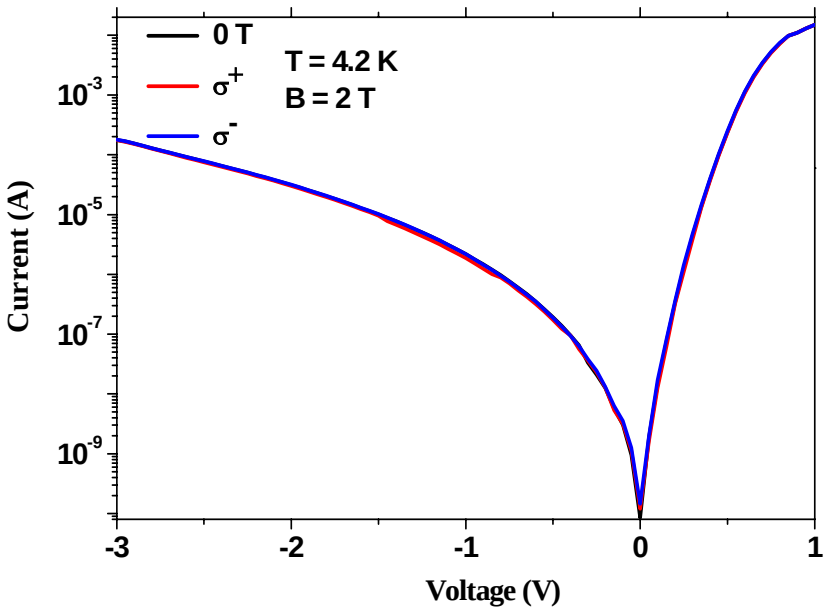

Figure 3.12 Current-Voltage characteristics of the magnetic *p-n* junction with magnetic *p*-type and nonmagnetic *n*-type regions. The measurements were performed with (blue and red curves) and without (black curve) magnetic field applied at T = 4.2 K.

To analyze the *I-V* characteristics of the magnetic *p-n* junction hold under illumination by spin-polarized light a spin polarization current parameter (*P*) can be introduced. This parameter is described by the following equation:

$$P = \frac{I_+ - I_-}{I_+ + I_-}, \tag{3.8}$$

where I_+, and I_- are currents flowing through the *p-n* junction under illumination by σ^+ and σ^- circularly polarized light, respectively.

In the present case *P* describes a contribution of electrons with definite spin orientation to the total current. Figure 3.13 shows the plot of the current spin polarization as a function of voltage applied to the magnetic *p-n* junction with magnetic *p*-type ($Cd_{0.86}Zn_{0.09}Mn_{0.05}Te$) and nonmagnetic *n*-type (CdTe) regions.

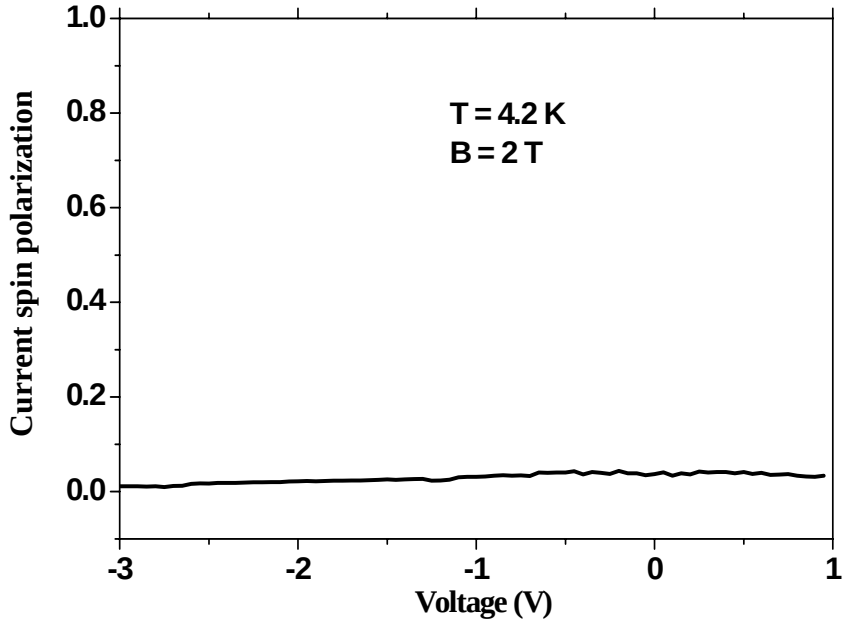

Figure 3.13 The current spin polarization as a function of bias applied to the magnetic *p-n* junction with magnetic *p*-type and nonmagnetic *n*-type regions. This curve was taken with magnetic field of B = 2 T at T = 4.2 K.

As seen in this figure the current spin polarization is close to zero and stays almost constant over the whole range of the applied bias. Similar results were also obtained in *p-n* junctions with the higher concentration of Mn and for the higher values of the magnetic

field applied. Moreover, similar conclusions were also obtained for the diode with magnetic *n*-type ($Cd_{0.95}Mn_{0.05}Te$) and nonmagnetic *p*-type ($Cd_{0.91}Zn_{0.09}Te$) regions, however, for the sake of clarity these results are not presented in Fig. 3.13. Thus, as clearly follows the current spin polarization does not change as a function of both magnetic field and Mn content in the magnetic diode.

Another interesting detail which we would like to focus on is that due to theoretical predictions by Zutic and Fabian current flowing through the magnetic diode should be observed even when bias is not applied to the structure [1-5]. Following this idea, we determine zero bias current as a function of magnetic field applied to the magnetic diode.

Figure 3.14 shows zero bias current as a function of magnetic field for the magnetic *p*-*n* junction with magnetic *n*-type ($Cd_{0.95}Mn_{0.05}Te$) and nonmagnetic *p*-type ($Cd_{0.91}Zn_{0.09}Te$) regions at 4.2 K, 77 K and 300 K. During low-temperature measurements the diode was illuminated by He-Ne circularly polarized laser beam having a minimal excitation power. As seen in Fig. 3.14 the zero bias current does not change as a function of magnetic field. This is an opposite effect to that predicted by Zutic and Fabian.

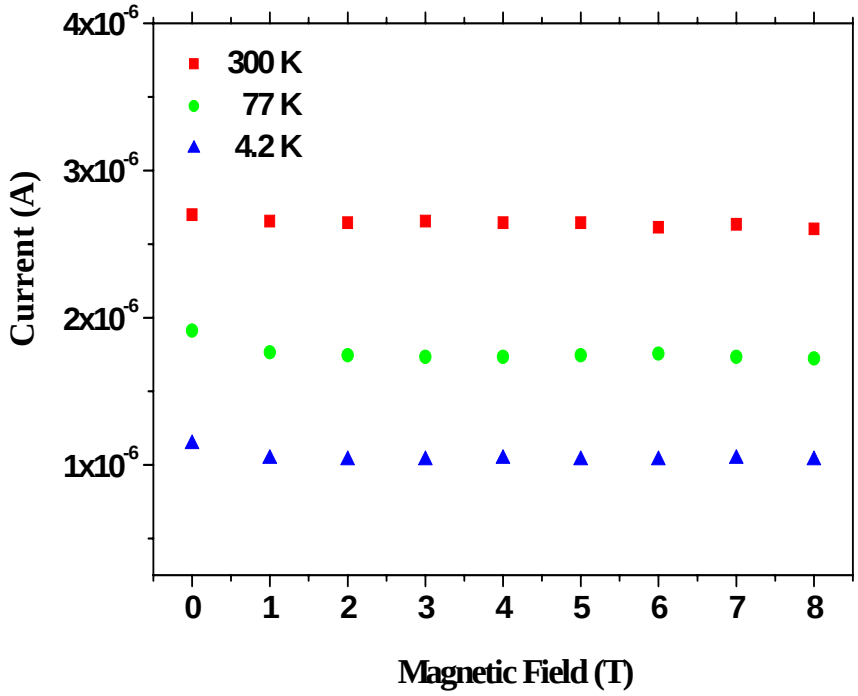

Figure 3.14. The zero bias current as a function of magnetic field for the magnetic *p*-*n* junction with magnetic *n*-type (CdMnTe) and nonmagnetic *p*-type (CdZnTe) regions taken at 4.2 K, 77 K and 300 K.

One of the main reasons of the absence of the magnetic effects predicted by Zutic and Fabian may be related to the fact that magnetically induced changes of the barrier height are quite small in comparison to the initial barrier height in the unbiased diode at 0 T. As mentioned above the barrier height for spin down electrons is smaller comparing with that for spin up electrons. However, as seen in Fig. 3.7 it can be still too high for electrons to overcome even when magnetic field is applied to the diode. Indeed, the initial barrier height was estimated to be about 0.4-0.5 eV at 50 K. On the other hand the maximal value of the excitonic Zeeman splitting in CdMnTe is only about 100 meV at 4.2 K, whereas a maximal Zeeman splitting of the conduction band is even smaller and equal about 20 meV.

Taking into account all these considerations one can expect that placing an undoped intrinsic layer between *p*- and *n*- regions the initial barrier height for electrons can be divided in two parts. It could allow electrons having the smaller energy to overcome the barrier and, thus, in an artificial way to decrease the initial barrier height. Following this idea, a number of *p*-*i*-*n* structures with different width of the intrinsic layer have been grown using the MBE technique.

3.7 *P*-*i*-*n* magnetic diodes

The *p*-*i*-*n* diodes were fabricated in a form of sandwich, in which the external segments consist of *p*- and *n*-type regions with a relatively high conductivity, whereas the middle layer was fabricated from an undoped semiconductor (*i*-intrinsic) providing a small capacity of the diode. One should notice that identical growth parameters as those for the *p*-*n* junction with the lowest barrier height have been used in this case.

In an unbiased diode resistance of the *p*-*i*-*n* junction structure is about tens $K\Omega$ at room temperature. Moreover, it becomes even larger when a reverse bias is applied. On the other hand, injection of holes from the *p*-type region and electrons from the *n*-type region to the intrinsic *i*-layer occur in the forward biased diode. This leads to a sharp decrease of the resistance of such structure. Therefore, a typical characteristic feature of the *p*-*i*-*n* diode is the higher ratio between the forward and reverse resistance comparing with a “normal” *p*-*n* diode [32].

Figure 3.15 shows *I*-*V* characteristics of the *p*-*i*-*n* structure with nonmagnetic *n*-type (CdTe) and *p*-type ($Cd_{0.91}Zn_{0.09}Te$) regions and magnetic intrinsic region ($Cd_{0.95}Mn_{0.05}Te$) recorded with and without magnetic field applied. The width of the intrinsic region is 200 Å.

All *I-V* characteristics were measured under illumination by circular polarized light having a minimal intensity at 4.2 K. For the sake clarity only two different values of magnetic field (B = 0 T and 2 T) are shown in this figure.

As seen in Fig. 3.15 no influence of the magnetic field on the *I-V* characteristics has been also observed in this case. No changes in the *I-V* characteristics were also observed if the higher magnetic field (up to 8 T) was applied to the diodes. Moreover, similar results have been obtained varying both Mn content in the intrinsic layer and the width of the intrinsic layer. Thus, according to these results it is very likely that the barrier height in such structures is still too high in order to observe the magnetic effects predicted by Zutic and Fabian.

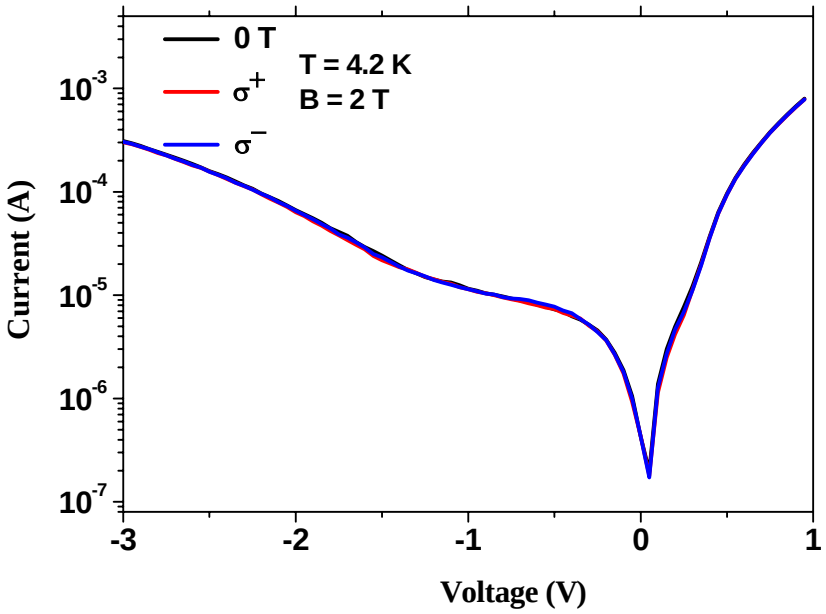

Figure 3.15 Current-Voltage characteristics of the *p-i-n* structure with nonmagnetic *n*-type (CdTe) and *p*-type ($Cd_{0.91}Zn_{0.09}Te$) regions and magnetic intrinsic region ($Cd_{0.95}Mn_{0.05}Te$), measured at two polarizations of circular polarized light having a minimal intensity at T = 4.2 K.

3.8 Light Emitting Diode structures

From magneto-optical measurements of nonmagnetic *p-n* junctions we observed that the forward-biased diode can effectively emit light, and, thus, serve as a Light Emitting Diodes (LED) [33]. Moreover, the intensity of the emitting light may be significantly increased if a quantum well (QW) is located between *n* and *p*-type terminals. Thus, in this

section, we would like to concentrate our attention on properties of the magnetic *p-n* junction, playing as effective light sources.

In the forward-biased Light Emitting Diode with a nonmagnetic or magnetic quantum well electrons and holes recombine in the vicinity of the *p-n* junction or inside the quantum well and as a result such structures can emit light. This light is unpolarized, because all carrier spin states are equally populated, and all dipole-allowed radiative transitions occur with equal probability. Similar results are observed in the diode with nonmagnetic QW even when magnetic field is applied [28]. On the other hand, in LED with DMS quantum well, in the presence of magnetic field the *sp-d* exchange interaction leads to a giant spin splitting with the *g*-factor (the effective Lande factor of an electron inside the semiconductor) of up to 100 [34]. This results in a large Zeeman splitting of band-edge-related states in the DMS material. In zinc blende semiconductor such as CdMnTe, the conduction band is twofold degenerate at the center of the Brillouin zone corresponding to spin-up and spin-down electrons ($m_j = \pm\frac{1}{2}$). The valence band is fourfold degenerate in the same material, and consists of heavy-hole and light-hole bands with large and small effective masses ($m_j = \pm\frac{3}{2};\pm\frac{1}{2}$). Moreover, in the case of DMS quantum well the heavy-hole and light-hole valence bands are separated in energy due to the quantum confinement effect. The value of this splitting is usually around 10 meV, and is much larger than k_BT (around 0.12 meV) at 1.4 K. As a result the states, which correspond to the light-hole valence band are not occupied. In this case, only states of the heavy-hole valence band participate in the radiative recombination process. The probability of a given transition is weighted by the matrix element connecting the levels involved, so that transitions to heavy-hole states are 3 times more likely than those to light-hole states. Then, the emitted light will be circularly polarized with a degree of polarization given by the following equation:

$$P_{circ} = \frac{I^+ - I^-}{I^+ + I^-} = \frac{(3n_\uparrow + n_\downarrow) - (3n_\downarrow + n_\uparrow)}{(3n_\uparrow + n_\downarrow) + (3n_\downarrow + n_\uparrow)}, \qquad (3.9)$$

where $n_\uparrow$ and $n_\downarrow$ are the occupation numbers of the spin ½ levels.

Thus, in a case of the LED structure with magnetic QW, polarization analysis of the electroluminiscence (EL) data effectively interrogates the spin polarization of the carriers involved in this process.

Figure 3.16 shows the EL spectra recorded for the LED structure with the magnetic quantum well ($Cd_{0.99}Mn_{0.01}Te$) using right (σ^+) and left (σ^-) circular polarizations for different values of the magnetic field applied at 1.4 K. The threshold current for light emission process was 140 mA, whereas the forward bias was kept 1 V during these measurements. The thickness of each nonmagnetic barrier $Cd_{0.80}Mg_{0.20}Te$ was 500 Å. The spectra are normalized and aligned to the zero-field spectrum.

As seen in Fig. 3.16 (a) no optical polarization is observed in the absence of a magnetic field. This is consistent with that $Cd_{0.99}Mn_{0.01}Te$ is a Brillouin paramagnet, which acquires a net magnetization only when a magnetic field is applied to the structure. We identify the dominant emission peak near 1.615 eV as a signal corresponding to the exciton recombination (X). It is in a good agreement with the energy of exciton (1.615 eV) in 100 Å thick $Cd_{0.99}Mn_{0.01}Te$ quantum well [34]. In support of this idea this line has not been observed in the magnetic *p*-*n* junction without QW (Fig. 3.17). However, the full width at half maximum (FWHM) observed for the X signal is relatively large (about 40 meV). Additionally, this dominant peak at 1.615 eV has a clear asymmetrical form. This can be only explained by superposition of two different peaks. The first peak is related to the exciton recombination in the magnetic quantum well (1.615 eV), whereas the second one is shifted towards the lower energy. In contrast to the X peak this second peak labeled DAP (donor-acceptor pair) has been also observed in the magnetic *p*-*n* junction without QW where it has a maximal value at 1.597 eV. However, one should notice that the intensity of the DAP peak is significantly smaller comparing with that of the X peak.

Taking into account identical growth parameters of the magnetic *p*-*n* junction and the LED structure one can conclude that the DAP peak origins from the energy transition located in nonmagnetic *p*- and/or *n*-type regions. The most plausible explanation is that this signal corresponds to the energy of the donor-acceptor pair transition in *n*-type I doped CdTe, which is 1.597 eV [35] and perfectly coincides with the position of the peak in the EL spectrum.

Using the EL data shown in Fig. 3.16 the degree of circular polarization can be calculated using equation (3.9). As seen in Fig. 3.16, the intensities of σ^+ and σ^- components become different at 2 T (Fig. 3.16 (c)). This difference reaches a maximal value at 7 T (see Fig. 3.16 (e)). Thus, circular polarization of light emitted from the quantum well region increases as a function of magnetic field.

Following this idea Fig. 3.18 shows degree of circular polarization of the EL signal in the forward-biased LED structure with magnetic quantum well ($Cd_{0.99}Mn_{0.01}Te$) embedded between $Cd_{0.80}Mg_{0.20}Te$ barriers as a function of magnetic field applied at 1.4 K.

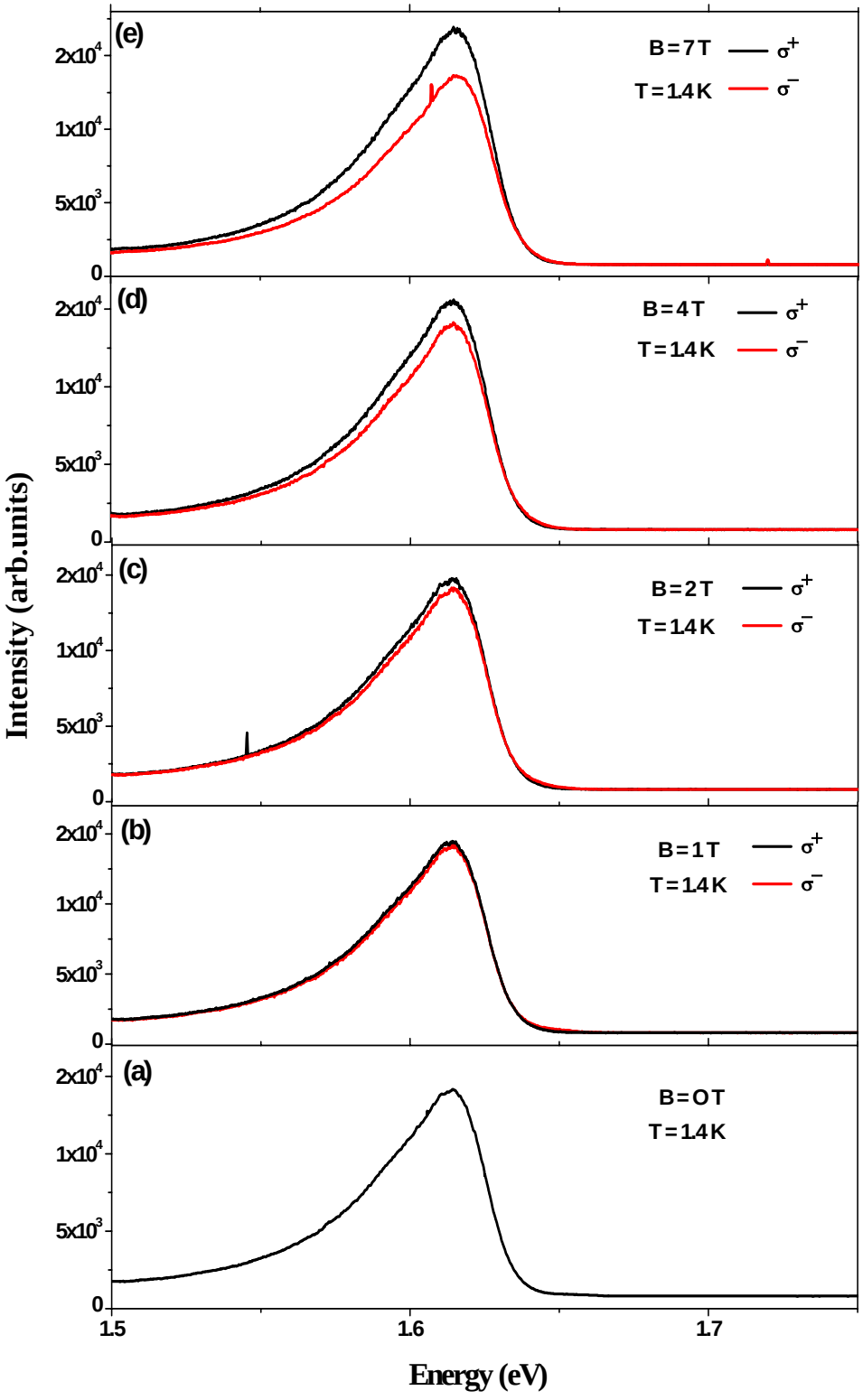

Figure 3.16 Electroluminescence spectra recorded for the LED structure using right (σ^+) and left (σ^-) circular polarization for different values of magnetic field applied at 1.4 K.

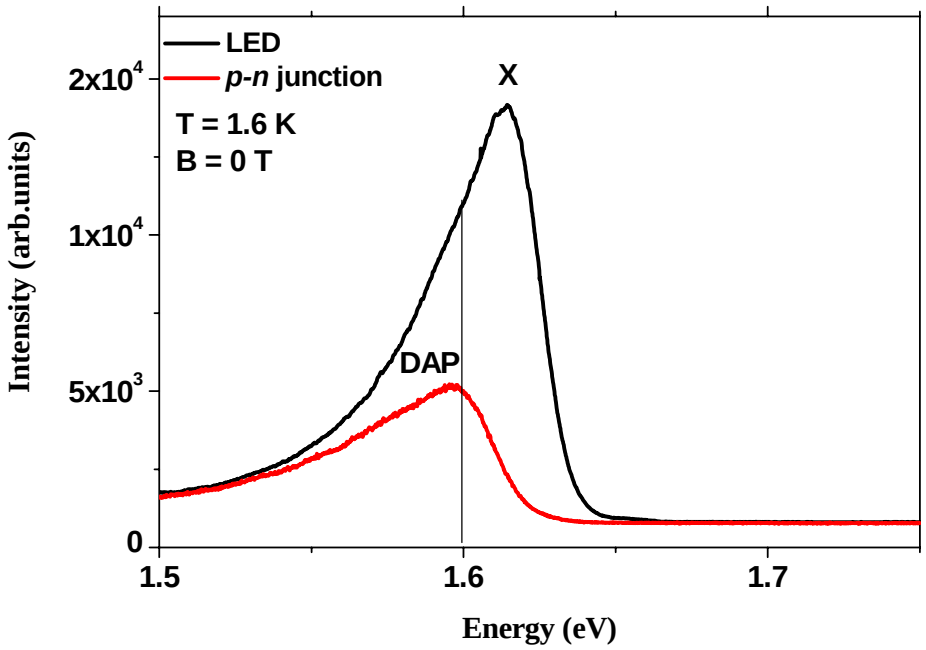

Figure 3.17 Electroluminiscence spectra measured in the absence of a magnetic field for the magnetic *p-n* junction without (red) and with (black) the magnetic quantum well at 1.4 K.

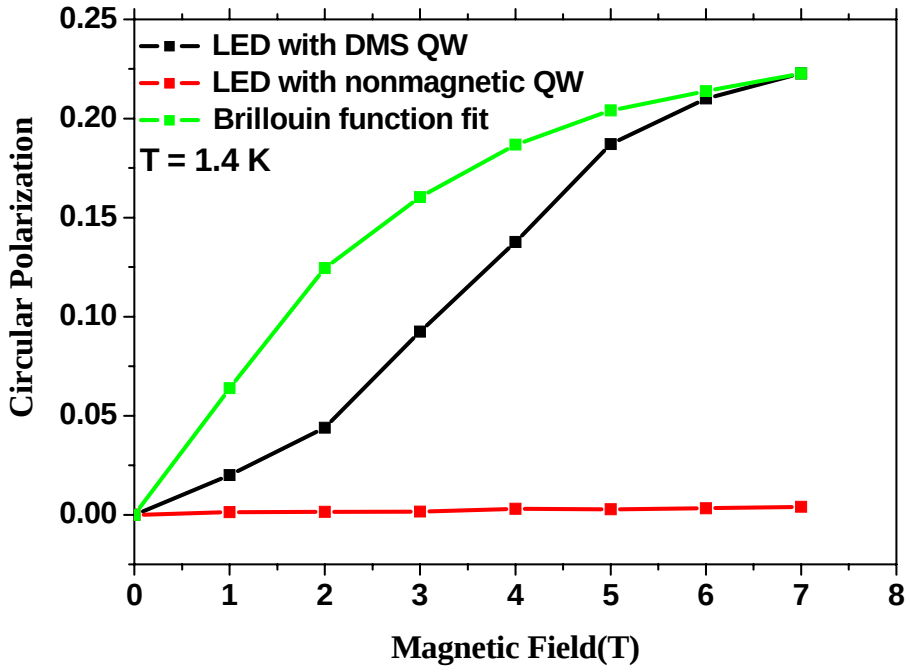

Figure 3.18 Magnetic field dependence of the circular polarization of emitted light obtained for the LED diode with the magnetic and nonmagnetic quantum wells (see text for details). The green line is fitting using a simple Brillouin function.

Green line in this figure shows the spin splitting of $Cd_{0.99}Mn_{0.01}Te$ QW calculated from a standard Brillouin function analysis and scaled by a multiplicative factor to fit polarization data [36]. As seen the calculated spin splitting fits nicely the experimental curve for $B > 5$ T. This also confirms that in this case the polarization of EL is due to spin-polarized electrons. On the other hand, a distinct deviation from the fitting Brillouin function is observed at $B < 5$ T. One of the main reasons of this discrepancy can be linked with the heating of the LED structures. Indeed, in the present case it is rather difficult to avoid this heating effect because the resistivity of the LED structure is quite high at the low temperature and, therefore, the higher current should be applied to overcome a threshold for the light emission process. For comparison, degree of circular polarization of the EL signal recorded in the *p-n* junction with a nonmagnetic quantum well is also presented in Fig. 3.18. As one can expect in this case a negligible small polarization of the electroluminescence was observed, which, moreover, stays almost constant for different values of the magnetic field applied.

Finally, Fig. 3.19 shows circular polarization of emitted light from the LED structure with DMS QW embedded between 500 Å thick $Cd_{0.80}Mg_{0.20}Te$ barriers as a function of temperature recorded at 7 T.

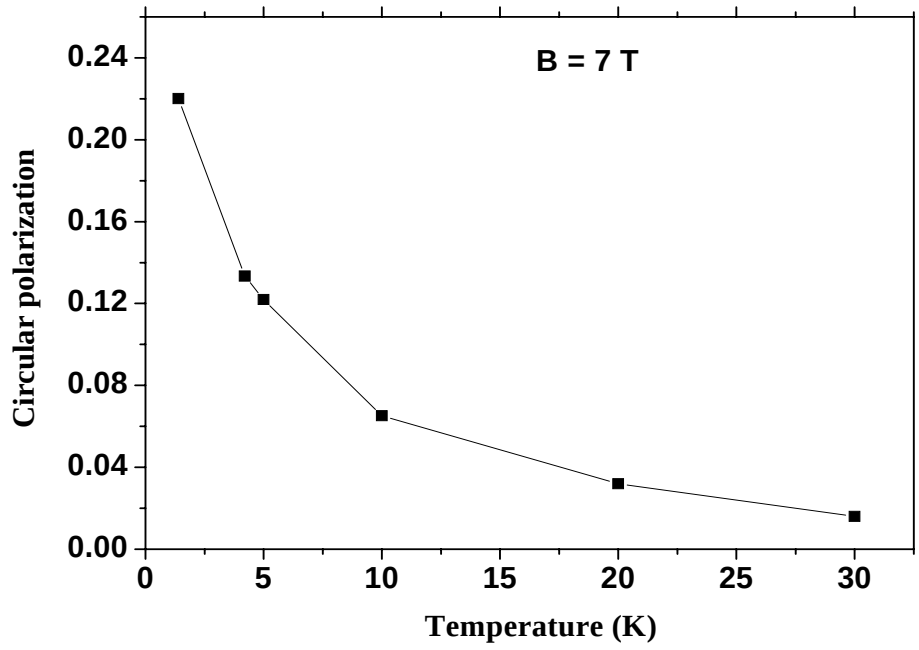

Figure 3.19 Degree of circilar polarization of the electroluminiscence as a function of temperature obtained for the LED structure with the magnetic quantum well.

As seen in this figure circular polarization decreases when temperature increases and its value becomes even lower than 2% at about 30 K. These observations can be explained by the following. First of all, it should be noticed that the local heating reduces the initial spin polarization as follows from a strong temperature dependence of a Brillouin paramagnet. On the other hand, the Zeeman spin splitting of DMS material bands is known to be very sensitive to changes of temperature. Moreover, it was shown that the value of the *g*-factor decreases significantly with increasing temperature in CdMnTe [36, 37]. All these observations can be also reflected by polarization of the electroluminescence and lead to the decrease of polarization observed as a function of temperature.

3.9 Conclusions

In this chapter, the magneto-transport measurements were used to characterize the electrical properties of the *p*-*n* junction with magnetic *p*- and nonmagnetic *n*-type regions, the *p*-*n* junction with nonmagnetic *p*- and magnetic *n*-type regions and *p*-*i*-*n* structures. In spite of theoretical predictions by Zutic and Fabian none of the magnetic effects such as spin-voltaic, spin-valve effects has been observed in these structures. We believe that there could be several reasons, which could lead to the absence of these effects.

The first one is linked with the fact that magnetically induced changes of the barrier height are very small in comparison to the initial barrier height in the unbiased diode. In support of this idea we showed that the value of Zeeman spin splitting of the conduction band calculated at 1.4 K is only about 12 meV in the magnetic *p*-*n* junction containing 15% of Mn. Moreover, this value decreases even further when temperature increases. On the other hand, the initial potential barrier height in the unbiased diode was found to be much higher and equals about 0.4 eV and 1 eV at 50 K and 300 K, correspondingly. Trying to decrease the initial potential barrier the structures with the highest possible doping level and the *p*-*i*-*n* structures were fabricated. Additionally, some of such structures were illuminated by spin polarized light. However, even in this case none of the magnetic effects has been observed. Here, it is very important to emphasize that Zutic and Fabian used very low concentrations of both electrons and holes in their calculations which lead to the quite low barrier height comparing with those in the present investigation. Due to the freeze-out effect we could not decrease concentration of free carriers too much and, thus, we believe that this could be the main reason of the absence of magnetic phenomena predicted by Zutic and Fabian.

Another reason can be linked with the fast spin-flip process of electrons to the lower energy state in the presence of magnetic field in CdMnTe layer. This could lead to a situation when the built-in potentials for spin-up and spin-down electrons are identical and, thus, exclude observation of any magnetic effects related to the identification of the spin orientation. As clearly follows no influence of magnetic field on magneto-transport measurements can be observed in this case.

The third reason which could also influence on the present results is the location of electric contacts. The spin diffusion length in CdTe-based materials is about 100 nm, and location of the contacts far away from the junction could lead to the situation, when electrons should pass a long distance (about several millimeters) without scattering in order to reach the contact region. However, during this electrons can change their orientation due to various

collisions with either magnetic ions or impurity dopants, which concentration is high enough inside the sample. This leads that instead of spin splitting of energy levels a “single” energy level exists and, then, no influence of the magnetic field can be also observed. On the other hand, following this idea one can expect that employing magnetic spin transistors operating as both voltage and current amplifier may be very useful in this case. Indeed, if a small spin current appears, which cannot be detected in the magnetic *p*-*n* junction, it could be done using the magnetic bipolar transistor structure. The results concerning this point will be presented in the next chapter of the present thesis.

Finally, in the last part of this chapter we demonstrated that the *p*-*n* junction with magnetic quantum well (CdMnTe) embedded between nonmagnetic *n*- and *p*-type regions ($Cd_{0.80}Mg_{0.20}Te$) can serve as a Light Emitting Diode. We showed that the spin polarization of the emitted light can reach 22% in such structures. However, it decreases very fast with increasing temperature.

3.10 Literature

[1] I. Zutic, J. Fabian, and S. Das Sarma, Phys. Rev. B **64**, 121201 (2001).

[2] I. Zutic, J. Fabian, and S. Das Sarma, Appl. Phys. Lett. **79**, 1558 (2001).

[3] I. Zutic, J. Fabian, and S. Das Sarma, Phys. Rev. Lett. **88**, 066603 (2002).

[4] I. Zutic, J. Supercond. **15**, 5 (2002).

[5] J. Fabian, I. Zutic, Das Sarma, Phys. Rev. B **66**, p165301(2002).

[6] J. Fabian, I. Zutic and S. Das Sarma, Phys. Rev. B **69**, 115314 (2004).

[7] J. Fabian, I. Zutic, and S. Das Sarma, Appl. Phys. Lett. **84**, 85 (2004).

[8] J. M. Marshall, D. Dimova-Malinovska, "*Photovoltaic and photoactive materials--properties, technology and applications*" (NATO Science Series II, 2002).

[9] T. Baron, K, Saminadayar, N. Magnea, J. Appl. Phys. **83 (3)**, 1354 (1998).

[10] S. M. Sze, „*Physics of Semiconductor Devices*" (John Wiley & Sons, 1969).

[11] W. D. Baker, A. G. Milnes, J. Appl. Phys. **43** (12), 5152 (1972).

[12] J. M. Woodall, J. F. Freeouf, G. D. Pettit, T. Jackson, and P. Kirchner, J. Vac. Sci. Technol. **19**, 626 (1981).

[13] Y. Fan, J. Han, L. He, J. Saraie, R. L. Gunshor, M. Hagerott, H. Jeon, A. V. Nurmikko, G. C. Hua, N. Otsuka, Appl. Phys. Lett. **61** (26), 3160 (1992).

[14] F. Erdogan, A. C. Kaya, P. F. Joseph, J. Appl. Mech. **58**, 400 (1991).

[15] F. Erdogan, Comp. Eng. **5**, 753 (1995).

[16] H. H. Berger, Solid-State Electron. **15,** 145 (1972).

[17] E. K. Evangelou, L. Papadimitriou, C. A. Dimitriades, G. E. Giakoumakis, Solid-State Electron. **36**, 1633 (1993).

[18] N. Brutscher and M. Hoheisel, Solid-State Electron. **31**, 87 (1988).

[19] T. Won, G. Munns, M. S. Unlu, H. Unlu, J. Chyi, H. Morkoc, J. Appl. Phys. **62** (9), 3860 (1987).

[20] C. T. Sah, R. N. Noyce, W. Shockley, Proc. IRE **45**, 1228 (1957).

[21] C. H. Henry, R. A. Logan, F. R. Merritt, J. Appl. Phys. **49,** 3530 (1978).

[22] V. L. Rideout, Thin Solid Films **48**, 261 (1978).

[23] M. V. Schneider, A. Y. Cho, E. Kollberg, H. Zirath, Appl. Phys. Lett. **43,** 558 (1983).

[24] R. T. Tung, Phys. Rev. B **45,** 13509 (1992).

[25] M. S. Uniu, G. Munns, J. Chen, T. Won, H. Uniu, H. Morkoc, G. Radhakrishnan, J. Katz, D. Verret, Appl. Phys. Lett. **51** (24), 1995 (1987).

[26] B. Abay, G. cankaya, H. S. Guder, H. Efeoglu, Y. K. Yogurtcu, Semicond. Sci. Technol. **18** 75 (2003).

[27] J. P. Sullivan, R. T. Tung, M. R. Pinto, W. R. Graham, J. Appl. Phys. **70**, 7403 (1991).

[28] R. Fiederling, M. Kleim, G. Reuscher, W. Ossau, G. Schmidt, A. Waag, and L.W. Molenkamp, Nature (London) **402**, 787 (1999).

[29] B. G. Streetman, "*Solid State Electronic Devices*" (Prentice Hall, New Jersey, 1980).

[30] D.H. Navon, "*Semiconductor Microdevices and Materials*" (CBS College Publishing, New York, 1986**)**.

[31] J. L. Moll, "*Physics of Semiconductor Devices*" (McGraw Hill Book Co., New York, 1964).

[32] J. E. Carroll, "*Physical Models for Semiconductor Devices*" (Edward Arnold, Cambridge 1980)).

[33] A. A. Bergh, and P. J. Dean, "*Light emitter diodes*" (Clarendon Press, Oxford, 1976).

[34] M. Kutrowski, Phd thesis, IF PAN, Warsaw, 2001.

[35] N. C. Giles, J. Lee, D. Rajavel, C. J. Summers, J. Appl. Phys. **73** (9), 4541 (1993).

[36] J. K. Furdyna and J. Kossut, "*Diluted Magnetic Semiconductors*" (Vol. 25 of Semiconductors and Semimetals Academic, New York, 1988).

[37] B. T. Jonker, A. Hanbicki, Y. D. Park, G. Itskos, M. Furis, G. Kioseoglou, A. Petrou, and X. Wej, Appl. Phys. Lett. **79,** 19 (2001).

Chapter 4. Magnetic Bipolar Transistor

4.1 The model of the magnetic bipolar transistors

Magnetic Bipolar Transistors (MBT) are build on bipolar junction transistors, conventional device schemes introduced by Shockley et al. [1] and widely used in signal amplification and processing as well as in fast logic applications. MBT is based on spin population differences relying on ensemble spin (magnetization) and can be viewed as having two magnetic *p–n* junctions connected in series, forming a three terminal device. While such an arrangement may sound like a trivial extension of the *p-n* junction diode, the new structure has the remarkable novel functionality of amplifying small current signals [2].

The concept of magnetic bipolar transistor in general is similar to the concept of magnetic diode. In a case of MBT, one part of this device (a base in the present work) was made of magnetic material exhibiting the giant spin splitting in the presence of a magnetic field, while other parts consist of nonmagnetic semiconductors (emitter and collector in the present work, respectively). Zutic and Fabian demonstrated that MBT displays a number of phenomena, which cannot be observed either in the conventional spin-unpolarized bipolar transistor or in the magnetic diode. One of such effects is electrical spin injection from the emitter to the collector which is effective in the amplification mode of the transistor. Other effects are also related to the current amplification, which could be influenced in two ways. First of all, because the equilibrium spin controls the magnitude of the equilibrium electron and hole densities, it also controls the current flowing through the transistor. Secondly, the current amplification can be also influenced by the spin-charge coupling which directly modifies the electron injection from the emitter to the collector [2-4].

At the beginning of this chapter we present details of construction of magnetic bipolar transistor based on II-VI diluted magnetic semiconductors (CdMnTe) and its electrical properties. Further, we concentrate our attention on detection of spin current in such a system using the magnetic bipolar transistor.

4.2 Practical realization of magnetic bipolar transistors

4.2.1 Schematic design and details of the MBE growth process of magnetic bipolar transistors

First of all, following considerations described in the previous paragraph we fabricated a few series of *n*-*p*-*n* magnetic bipolar transistors consisted of magnetic *p*-type base region and nonmagnetic *n*-type emitter and collector terminals. In the first series of samples concentration of Mn was kept constant (5%) while thickness of the base region was changed in the range from 0.1 μm to 4 μm. On the other hand, in the second series the thickness of the base region was kept constant (1 μm) whereas the concentration of Mn was 1%, 5%, 10%, and 15%, respectively. All parameters describing these structures are combined in Table 4.1.

Samples	Concentration of Mn, %	Thickness of base, μm	Thickness of emitter, μm	Thickness of collector, μm
N1	5	0.1	5.33	6.6
N2	5	0.5	5.33	6.6
N3	5	1	5.33	6.6
N4	5	1.5	5.33	6.6
N5	5	2	5.33	6.6
N6	5	2.5	5.33	6.6
N7	5	3	5.33	6.6
N8	5	3.5	5.33	6.6
N9	5	4	5.33	6.6
N10	1	1	5.33	6.6
N11	10	1	5.33	6.6
N12	15	1	5.33	6.6

Table 4.1 The list of *n*-*p*-*n* magnetic bipolar transistors grown by the MBE technique and investigated in the present work.

Fig. 4.1 shows a schematic structure of the *n*-*p*-*n* MBT. As seen in this figure the magnetic CdZnMnTe epilayer was doped with nitrogen acceptors and embedded between two nonmagnetic CdTe layers, both of which were doped with iodine donors and play as the emitter and collector terminals of the MBT. One should notice that in this case a small amount

of Zn (about 9%) was also added to CdMnTe. As shown in Chapters 1 and 3 this allows to significantly increase the effectiveness of the *p*-type doping in CdTe-related semiconductors. All structures have been grown on (100) oriented semi-insulating GaAs substrate, which was kept at 250^0C. To improve the sample stability and minimize the effect arising from the degradation process 4.2 μm thick undoped buffer layer of CdTe was grown between the substrate and the *n-p-n* spin transistor. In these samples 5.33 μm thick I-doped CdTe being the emitter has concentration of electrons about 8×10^{18} cm^{-3}, whereas 6.6 μm thick I-doped CdTe being the collector has concentration of electrons about 2×10^{16} cm^{-3}. The base (N-doped $Cd_{0.91-x}Zn_{0.09}Mn_xTe$) has concentration of holes about 1.2×10^{17} cm^{-3}.

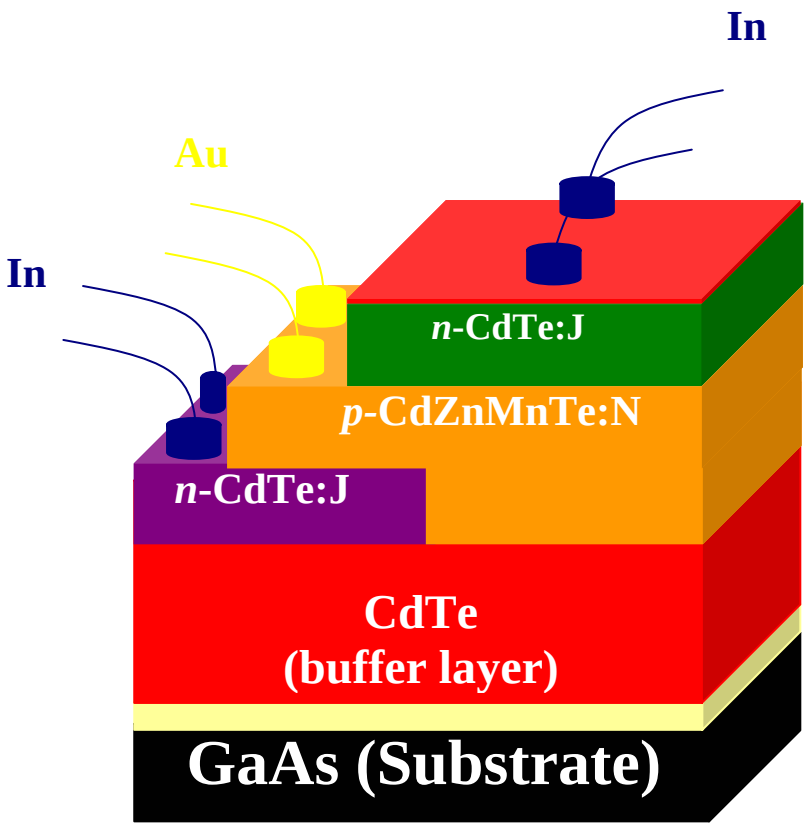

Figure 4.1 The scheme of the *n-p-n* spin transistor with magnetic *p*-type base and nonmagnetic *n*-type emitter and collector regions.

4.2.2 Formation of Ohmic contacts

Similar to the case of the magnetic diodes Ohmic contacts to the *n*-type CdTe were made by annealing of indium dots in air at about 170^0C for 20-30 s. Before this as shown in Fig. 4.1 a part of the *p*-type region was removed by etching in methanol solution with 0.5% bromine (Br_2-CH_3OH) for 5 seconds. To protect other parts of the *p*-type region and the

whole *n*-type collector the vacuum grease "Apiezon N" was used as a mask. After etching this mask was removed by rinsing the *n-p-n* structure in the C_2HCl_3 solution. The contacts to the *p*-type region were formed by silver paste on gold-palladium (85% gold and 15% palladium) contact points, which had been sputtered on the surface of the *p*-type region.

The quality of all contacts has been checked by measuring *I-V* characteristics of MBT at room temperature. The measurements were performed between various pairs of coplanar contact pads for both *n*- and *p*- type regions of MBT as shown in Fig. 4.1.

Figure 4.2 shows the *I-V* characteristics of the spin transistor's contacts measured for three different cases. Figure 4.2 (a) shows collector current versus collector-emitter voltage. The *I-V* characteristic for the base current as a function of voltage applied between the emitter and the base are presented in Fig. 4.2 (b). At last, the *I-V* characteristic shown in Fig. 4.2 (c) represents the collector current versus the collector-base voltage. As seen in Fig 4.2 (a) the collector current changes linearly as a function of the collector-emitter voltage. This clearly shows that the collector contact has an Ohmic behavior. On the other hand, the *I-V* characteristics of the ordinary forward biased diode are shown in Figs. 4.2 (b) and (c). A small difference in these characteristics can be explained by different doping levels of the emitter and the collector in such structures.

4.3 Electrical characterization of magnetic bipolar transistors

4.3.1 Electrical parameters of MBT

Generally, a transistor can be measured in three circuit configurations with corresponding input and output currents and voltages: common-base, common-emitter, and common-collector. These configurations are also referred to as the basic amplifying circuits.

The relation between the input and output currents and voltages may be presented by a minimum of two sets of characteristic curves for any of the three transistor configurations, since all other curves may be derived from these two. From technical point of view, the available power gain of the transistor in the common-emitter configuration is higher than it is in either of the other two configurations [5]. Therefore, in the present work all measurements were performed in the forward active mode and in configuration with common-emitter, at which the emitter–base junction is forward biased and the base–collector junction is reverse biased. In this latter configuration, the input resistance of the transistor is low compared with the output resistance, and in fact, is low compared with the internal resistance of a bias supply connected to the base.

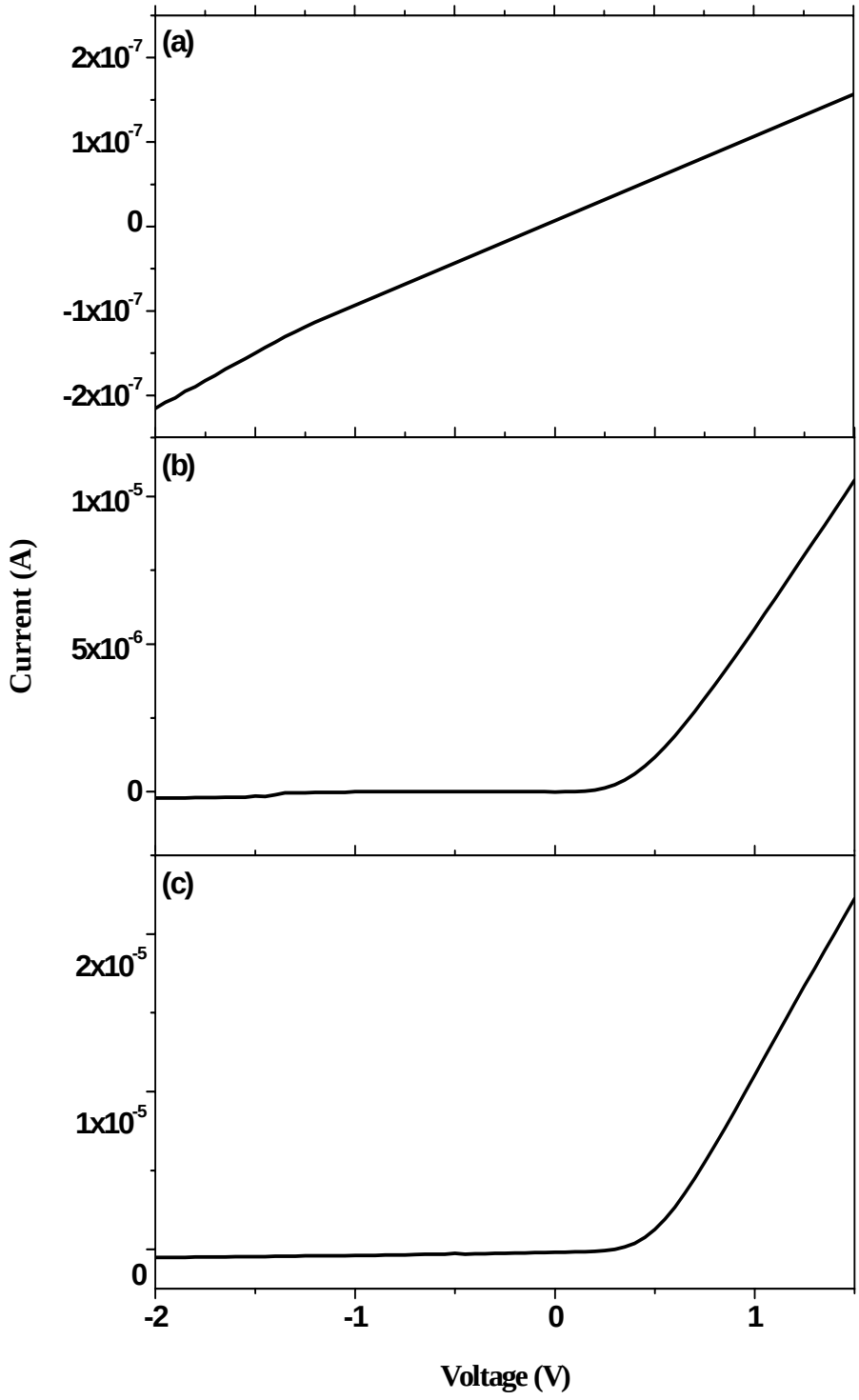

Figure 4.2 Current-Voltage characteristics measured between different contacts of MBT (see the text for details).

The transistor base and emitter form the elements of a diode, which is biased in the forward direction, so that the current is easily controlled, while the voltage is not. It is therefore considerably more difficult to control the input or base-to-emitter voltage than it is to control the base current. The collector circuit is usually a high-impedance circuit compared with the internal resistance of the energizing source feeding the collector. Consequently, it would seem that the collector voltage is more easily controlled than is the collector current, so that the collector voltage rather than current is more naturally the independent variable. Therefore, in configuration with common-emitter the input parameters are base current and voltage between base and emitter, and the output are collector current and voltage between collector and emitter. A huge practical value always has the output characteristics, which testify about correct working of the device [5].

Figure 4.3 shows the output characteristics of the *n*-*p*-*n* spin transistor with magnetic *p*-type base (N-doped $Cd_{0.86}Zn_{0.09}Mn_{0.05}Te$) and nonmagnetic *n*-type emitter and collector terminals which are I-doped CdTe in common-emitter configuration , which were measured in the absence of magnetic field at 4.2 K. In other words the collector current as a function of collector-emitter voltage V_{CE} for a constant value of the base current I_B was presented in this figure. Also similar curves for the structures having different values of the base current are shown in this figure. The widths of the base region were 1 μm (see Fig. 4.3 (a)) and 2 μm (see Fig. 4.3 (b)), correspondingly.

As seen in Figs. 4.3 (a) and (b) the collector current I_C increases as a function of V_{CE} for small voltages (less than 1 V). Further, it becomes almost constant and is entirely determined by the base current I_B. The insets in Figs. 4.3 (a) and (b) show the enlarged I_C-V_{CE} characteristics which correspond to the lower values of the base current than 10^{-5} A. As follows from these figures no significant influence of the width of the base region on electrical properties of MBT has been observed for low values of the base current varying in the range from 10^{-8} A to 10^{-6} A. However, as seen in Fig. 4.3 (b) for the base current of 10^{-5} A the collector current increases much slower with increasing V_{CE} in comparison to the analogous case of MBT with the smaller width of the base region. Moreover, in this case the saturation regime of the spin transistor was shifted towards the higher voltages. However, in both cases the breakdown of the spin transistor was observed if the base current becomes higher than 10^{-4} A. The curves, which correspond to this regime, are shown in black and blue in Figs. 4.3 (a) and (b), correspondingly. Moreover, as seen in Fig. 4.3 the collector current I_C is not equal zero in the absence of the base current. This is a well-known phenomenon which can be explained by intrinsic conduction of semiconductors [6, 7].

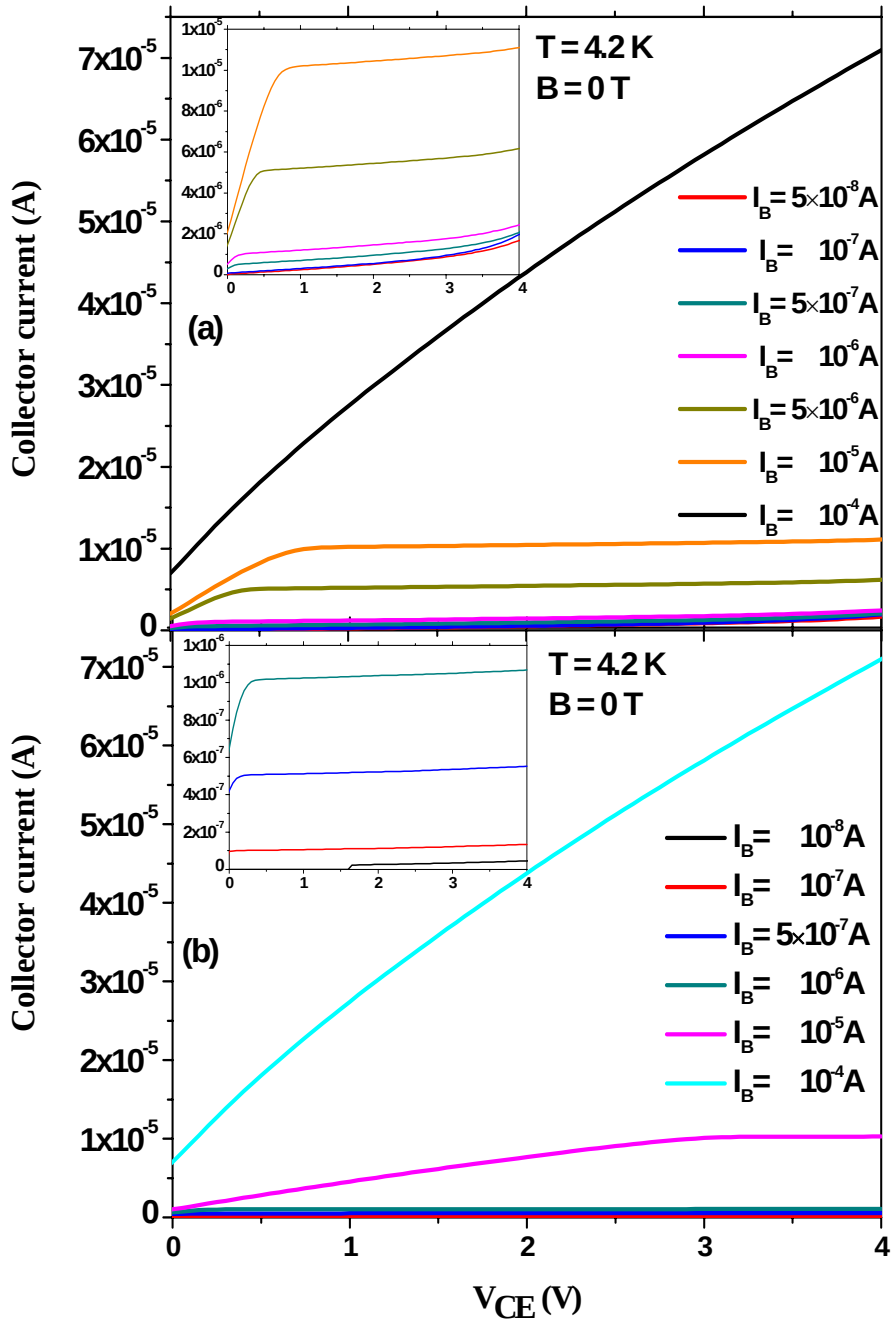

Figure 4.3 Current-Voltage characteristics of the *n-p-n* spin transistor with magnetic *p*-type base ($Cd_{0.86}Zn_{0.09}Mn_{0.05}Te$) and nonmagnetic *n*-type emitter (CdTe) and *n*-type collector (CdTe). These characteristics were measured in configuration with the common emitter in the absence of magnetic field at 4.2 K. The width of the base was 1 μm (a) and 2 μm (b), correspondingly. The insets show the enlarged I_C-V_{CE} characteristics which correspond to the base current lower than 10^{-5} A.

It is necessary to note that MBT's with the base region smaller than 1 μm have been also fabricated in this work. However, in these structures we were not able to fabricate a good quality Ohmic contact to the *p*-type base. On the other hand, if the base region of the transistor is thicker than 2.5 μm then all injected electrons from the emitter regions recombine in the base before reaching the base-collector junction. Thus, instead of the *n*-*p*-*n* structure we observed two diodes which are connected back to back. Another interesting thing is that in the structures with the base region above 2.5 μm we could not perform transport measurements below 40 K, whereas it is possible to be done if the base region of the transistor is below 2.5 μm. We believe that this is related with the following. Because the activation energy of nitrogen and iodine in CdTe is about 56 meV [8] and 3 meV [9], respectively, the resistivity of the *p*-type material is much higher than that in the *n*-type material at low temperature. Then, if the thickness of the *p*-type region is much smaller than that of the *n*-type region then the whole resistance stays almost unchanged, what is indeed observed in such structures.

Another feature observed in Fig. 4.3 is a displacement of the output characteristics when the base current is changed. Like in a case of ordinary bipolar transistors, this displacement is related to an increase of the emitter current under assumption that the voltage on the collector is constant while the base current increases and can be described by the following equation [7]:

$$H_{21E} = \frac{I_C - I_{CB0}}{I_B + I_{CB0}}\ , \qquad (4.1)$$

where H_{21E} is the forward short-circuit current amplification factor, I_{CB0} is the reverse current of the collector, which is determined under the assumption that the emitter current is equal zero.

Heavy doping of the emitter region and light doping of the base region cause many more electrons to be injected from the emitter into the base than holes to be injected from the base into the emitter. For practical purposes it is interesting to know the current gain parameter (β_0), which is defined as the ratio between changes of the collector current to changes of the base current at the constant bias applied to the base (see chapter 1). This parameter usually varies in the range of 20 and 200 for Si-based bipolar junction transistor [7].

In the *n*-*p*-*n* spin transistor with magnetic *p*-type base and nonmagnetic *n*-type emitter and collector terminals the current gain β_0 was evaluated to be only about 1.24 for both

transistors having 1 μm and 2 μm base regions. Moreover, this coefficient was found do not depend on the base current. As clearly follows the collector current is almost equal to the base current, which consists of two components: the first one is the current due to an inward flow of electrons to replace those lost in the hole injection and diffusion processes; the second one is the leakage current of collector. This means that it is very likely that the potential barrier between *n*-type emitter region and *p*-type base region is still too high for electrons and only a small part of them can overcome this barrier to be injected into the collector.

Another important parameter, which can be calculated from the output transistor characteristics is the output admittance with input open h_{22E}, which is described by the following equation:

$$h_{22E} = \left(\frac{\Delta I_C}{\Delta V_C}\right)_{I_B=const}, \tag{4.2}$$

In the present work the value of this parameter was calculated to be 0.4 $\mu\Omega^{-1}$ and 0.26 $\mu\Omega^{-1}$ for the spin transistor with the width of the base region of 1 μm and 2 μm, respectively. For comparison, in silicon bipolar transistor the output admittance with input open changes in the range from 10^{-4} to 10^{-5} Ω^{-1} [5, 7], and, thus, is about 2-3 order of magnitude higher than in the present case.

4.3.2 Magnetic field effect on electrical characteristics of the magnetic bipolar transistor

As mentioned above, magnetic field causes the giant Zeeman splitting of energy bands in DMSs at low temperature. This leads that different heights of the potential barrier for electrons with different spin orientation appear in MBT. Thus, upon applying magnetic field one expects that the emitter-base barrier for spin-down electrons will be smaller than that for spin-up electrons. If the base width is sufficiently small, electrons injected from the emitter can diffuse through the base reaching the base-collector depletion edge and then “float up” into the collector. In a forward active mode, at which the emitter–base junction is forward biased and the base–collector junction is reverse biased, we could also significantly reduce the barrier for both spin orientation of electrons. Thus, one can expect that in the defined range of voltages we could observe only the movement of spin-down electrons through the base towards the collector.

Figure 4.4 shows the output characteristics of the *n-p-n* spin transistor with magnetic N-doped base region ($Cd_{0.86}Zn_{0.09}Mn_{0.05}Te$) and nonmagnetic I-doped emitter and collector terminals (CdTe) in common-emitter configuration in the presence of magnetic field at 4.2 K. Similar to the previous case (see Fig. 4.3) the I_C-V_{CE} curves in this figure correspond to the spin transistors having 1μm (a) and 2 μm (b) widths of the base region, respectively. In both these cases the base current was constant and equal 10^{-5} A. The magnetic field changes in the range from -8 to 8 T. For the sake of clarity, only curves measured without and with magnetic field of 3 T are presented in this plot.

As seen in Fig. 4.4 the I_C-V_{CE} characteristics of the spin transistors are identical with (3T) and without the magnetic field applied. Similar results have been also observed for the higher values of magnetic field applied (up to ± 8 T). Moreover, no changes have been detected in the samples with the higher concentration of the magnetic impurity (10% and 15%).

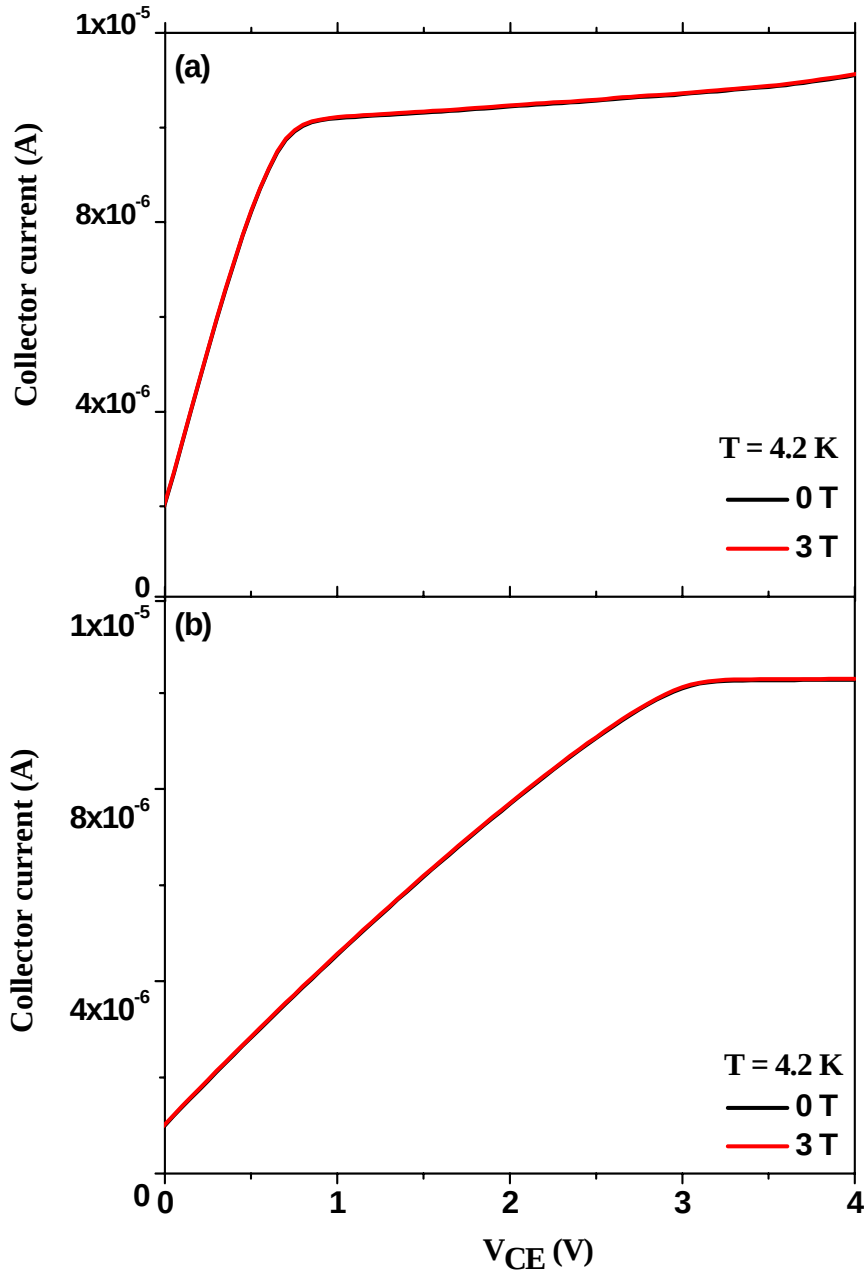

Figure 4.4 The output characteristics of the *n-p-n* spin transistor with magnetic N-doped base region ($Cd_{0.86}Zn_{0.09}Mn_{0.05}Te$) and nonmagnetic I-doped emitter and collector (CdTe) regions in common-emitter configuration. The widths of the base region were 1 μm (a) and 2 μm (b), correspondingly. For the sake of clarity, only curves measured without and with (3 T) magnetic field are shown.

4.4 Conclusions

In this chapter, we presented results of magneto-transport measurements in the *n-p-n* magnetic bipolar transistor structures. As mentioned in the previous chapter using MBT, which can act as both current and voltage amplifier we expected to observe the higher spin current comparing with that in the magnetic diode. However, even in this case none of magnetic effects predicted by Zutic and Fabian has been observed. Thus, it is very likely that similar to the case of the magnetic diode the absence of magnetic effects is rather linked with the high potential barrier between the emitter and the base.

However, besides the high potential barrier various mechanisms of spin relaxation such as Elliott-Yafet, D'yakonov-Perel, Bir-Aronov-Pikus, and Hyperfine-interaction cannot be also excluded as a possible reason which may contribute to the absence of magnetic phenomena predicted by Zutic and Fabian.

4.5 Literature

[1] W. Shockley, M. Sparks, and G. K. Teal, Phys. Rev. **83**, 151 (1951).

[2] I. Zutic, J. Fabian, S. C. Erwin, IBM Journal of Research and Development **50** (1), 121 (2006).

[3] J. Fabian, I. Zutic, Phys. Rev. B **69,** p115314 (2004).

[4] J. Fabian, I. Zutic, and S. Das Sarma, Appl. Phys. Lett. **84** (1), 85 (2003).

[5] A. W. Lo, R. O. Enders, J. Zawels, F. D. Waldhauer, C. C. Cheng, "*Transistor Electronics*" (Englewood Cliffs, New Jersey, 1955).

[6] R. Murugeshan, K. Sivaprasath, "*Modern Physics*" (S Chand & Company LTD, New Delhi, 2005).

[7] V. V. Pasynkov, L. K. Chirkin, „*Semiconductor Devices*" (Vysshaya Shkola, Moscow, 1987).

[8] M. Moldovan, L. S. Hirsch, A. J. Ptak, C. D. Stinespring, T. H. Myers, and N. C. Giles, J. Electron. Mat. **27** (6), 756 (1998).

[9] D. A. Jenny and R. H. Bube, Phys. Rev. **96** (5), 1190 (1954).

Chapter 5. Spin quantum wells and spin superlattices

In this chapter, we would like to concentrate our attention on investigation of magnetic effects in spin quantum wells and spin superlattice structures.

Superlattices are periodically arranged layers of semiconductor materials having different energy-band parameters with a periodicity much greater than the fundamental lattice constant. The macroscopic properties of any semiconductor heterostructure are determined largely by the relative alignments of the conduction and valence bands at the interface. The incorporation of diluted magnetic semiconductors in such heterostructures allows one's to use the large band-edge spin splitting which characterize these compounds to tune the band offsets over a rather large range. Von Ortenberg *et. al.* [1] was one of the first who proposed that an external magnetic field applied to the semimagnetic superlattice induces a periodic, spin-dependent potential and forms a "spin superlattice" consisting of spatially separated spin states. Supporting this idea Dai *et. al.* [2] demonstrated formation of a magnetic-field-induced spin superlattice in modulated $ZnSe/Zn_{1-x}Mn_xSe$ structures using the magneto-optical measurements. In that work it was showed that 5% of Mn is the optimal value to create an ideal alloy composition. Moreover, in this case band offsets in both the conduction and valence bands become less than 5 meV in the absence of magnetic field. On the other hand, when magnetic field is applied to the structure the band edges in the magnetic semiconductor undergo a huge spin splitting due to the *sp-d* exchange between carriers and localized magnetic ions. The splitting in the nonmagnetic layers is much smaller in this case. Similar results have been reported for some other systems consisted of spin superlattices [3, 4]. One should emphasize that in all these works the investigated superlattices have not been intentionally doped.

The main idea used in the present work is to examine magneto-optical and magneto-transport properties of electrons confined in the shallow magnetic quantum well and relying on these properties try to build a good quality spin superlattice structures. One should notice that due to similar valence band offset ($Q_V = 0.30$) of $Cd_{1-x}Mn_xTe$ and $Cd_{1-y}Mg_yTe$ even for large values of Mn and Mg content (up to 27%) [5, 6] the system of $Cd_{1-x}Mn_xTe/Cd_{1-y}Mg_yTe$ is the ideal structure for investigation of characteristics of spin superlattice structures. That is why the superlattices consisted of such materials are used in the present work. However, before the spin superlattices with a large number of the quantum wells are fabricated, the more simple structures with zero band offsets between the magnetic and nonmagnetic matrix

have been grown. Investigation of such simple structures may help us to understand deeper the origin of transport effects and optical phenomena observed in more complicated systems such as the spin superlattices.

5.1 Practical realization of shallow spin quantum well and spin superlattice structures

5.1.1 Spin quantum wells formation in CdMgTe/CdMnTe matrixes

Single diluted magnetic semiconductor quantum well (SDMSQW) structures $Cd_{1-x}Mn_xTe$ which are modulation I-doped and embedded between $Cd_{1-y}Mg_yTe$ barriers have been grown by the MBE technique on (100)-oriented semi-insulating GaAs substrates. Contents of Mn and Mg in CdMnTe and CdMgTe layers, respectively, were adjusted to form a shallow well in 100 Å thick CdMnTe layer. One should notice that we would like to fabricate structures in which no quantum wells are observed in the absence of magnetic field whereas the confining potential is induced by applying the magnetic field. All grown SDMSQW structures can be divided in two groups. The first one is a series of samples with different width of the doped region varying in the range from 4 Å to 200 Å, whereas the width of the spacer layer was kept constant (200 Å). In the second series of samples, the width of spacer layer changes from 0 to 600 Å, whereas the width of the doped region was kept constant (100 Å). All growth parameters are combined in Table 5.1.

Before growing the SDMSQW structures the buffer layer of $Cd_{1-y}Mg_yTe$ (4.2 μm) was fabricated on the top of the substrate to release the interfacial strains arising from the lattice mismatch. Afterwards 100 Å thick $Cd_{1-x}Mn_xTe$ well was grown directly on the buffer layer. 2DEG was formed by placing I-doped $Cd_{1-y}Mg_yTe$ layers, which were separated from the quantum well by intrinsic $Cd_{1-y}Mg_yTe$ spacers. During the growth procedure temperature of the substrate was about 265^0C, whereas the temperature of I effusion cell was 190^0C ($n_e = 3\times10^{18}$ cm^{-3}). From the top the whole structure was covered with 2000 Å thick cap layer consisted of $Cd_{1-y}Mg_yTe$. For the sake of clarity, the schematic layer structure of the modulation doped single DMS quantum well of CdMnTe embedded between CdMgTe barriers is shown in Fig. 5.1 (a).

Samples	Concentration of Mn, %	Concentration of Mg, %	Spacer layer width, Å	Quantum well width, Å	Doped layer width, Å	Cap layer width, Å
N1	5	5	200	100	4	2000
N2	5	5	200	100	8	2000
N3	5	5	200	100	16	2000
N4	5	5	200	100	25	2000
N5	5	5	200	100	50	2000
N6	5	5	200	100	75	2000
N7	5	5	200	100	100	2000
N8	5	5	200	100	150	2000
N9	5	5	200	100	200	2000
N10	5	5	600	100	100	2000
N11	5	5	500	100	100	2000
N12	5	5	300	100	100	2000
N13	5	5	200	100	100	2000
N14	5	5	100	100	100	2000
N15	5	5	50	100	100	2000
N16	5	5	0	100	2*50	2000
N17	5	5	0	100	2*75	2000
N18	5	5	0	100	2*100	2000
N19	5	5	0	100	2*200	2000
N20	5	6	200	100	100	2000
N21	5	4	200	100	100	2000
N22	1	1	200	100	100	2000
N23	10	10	200	100	100	2000
N24	10	10	200	100	50	2000
N25	10	10	200	100	25	2000
N26	10	10	200	100	12	2000
N27	15	15	200	100	100	2000
N28	15	15	200	100	50	2000

Table 5.1 Growth parameters of SDMSQW structures.

5.1.2 Spin superlattices formation in CdMgTe/CdMnTe matrixes

Similar to the case of spin quantum wells described in the previous section a few series of superlattice structures with different Mn and Mg content have been grown. The

schematic layer structure of spin superlattices is shown in Fig. 5.1 (b). All growth parameters used during the MBE process are combined in Table 5.2.

Samples	Concentration of Mn, %	Concentration of Mg in the barrier, %	Spacer layer width, Å	Quantum well width, Å	Doped layer width, Å	Cap layer width, Å
N1	12	7	100	100	100	2000
N2	12	12	100	100	100	2000
N3	12	13	100	100	100	2000
N4	5	5	50	200	4	2000
N5	5	5	50	200	12	2000
N6	5	5	50	200	25	2000
N7	5	5	50	200	50	2000
N8	5	5	50	200	75	2000
N9	5	5	50	200	100	2000
N10	5	5	50	200	150	2000
N11	5	5	50	200	200	2000
N12	0	5	50	200	100	2000
N13	1	5	50	200	100	2000
N14	14	5	50	200	100	2000
N15	5	5	100	200	100	2000
N16	5	5	120	200	100	2000
N17	5	5	200	200	100	2000
N18	5	5	250	200	100	2000
N19	5	5	400	200	100	2000
N20	5	5	600	200	100	2000

Table 5.2 Growth parameters of spin superlattice structures.

In the first series each sample consisted of 50 individual layers of magnetic $Cd_{0.88}Mn_{0.12}Te$ and nonmagnetic $Cd_{1-y}Mg_yTe$ epilayers which were grown on $Cd_{1-y}Mg_yTe$ buffer layer. The thickness of each layer was 100 Å. Content of Mg was varied 7%, 12% and 13%, respectively. Temperature of I cell was 190^0C. It should be noticed that in this series of samples no modulation doping has been used. All superlattice structures were doped by iodine whereas the buffer and cap layers were undoped.

In the second series the samples were modulation doped and consisted of 25 loops of magnetic $Cd_{1-x}Mn_xTe$ layer and nonmagnetic $Cd_{1-y}Mg_yTe$ barrier. The thickness of each layer was 200 Å in this case. Additionally, in this series the width of the doped layer was varied in

the range from 4 Å to 200 Å, whereas the width of the spacer layer was kept constant (50 Å). In the third series of samples the width of the spacer layer was varied in the range from 50 Å to 600 Å, whereas the width of the doped region was kept constant (100 Å).

One should notice that in all these series the cap layer consisted of 2000 Å thick $Cd_{1-y}Mg_yTe$ was used to cover the whole structure. However, in the first series of samples content of Mg in the cap layer is equal to those in the barrier and buffer layers while in the second and third series this content was chosen to be equal to concentration of Mg in the buffer epilayer (y = 30%). Therefore, from this point of view the structures in the second and third series look like a wide quantum well in which modulation doped superlattices are created. Finally, all superlattice structures were doped by iodine whereas the buffer and cap layers were kept undoped.

The schematic view of energy bands for the spin superlattice without and with magnetic field applied is shown in Figs. 5.1 (c) and (d). As shown in Fig. 5.1 (c) contents of Mn and Mg were chosen in such way that both the conduction and valence bands in CdMnTe and CdMgTe perfectly match each other in the absence of magnetic field. As a consequence carriers are not spatially confined. Due to the giant spin splitting in the presence of a magnetic field the bands of the DMS material split and carriers with opposite spins gather in different regions: spin-down electrons in the DMS layers and spin-up electrons in the nonmagnetic layers (Fig. 5.1 (d)).

5.2 Magneto-optical measurements of SDMSQW and spin superlattice structures

In this part of the work results of magneto-optical measurements of SDMSQW and spin superlattice structures are presented. These measurements were performed using the photoluminescence (PL) technique in the presence of magnetic field which was varied from -8.5 T to 8.5 T at T = 4.2 K.

Figure 5.2 shows the PL spectra of the modulation doped SDMSQW $Cd_{0.85}Mn_{0.15}Te$/ $Cd_{0.85}Mg_{0.15}Te$ structure measured with σ^- (Fig. 5.2 (a)) and σ^+ (Fig. 5.2 (b)) circular polarization for different values of the magnetic field at 4.2 K. For such Mn and Mg contents zero band offsets between the magnetic and nonmagnetic regions are expected to be formed. The width of the quantum well, the intrinsic spacer and the doped region were 100 Å, 200 Å and 100 Å, respectively.

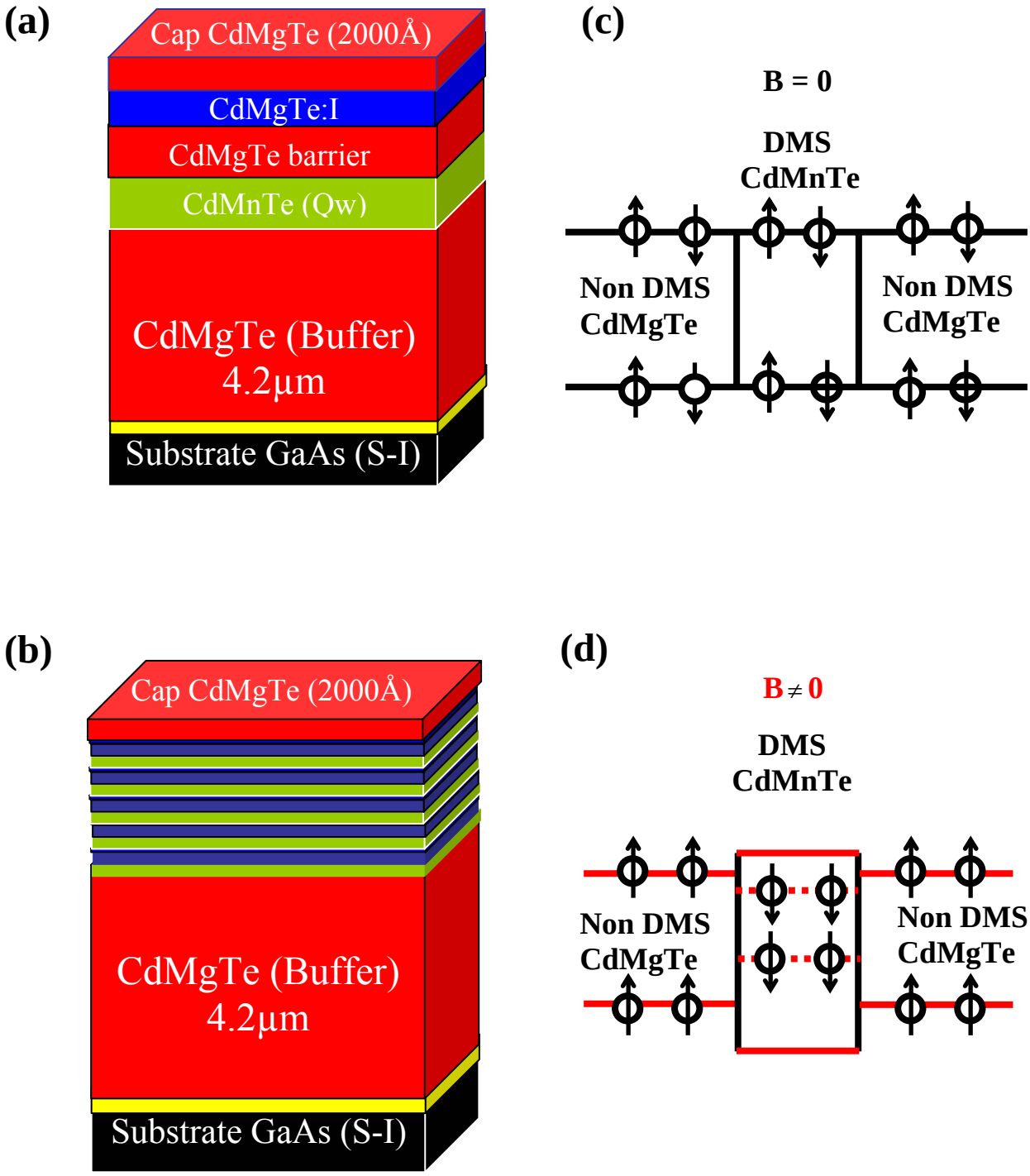

Figure 5.1 The schematic layer structures of the modulation doped magnetic-field-induced single DMS quantum well consisted of CdMnTe embedded between CdMgTe barriers (a) and spin superlattice structures (b). The schematic view of the energy bands for the spin superlattice, which consists of alternating layers of non DMS and DMS materials with equal band gaps with and without the magnetic field, are presented in Figs. (c) and (d).

As shown in Fig. 5.2 one dominant peak at 1.825 eV was observed in the absence of magnetic field. Applying the magnetic field a similar spectrum was obtained for σ^- polarization, whereas this emission line splits into two components for σ^+ polarization. In this latter case the first dominant component at 1.825 eV is not also affected by the magnetic field and, therefore, one can assign this peak to the signal originating from the nonmagnetic CdMgTe matrix. On the other hand, changing the magnetic field a significant red-shift of another smaller component was observed (Fig. 5.2 (b)). This indicates that this signal is very likely to originate from a transition in the magnetic CdMnTe layer. One should emphasize that the peaks originating from magnetic CdMnTe quantum well and nonmagnetic CdMgTe barrier are very close in energies in the absence of magnetic field. This is entirely consistent with that these materials were grown in such way that their energy gaps are almost identical at B = 0 T.

Figure 5.3 shows the PL spectra of the spin superlattice structure consisted of 50 individual layers of 100 Å thick $Cd_{0.88}Mn_{0.12}Te$ and $Cd_{0.87}Mg_{0.13}Te$ epilayers measured with σ^- (Fig. 5.3 (a)) and σ^+ (Fig. 5.3 (b)) circular polarizations for different values of the magnetic field at 4.2 K. One should notice that this ratio of Mn and Mg contents forms a structure containing so-called shallow quantum well. As shown in Fig. 5.3 two PL peaks at 1.7712 eV and 1.7811 eV were observed in the absence of magnetic field for both circular polarizations in this case. However, the pattern becomes different when magnetic field is applied to the structure. For σ^- polarization a slight blue-shift of the low-energy peak at 1.7712 eV was observed, whereas the position of the second peak was constant. On the other hand, for σ^+ polarization we observed that the peak at 1.7811 eV is almost independent to magnetic field changes whereas another peak at 1.7712 eV shows a significant red-shift in the PL spectrum. In analogy to the modulation doped SDMSQW $Cd_{0.85}Mn_{0.15}Te$/ $Cd_{0.85}Mg_{0.15}Te$ structures one can assume that the peak which shifts with magnetic field is very likely linked with a transition inside the magnetic CdMnTe layer whereas the peak which is not influenced by the magnetic field corresponds to a transition in the nonmagnetic CdMgTe barrier.

One should notice that in both these cases presented in Figs. 5.2-5.3 upon applying magnetic field the spin-down level of electrons shifts down forming the quantum well for such electrons inside the structure. Then one can say that the electrons occupied this level are confined inside the DMS material in this case. On the other hand, the opposite tendency is expected for the spin-up level of electrons. Applying magnetic field this level raises up and it is possible to create the potential magnetic barrier inside the structure at high values of the magnetic field.

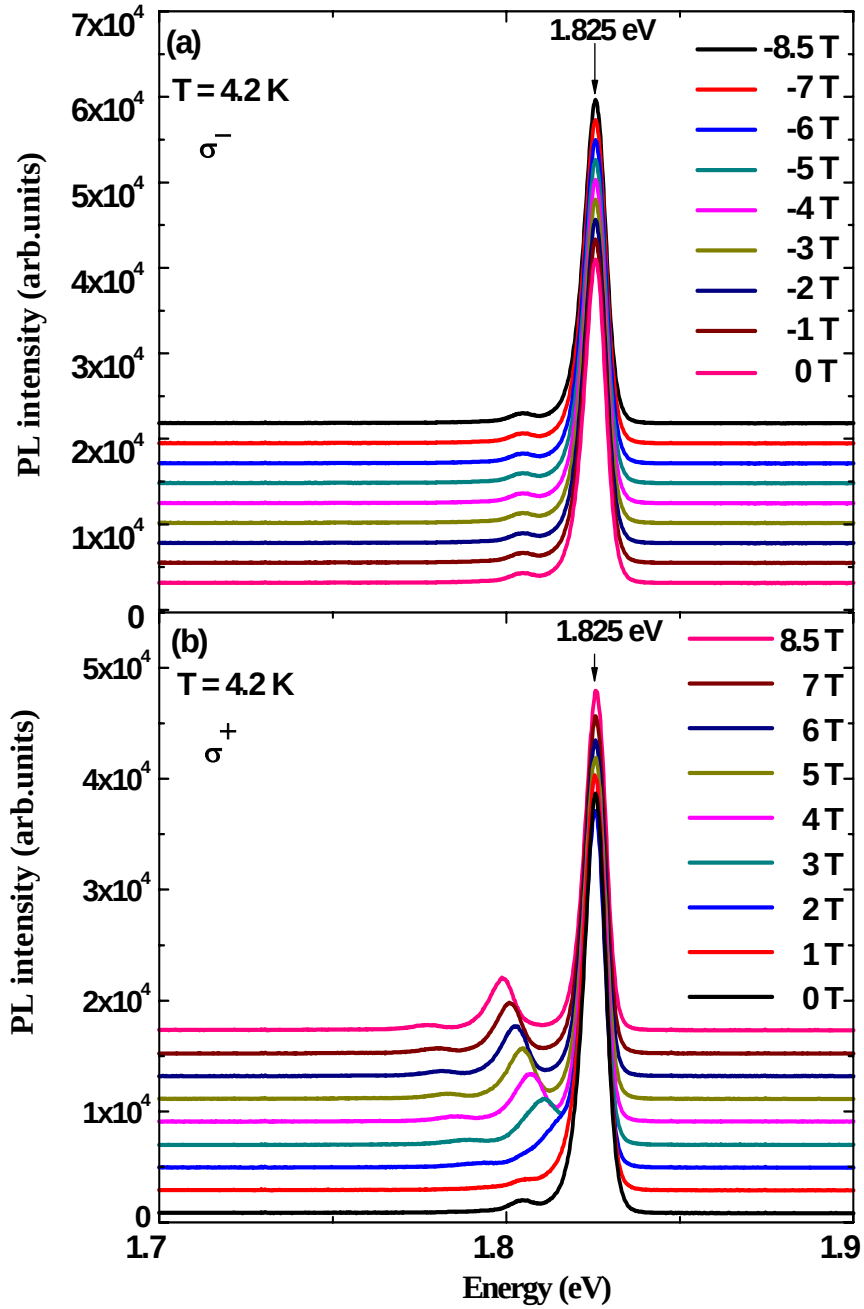

Figure 5.2 PL spectra recorded in the modulation doped SDMSQW $Cd_{0.85}Mn_{0.15}Te$/ $Cd_{0.85}Mg_{0.15}Te$ structure obtained with σ^- (a) and σ^+ (b) circular polarizations for different values of the magnetic field at 4.2 K.

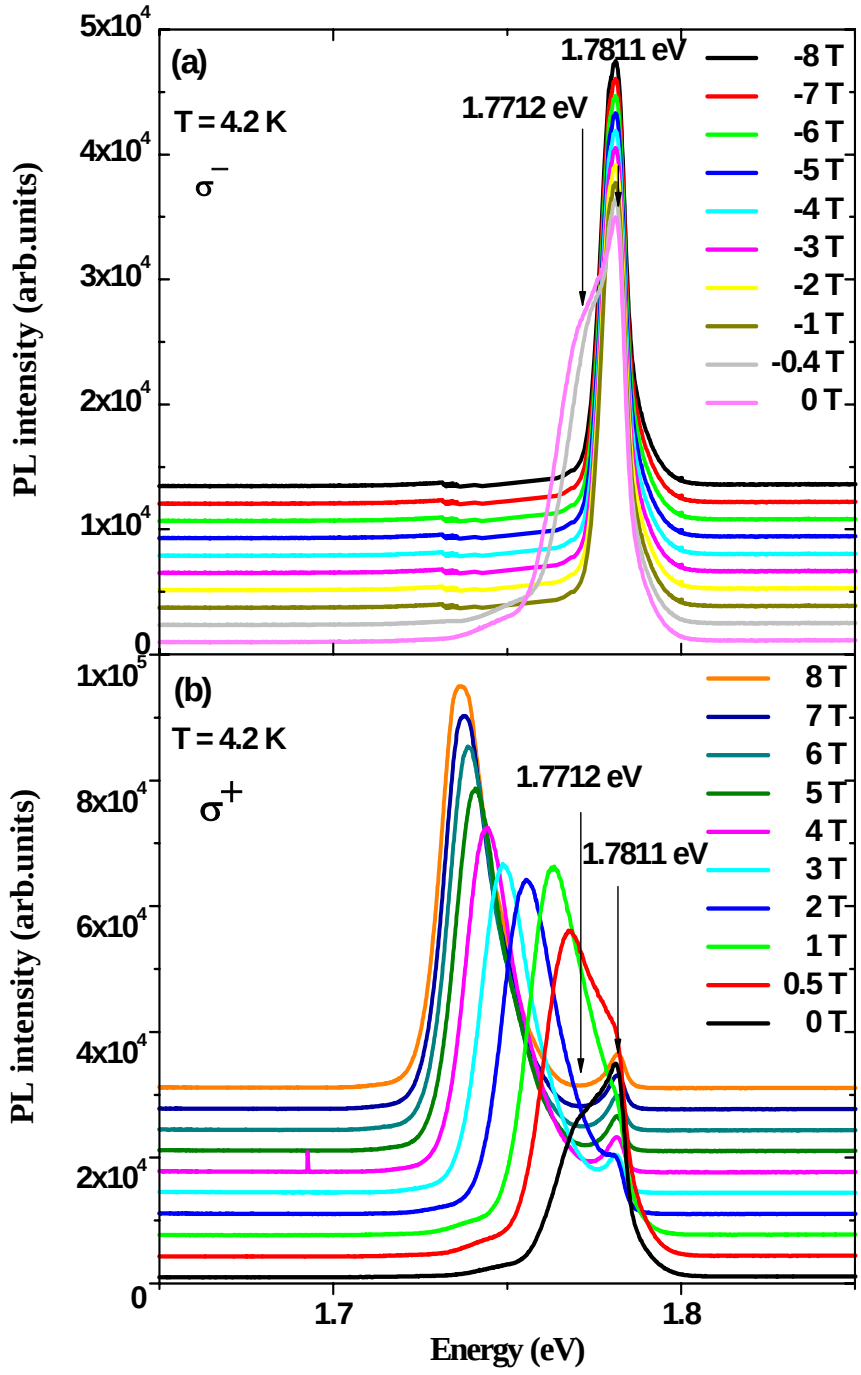

Figure 5.3 PL spectra recorded in the spin superlattice structure with the magnetic $Cd_{0.88}Mn_{0.12}Te$ quantum well embedded between $Cd_{0.87}Mg_{0.13}Te$ barriers obtained with σ^- (a) and σ^+ (b) circular polarizations for different values of the magnetic field at 4.2 K.

Following this idea and using the positions of the PL peaks shown in Figs. 5.2-5.3 one can calculate the depth of the magnetic quantum well and the height of the magnetic barrier for spin-up and spin-down electrons, respectively. In these calculations we assume that the largest part of the spin splitting of the band edges of the DMS material occurs in the valence band (about 80%) due to the stronger *p-d* shell exchange coupling whereas the rest of this splitting (about 20%) happens in the conduction band [7]. Additionally, we performed these calculations only for conduction band electrons because holes are known to lose their spin orientation very quickly as a result of strong spin–orbit coupling in the valence band and their practical application for the spintronics is significantly impeded [8].

Figure 5.4 shows a schematic diagram of changes of the conduction band offset between the non DMS (CdMgTe) and DMS (CdMnTe) materials for spin-up and spin-down electrons calculated in the presence of magnetic field in two cases.

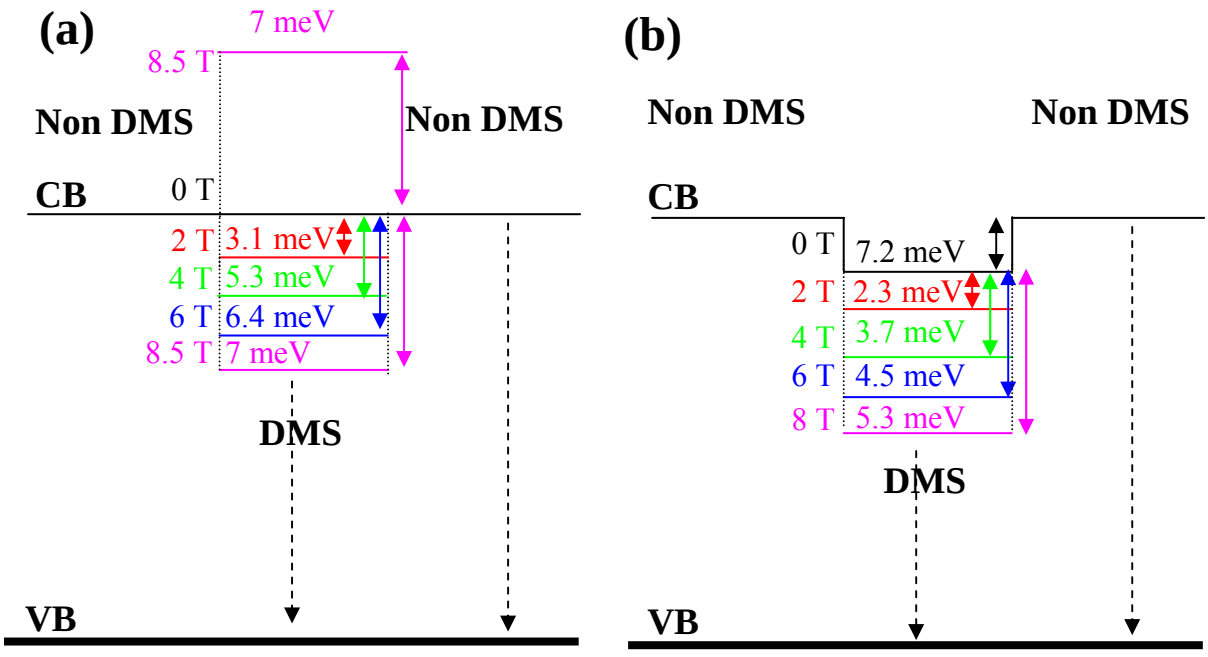

Figure 5.4 The schematic diagram of the changes of the conduction band offsets for spin-up and spin-down electrons calculated between the non DMS (CdMgTe) and DMS (CdMnTe) materials in the presence of the magnetic field. Two structures are shown: with zero band offset in the absence of magnetic field (a) and with a shallow magnetic quantum well (b).

Figure 5.4 (a) shows such changes for the structure with zero conduction band offset in the absence of magnetic field. One should notice that this structure corresponds to the

modulation doped SDMSQW $Cd_{0.85}Mn_{0.15}Te$/ $Cd_{0.85}Mg_{0.15}Te$ structure. As seen in Fig. 5.4 (a) increasing the magnetic field a shallow quantum well for spin-down electrons is being formed. The maximal value of the conduction band offset was found to be 7 meV at 8.5 T. It should be emphasized that the Zeeman spin splitting becomes smaller for a given temperature and magnetic field if content of Mn decreases and, thus, the depth of the quantum well also decreases in this case. On the other hand, the potential barrier formed for spin-up electrons increases as a function of magnetic field. To avoid confusion in Fig. 5.4 (a) we showed the position of the spin-up level of electrons only at 8.5 T. Therefore, as clearly follows from these calculations only spin-up electrons are confined inside the $Cd_{0.85}Mg_{0.15}Te$ barrier.

The conduction band offset for the structure consisted of a shallow quantum well in the absence of magnetic field is shown in Fig. 5.4 (b). One should notice that this structure corresponds to the spin superlattice consisted of 50 individual layers of 100 Å thick $Cd_{0.88}Mn_{0.12}Te$ and $Cd_{0.87}Mg_{0.13}Te$ epilayers. As seen in Fig. 5.4 (b) an apparent conduction band offset between the magnetic and nonmagnetic materials has been already observed in the absence of magnetic field. Moreover, this value was about 7.2 meV, which is found to be higher than that obtained for the highest magnetic field applied in the previous case (Fig. 5.4 (a)). When the magnetic field increases the depth of the quantum well for spin-down electrons also increases and reaches its maximal value (5.3 meV) at 8 T. For the spin-up level of electrons less than 2 meV conduction band offset between the magnetic and nonmagnetic materials was observed at 8 T (not shown in this figure). Thus, one can conclude that electrons for both spin orientations are confined in the DMS material in this case.

Figure 5.5 shows the positions of all peaks in the PL spectra shown in Figs. 5.2 and 5.3 as a function of magnetic field measured for both σ^+ and σ^- circular polarizations. One should notice that due to overlapping of peaks originating from the DMS and non DMS layers (Fig. 5.2) one cannot unambiguously evaluate the energy of the PL peak in the SDMSQW structures below 2 T. The solid lines in Fig. 5.5 show the fitting of experimental data using the Brillouin function (using T_{eff} and x_{eff} as fitting parameters), which determine the spin state of a paramagnet by varying the magnetic field at a constant temperature (see chapter 1). Using the Brillouin analysis the spin state of a material can be determined without knowing the exact chemical composition of the material, since it can be determined from the magnetization changed as a function of applied field. As seen in Fig. 5.5 the Brillouin function fits nicely the experimental data.

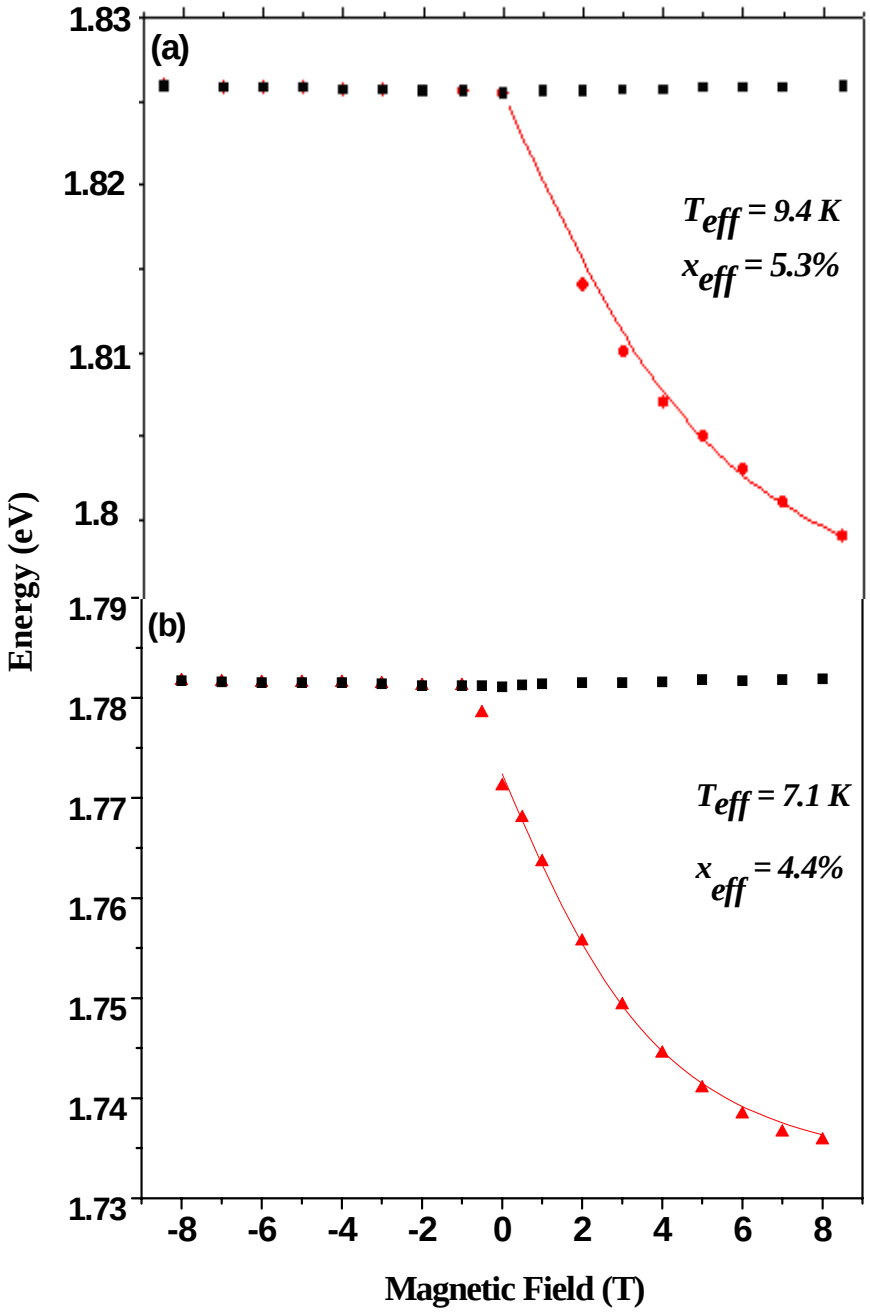

Figure 5.5 The positions of all peaks in the PL spectra shown in Figs. 5.2 and 5.3 as a function of the magnetic field measured for both σ^+ and σ^- circular polarizations. Red (black) points show the positions of peaks originating from the DMS material (non DMS). Solid lines in this figure are the fitting of experimental points using the Brillouin function.

It should be noticed that the differences between technological and fitting parameters mean that a fraction of Mn^{2+} ions form pairs and/or complexes with strong antiferromagnetic ordering, thus, producing no magnetic moment. That fraction understandably increases with the mount of manganese in the sample. The remaining ions (x_{eff}) align in the magnetic field according to a Brillouin function with T_{eff} greater than the real temperature. It reflects an antiferromagnetic type of interaction also among those ions [9]. Thus, from the Brillouin analysis together with the PL spectra shown in Figs. 5.2-5.3 one can conclude that:

Firstly, transitions between spin-down electrons ($m_j = -1/2$) and heavy holes ($m_j = -3/2$) which are localized in the DMS material are dominant in modulation I-doped SDMSQW measured using σ^+ circular polarization. In contrast to this the transitions between spin-up electrons ($m_j = 1/2$) and heavy holes ($m_j = 3/2$), which are localized in the nonmagnetic matrix are dominant for σ^- component.

Secondly, in spin superlattice structure with shallow magnetic quantum well in the absence of magnetic field transitions between spin-down electrons ($m_j = -1/2$) and heavy holes ($m_j = -3/2$) which are localized in the DMS material are dominant for σ^+ component whereas transitions between spin-up electrons ($m_j = 1/2$) and heavy holes ($m_j = 3/2$), which are also localized in the DMS material at low magnetic field are more likely for σ^- polarization.

Similar results have been also observed for spin superlattice with zero band offsets and for the SDMSQW structure having a shallow quantum well.

In the rest part of this section we would like to concentrate our attention on structures in which the initial magnetic barrier is formed between nonmagnetic regions. Figure 5.6 shows the PL spectra of the spin superlattice structure consisted of 50 individual layers of 100 Å thick $Cd_{0.88}Mn_{0.12}Te$ and 100 Å thick $Cd_{0.93}Mg_{0.07}Te$ epilayers measured with σ^- (a) and σ^+ (b) circular polarizations at 4.2 K. In this case the energy bandgap of the DMS material ($Cd_{0.88}Mn_{0.12}Te$) is larger than that of the nonmagnetic semiconductor ($Cd_{0.93}Mg_{0.07}Te$). This leads to the band offsets between these two materials. However, as mentioned above in contrast to the case described in Fig. 5.3 the spin superlattice containing magnetic barriers is formed in the present case. For such structure the band offsets decrease for spin-down electrons and increase for spin-up electrons with increasing magnetic field. As seen in Fig. 5.6 the only dominant peak at 1.716 eV was observed in the absence of magnetic field. The position of this peak does not depend on the magnetic field applied for both σ^+ and σ^- circular polarizations. Thus, it is very likely that the peak at 1.716 eV corresponds to a transition in the nonmagnetic $Cd_{0.93}Mg_{0.07}Te$ layer. This leads that both spin-up and spin-down electrons are confined inside the non DMS material.

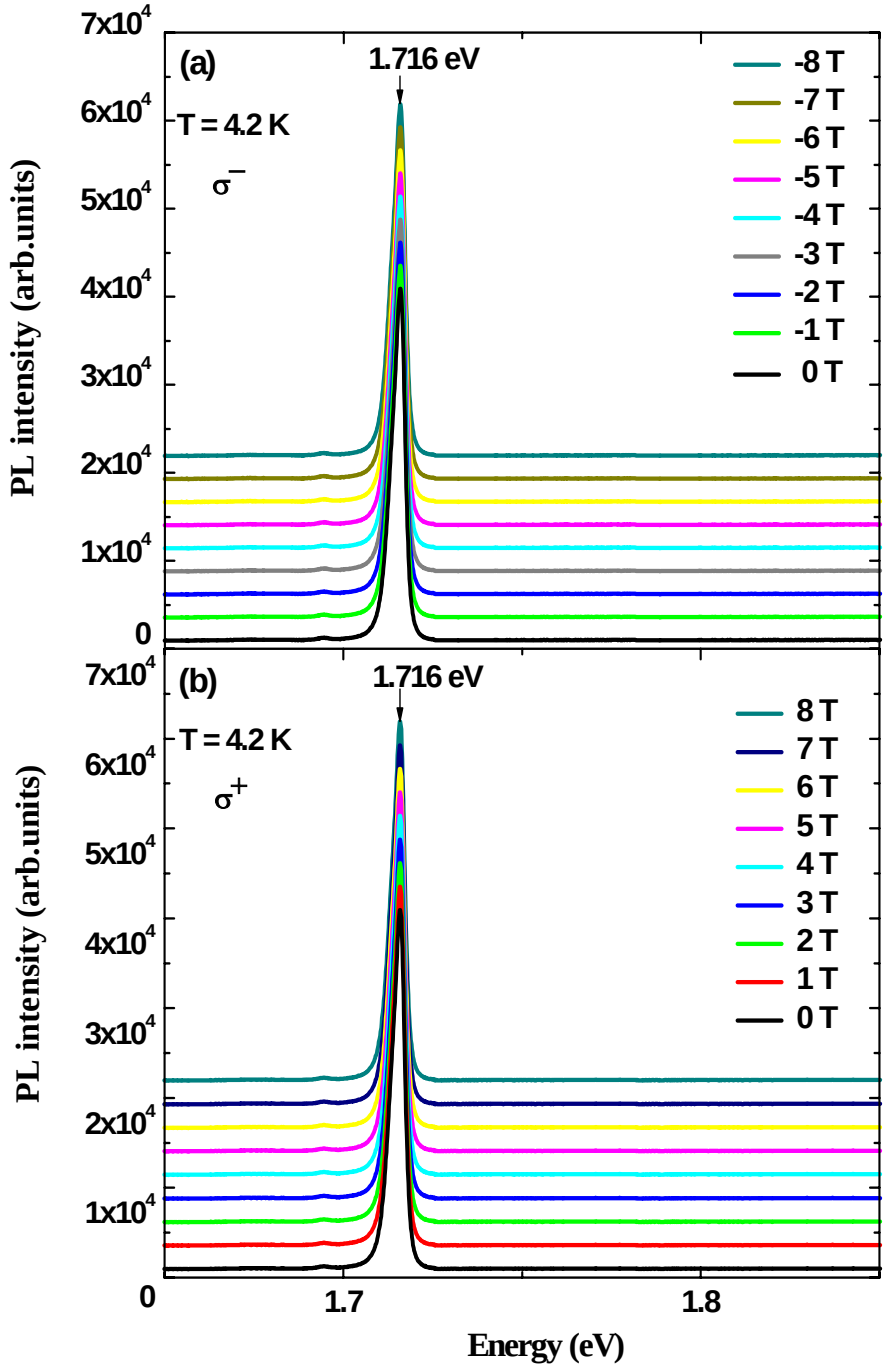

Figure 5.6 PL spectra recorded in the spin superlattice structure with magnetic $Cd_{0.88}Mn_{0.12}Te$ barrier and $Cd_{0.93}Mg_{0.07}Te$ quantum well obtained with σ^- (a) and σ^+ (b) circular polarizations for different values of the magnetic field at 4.2 K.

Summarizing, in this section we demonstrated that applying magnetic field one can confine electrons with spin-down and/or spin-up orientation in the DMS material embedded between two non DMS materials in different kinds of SDMSQW and spin superlattice structures: with zero band offsets, with a shallow magnetic quantum well and with a magnetic barrier.

5.3 Magneto-transport measurements of SDMSQW and spin superlattice structures

5.3.1 Hall resistivity measurements of SDMSQW structures

In this section we present results of magneto-transport measurements of SDMSQW structures. For this purpose the Hall effect measurements were performed in the presence of magnetic fields which was varied from -8.5 T to 8.5 T in the temperature range from 1.6 K to 300 K. One should notice that the magnetic field was perpendicular to the surface of the sample during these measurements.

Figure 5.7 shows the Hall resistivity (ρ_{xy}) of SDMSQW consisted of $Cd_{0.90}Mn_{0.10}Te$/ $Cd_{0.90}Mg_{0.10}Te$ structures measured as a function of magnetic field in the temperature range from 1.6 K to 300 K. The doped layer was separated from DMS QW by 200 Å thick spacer and from the surface by 2000 Å thick undoped cap layer. Two cases, in which iodine donors are introduced into 50 Å (Fig. 5.7 (a)) and 100 Å (Fig. 5.7 (b)) thick top barrier layers are presented in this figure. As seen in this plot the Hall resistivity depends linearly on magnetic field applied to the structure in two temperature ranges: from 1.6 K to 20 K and from 80 K to 300 K. As known the slope of the linear extrapolation determines a free carrier concentration in these structures. Thus, in this case the free electron concentration was found to be constant and independent on a magnetic field. However, a significant deflection of this linear dependence was observed in the range from 20 K to 80 K. This can be interpreted as changes of free carrier concentration, which occur with changing magnetic field in this temperature range. Following this idea, we plotted values of the electron concentration calculated from the Hall resistivity as a function of magnetic field (Fig. 5.8).

As seen in this figure the electron concentration has almost a constant value for different values of the magnetic field in both cases shown at 300 K. The slight decrease observed in this case (less than 10%) is believed to appear due to the magnetic freeze-out effect.

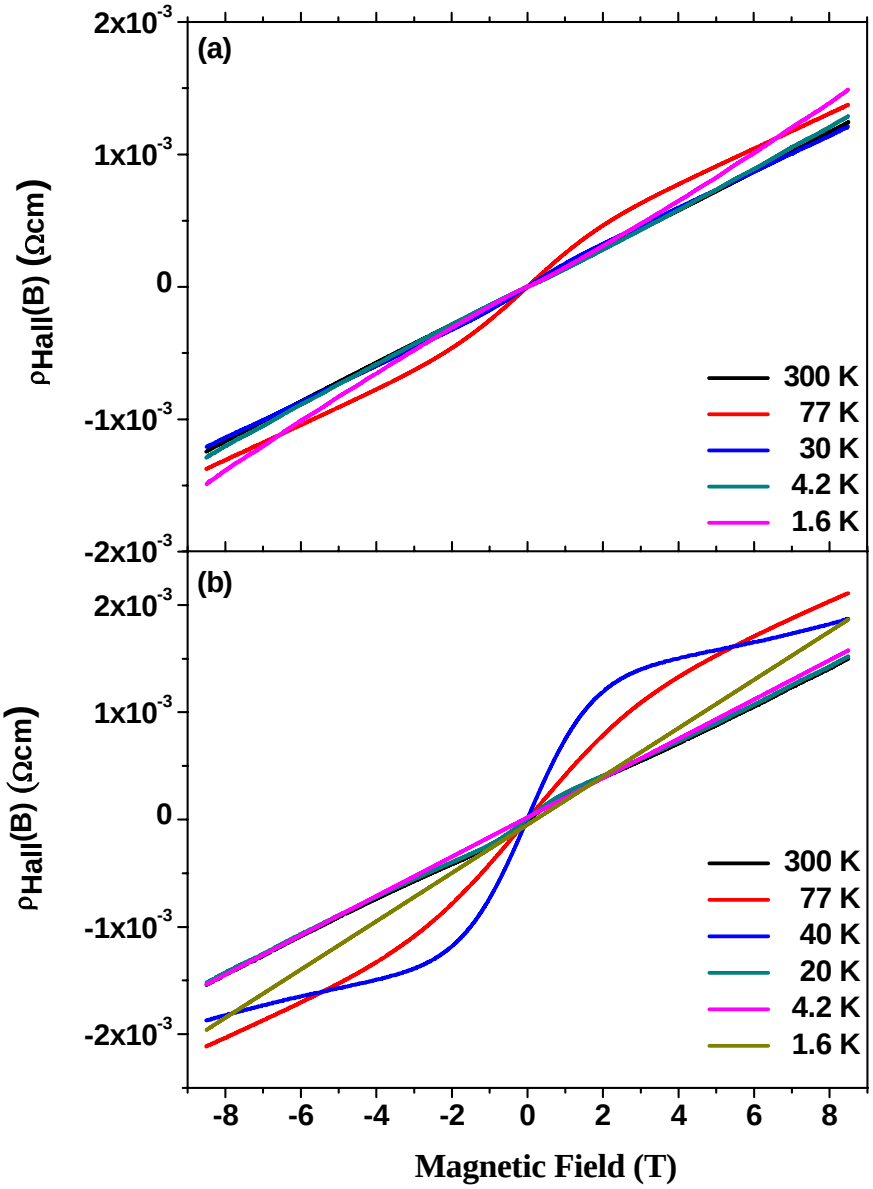

Figure 5.7 The Hall resistivity of SDMSQW consisted of $Cd_{0.90}Mn_{0.10}Te$/ $Cd_{0.90}Mg_{0.10}Te$ as a function of magnetic field measured in the temperature range from 1.6 K to 300 K. Two cases, in which iodine donors are introduced into 50 Å (Fig. 5.7 (a)) and 100 Å (Fig. 5.7 (b)) thick layers of the top barrier are shown.

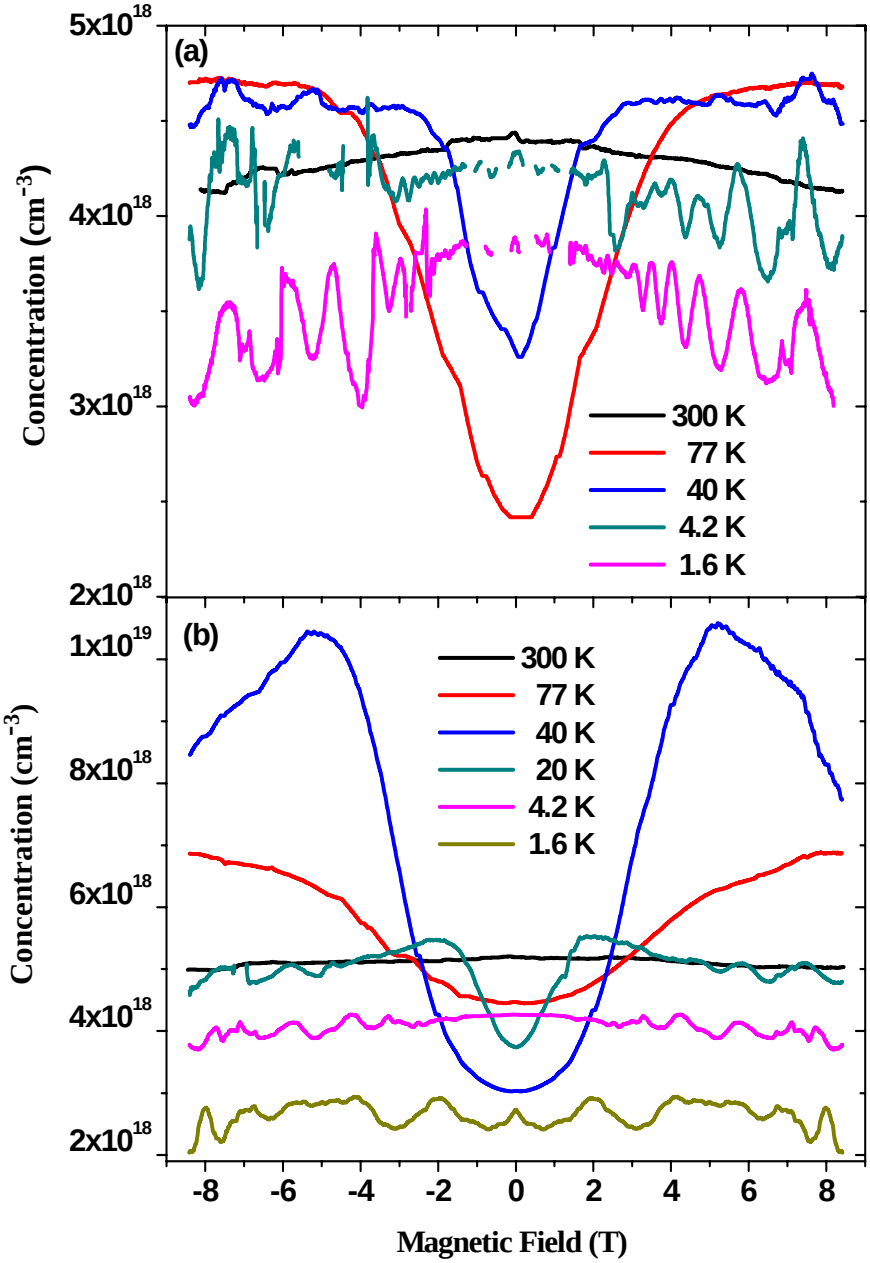

Figure 5.8 The carrier concentration determined from the Hall resistivity as a function of magnetic field for SDMSQW consisted of $Cd_{0.90}Mn_{0.10}Te/Cd_{0.90}Mg_{0.10}Te$ with the width of the doped region of 50 Å (a) and 100 Å (b), respectively.

However, the concentration of electrons drops down by a factor of two comparing with that at 300 K (from 4.45×10^{18} cm^{-3} to 2.4×10^{18} cm^{-3}) in the sample with 50 Å thick doped region in the absence of magnetic field at 77 K. On the other hand, only a slight decrease (about 30%) was observed in the sample with 100 Å thick doped region. When the magnetic field is applied to these structures, concentration of electrons increases significantly in both cases shown in Fig. 5.8. Moreover, this increase does not depend on the orientation of the magnetic field. This behavior indicates that a part of the conduction band electrons freezes-out on shallow donor states localized in the nonmagnetic $Cd_{1-y}Mg_yTe$ barriers and the magnetic field induces a quantum well in the magnetic $Cd_{1-x}Mn_xTe$ layer as was discussed in section 5.2. In this case thermally excited electrons can be captured by the well potential and contribute to the electrical transport. This leads to an increase of the carrier concentration observed in Fig. 5.8 at 77 K. Similar considerations can be also used to explain the curves observed at 40 K.

The characteristic feature of experimental results observed below 40 K is the Shubnikov-de Haas oscillations which are seen in Fig. 5.8 at the high values of the magnetic field applied. Such oscillations clearly indicate that highly mobile electrons confined in the quantum well, i.e., in a two-dimensional (2D) conductivity channel, significantly contribute to the electrical transport. Moreover, when temperature decreases the amplitude of the Shubnikov-de Haas oscillations increases whereas the period of these oscillations decreases. This unambiguously shows that the concentration and the mobility of electrons in the 2D channel increases.

From the Shubnikov-de Haas oscillations one can estimate the electron concentration in the 2D channel at low temperature when the Hall resistivity changes linearly as a function of magnetic field (see Fig. 5.9). These values were found to be 2.1×10^{18} cm^{-3} and 1.85×10^{18} cm^{-3} for structures with the width of the doped region of 50 Å (a) and 100 Å (b), respectively, at 1.6 K. However, both of them are different from those shown in Fig. 5.8. This clearly indicates that besides the 2D channel another channel of conductivity exists in these structures.

Wasik *et. al*. [10, 11] reported the calculated potential profiles of modulation doped CdTe/CdMgTe structures. In that work the authors demonstrated that in such structures a potential valley is formed spontaneously outside the quantum well in the region, which is doped with iodine donors. This leads to redistribution of free electrons between the quantum well and the side valley. And, therefore, an additional conductance channel (3D) appears inside the barrier in this case. The contribution of the 3D conductance channel varies strongly

with concentration of iodine donors introduced into the doped region, with the thickness of the spacer layer and with the depth of the quantum well. According to Wasik *et. al*. this 3D channel can be completely eliminated if the following conditions are carried out: the depth of the quantum well is larger than 240 meV, the spacer layer is not thicker than 20 nm and the cap layer is thicker than 150 nm. One should also notice that this can be also reached by decreasing a concentration of donors in the structures.

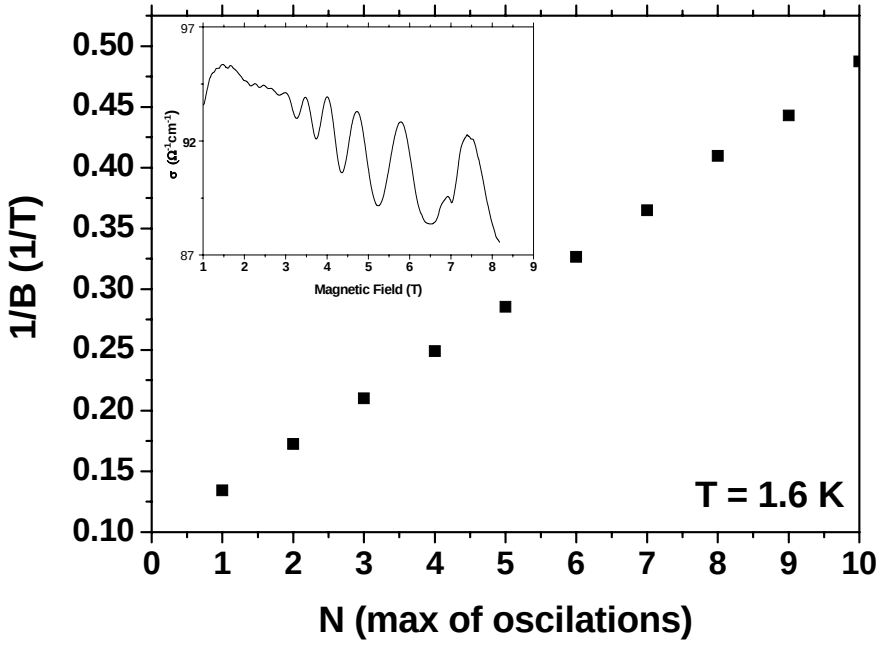

Figure 5.9 The Shubnikov-de Haas oscillations observed in the samples consisted of SDMSQW $Cd_{0.90}Mn_{0.10}Te$/ $Cd_{0.90}Mg_{0.10}Te$ with 100 Å thick of the doped region.

However, as shown in Fig. 5.4 the depth of the quantum well for spin-down electrons is only about 7 meV at 8.5 T in the structure with zero conduction band offset and only about 5 meV at 8 T in the structure with a shallow quantum well. These values are much smaller than that of 240 meV, which is necessary to have for elimination of the 3D conductivity channel. Moreover, changing the width of the spacer layer from 50 Å to 600 Å in the SDMSQW structures which have 2000 Å thick cap layer no significant difference in the magneto-transport measurements has been observed.

At last due to results reported by Wasik *et. al*. changes of electron concentration in the 2D channel have to be stronger with increasing magnetic field in structures with higher concentration of donors. This was indeed observed for the SDMSQW structures with 50 Å and 100 Å thick of the doped region (see Fig 5.7) in the present investigation. Unfortunately, we could not decrease the thickness of the doped region less than 25 Å. In this case, due to the

freeze-out effect, which leads to the high resistance of such structures (more than 10 $M\Omega$); it becomes impossible to perform the magneto-transport measurements.

To summarize experimental observations presented above we propose the model shown schematically in Fig. 5.10. As shown in this figure two parallel conduction channels can exist in the $Cd_{1-x}Mn_xTe$/ $Cd_{1-y}Mg_yTe$ structures. The first one with the thickness of QW region is formed in the $Cd_{1-x}Mn_xTe$ layer when the magnetic field is applied to the structure. Due to the defined thickness of the DMS layer electrons confined in this channel exhibit the 2D behavior manifested by the high mobility. The second channel is located in the doped $Cd_{1-y}Mg_yTe$ layer and is formed because of the electrostatic bending of the conduction band in the doped $Cd_{1-y}Mg_yTe$ layer. Due to this, the width of this channel is much wider than that of the 2D channel, and the 3D behavior of electrons in this channel is expected. The relative concentration of electrons in the 2D and 3D channels depends on both magnetic field and temperature. At room temperature, the Fermi level is located high in the conduction band and the influence of magnetic field on the process of conductivity can be neglected. In this case, the concentration of electrons localized in the 3D channel does not depend on the magnetic field (Fig. 5.10 (a)). However, in the range from 20 K to 80 K (Fig. 5.10 (b)), when the magnetic field is applied to the structure the electrons initially localized at shallow donors in the 3D channel can move to the magnetically induced 2D channel. This leads that all electrons are confined in the 2D channel even at low values of the magnetic field at 1.6 K (Fig. 5.10 (c)) [12].

As shown above changing the depth of the quantum well, the thickness of the cap layer and the thickness of the spacer layer one cannot completely eliminate the 3D channel in SDMSQW structures with zero band offsets or with a shallow quantum well. However, one can expect that the 3D and 2D channels could “match” each other in the structures with symmetrical doping layers relatively the QW region and in this case leads to elimination of the 3D channel. Figure 5.11 shows the Hall resistivity (ρ_{xy}) of $Cd_{0.95}Mn_{0.05}Te$/ $Cd_{0.95}Mg_{0.05}Te$ structures measured as a function of magnetic field in the temperature range from 1.6 K to 300 K. Iodine donors were intentionally symmetrically introduced into 75 Å (Fig. 5.11 (a)) and 100 Å (Fig. 5.11 (b)) thick layers above and under magnetic barriers. It should be noticed that in this case the doped layer has not been separated from the quantum well by the undoped spacer layer. The whole structure was covered by 2000 Å thick cap layer. As seen in Fig. 5.11 qualitatively similar results to those presented in Fig. 5.7 have been observed in the present case as well. Thus, even in this case one cannot entirely eliminate the 3D channel of conductivity.

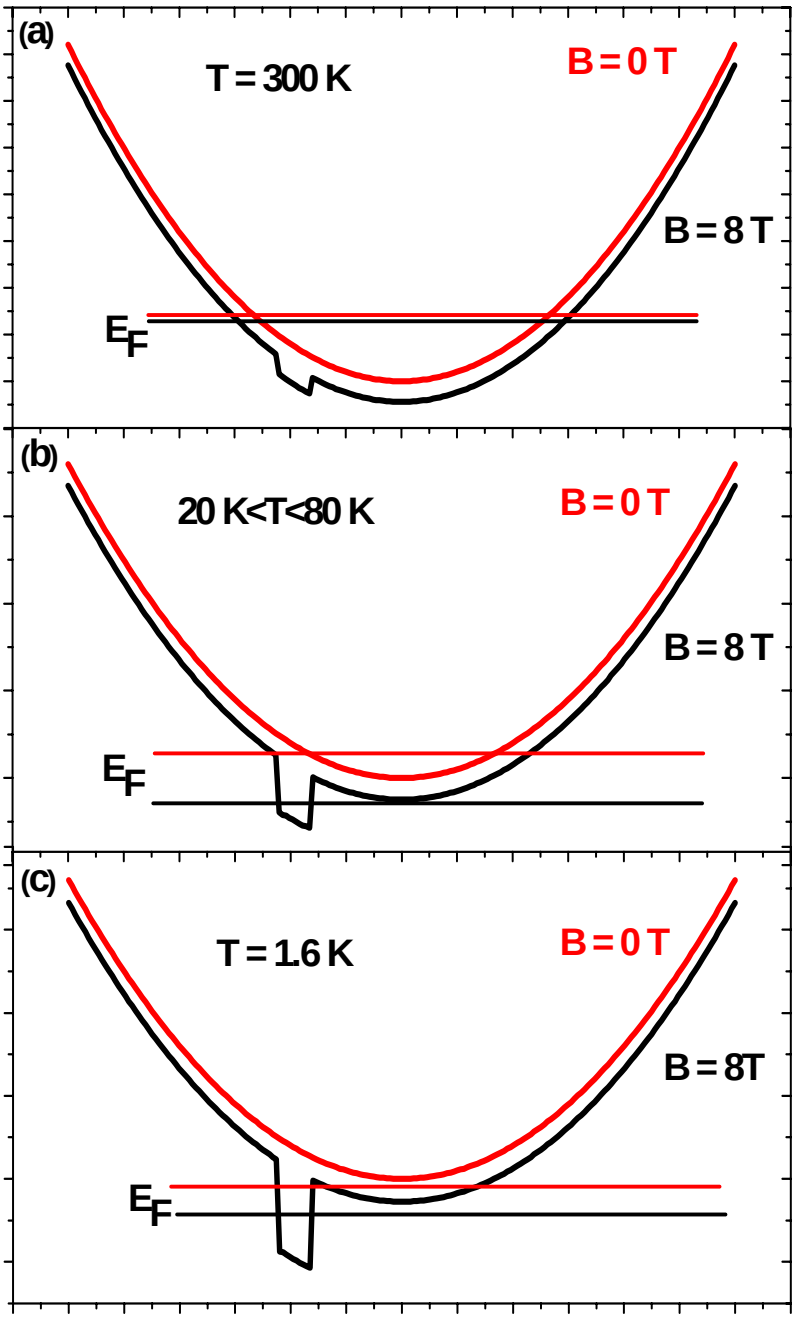

Figure 5.10 The schematic drawing of the alignment of the conduction bands in the vicinity of the $Cd_{1-x}Mn_xTe$/ $Cd_{1-y}Mg_yTe$ heterojunction in the absence of magnetic field and at 8 T.

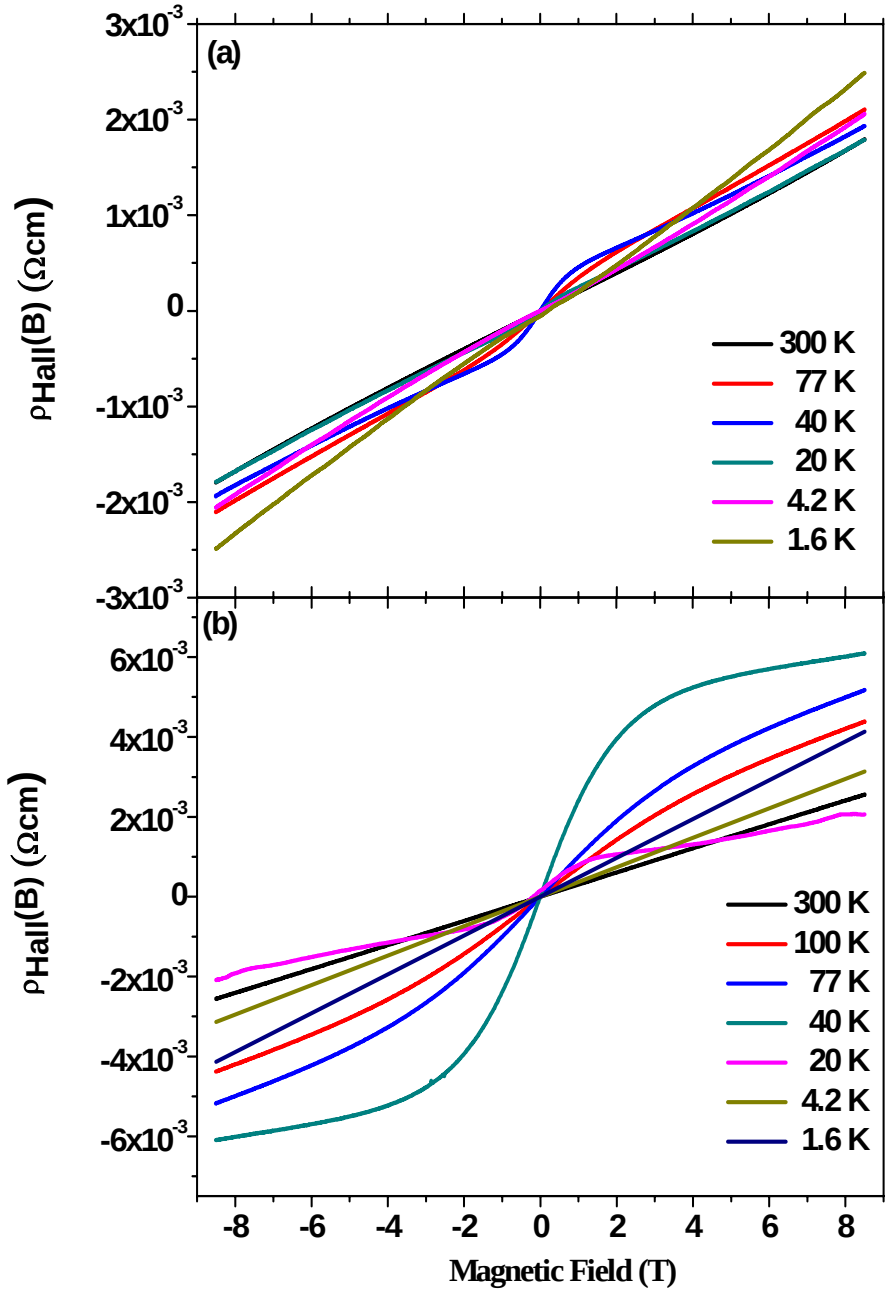

Figure 5.11 Hall resistivity of SDMSQW structures consisted of $Cd_{0.95}Mn_{0.05}Te/Cd_{0.95}Mg_{0.05}Te$ with the width of the doped region of 75 Å (a) and 100 Å (b) measured as a function of magnetic field at different temperatures.

5.3.2 Hall resistivity measurements of spin superlattice structures

In this section we present results of magneto-transport measurements in spin superlattice (SSL) structures, which consist of many repetitions of SDMSQWs described in details in the previous paragraph. All magneto-transport measurements were carried out in the presence of magnetic field which was varied from -8.5 T to 8.5 T in the temperature range from 1.6 K to 300 K.

Figure 5.12 shows the typical Hall resistivity (ρ_{xy}) of the modulation doped spin superlattice structures consisting of 25 loops of 200 Å thick $Cd_{0.95}Mn_{0.05}Te$ magnetic layer and 50 Å thick $Cd_{0.95}Mg_{0.05}Te$ nonmagnetic barrier measured as a function of magnetic field in the temperature range from 1.6 K to 300 K. In this case one can say that the spin superlattice structures were fabricated in a wide quantum well. This means that the content of Mg in spin superlattices is significantly less than 30% as it is in the buffer and cap layers. The width of the cap layer consisted of $Cd_{0.70}Mg_{0.30}Te$ is 2000 Å in this case. All structures were doped by iodine into 4 Å (Fig. 5. 12 (a)), 25 Å (Fig. 5.12 (b)) and 100 Å (Fig. 5.12 (c)) thick layers of the top barrier. As seen in Fig. 5.12 in all these cases ρ_{xy} depends linearly as a function of magnetic field in the whole range of temperatures. Similar results were also observed for all types of spin superlattice structures. This linear dependence can be only explained by the dominant role of the 3D channel in the conductivity process. As mentioned above this channel forms a deep potential valley and the main part of electrons contribute to the conductivity process using this channel. However, one should emphasize that even in this case the conductivity through the 2D channel cannot be entirely excluded due to the presence of small Shubnikov-de Haas oscillations at low temperature and a small increase of mobility of electrons observed in this case.

From Fig. 5.12 concentration of electrons was found to be 5×10^{18} cm^{-3} at 1.6 K and 5.5×10^{18} cm^{-3} at 300 K for the sample with 100 Å thick high-doped layer whereas it was slightly smaller for other structures: 2.9×10^{18} cm^{-3} at 1.6 K and 3.7×10^{18} cm^{-3} at 300 K for the structure with 25 Å thick the doped layer, and 1.4×10^{18} cm^{-3} at 1.6 K and 2.3×10^{18} cm^{-3} at 300 K for the structure with 4 Å thick the doped layer. One should emphasize that as clearly follows from these results all these semiconductors are degenerated. Similar results have been also observed in the spin superlattice structures with different width of the spacer layer and with different content of magnetic impurities.

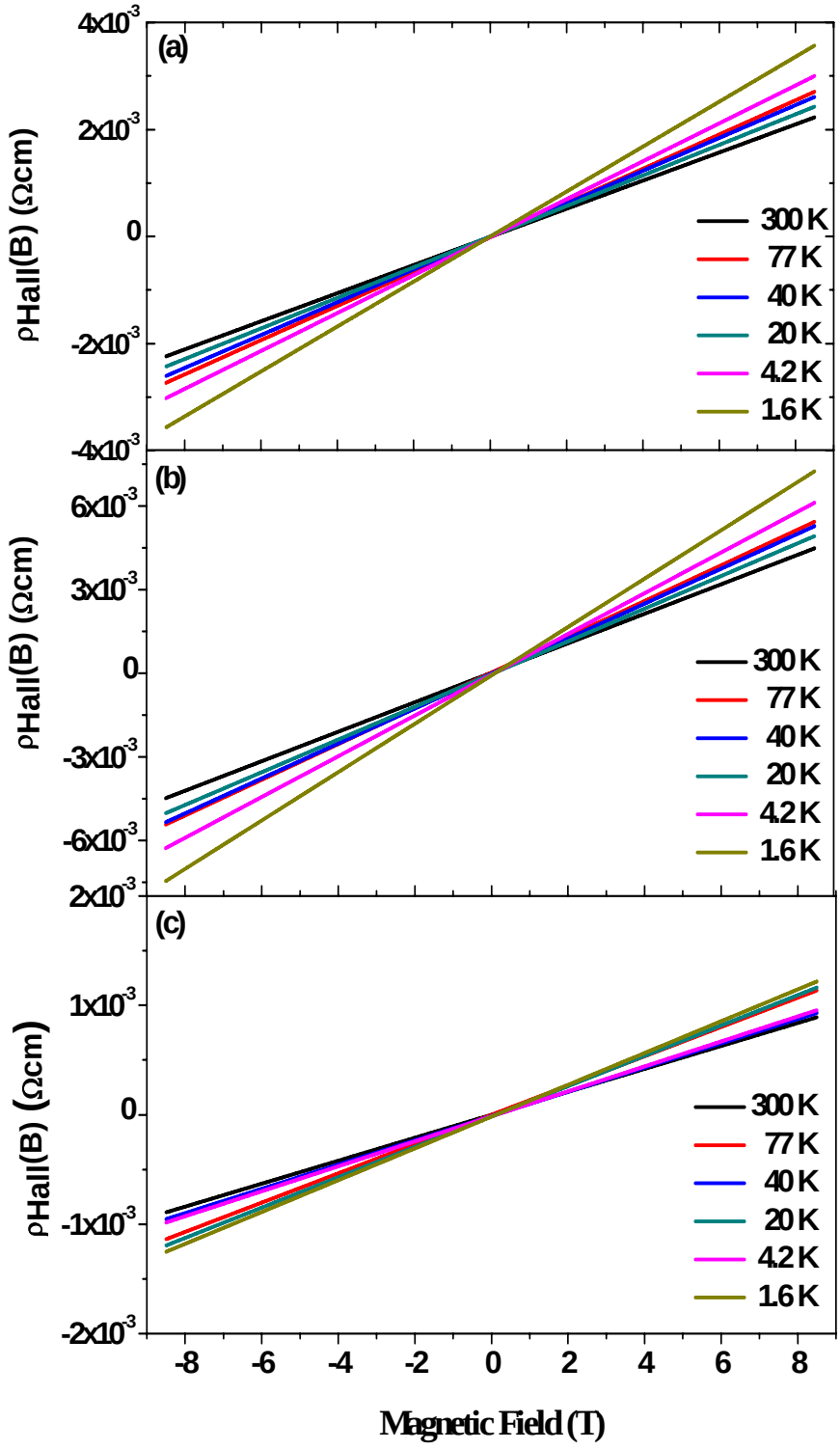

Figure 5.12 The Hall resistivity of the modulation doped spin superlattices consisted of $Cd_{0.95}Mn_{0.05}Te/Cd_{0.95}Mg_{0.05}Te$ with the width of the doped region of 4 Å (a), 25 Å (b) and 100 Å (c) measured as a function of the magnetic field in the temperature range from 1.6 K to 300 K.

5.3.3 The longitudinal magnetoresistance of SDMSQW and spin superlattice structures

In this section results of changes of longitudinal magnetoresistance in SDMSQW and spin superlattice structures measured as a function of magnetic field will be presented.

Figure 5.13 shows changes of the longitudinal magnetoresistance $\rho_{xx}(B)$-$\rho_{xx}(0)$ of the typical modulation doped SDMSQW structures consisted of $Cd_{0.99}Mn_{0.01}Te/Cd_{0.99}Mg_{0.01}Te$ with 50 Å (Fig. 5.13 (a)) and 100 Å (Fig. 5.13 (b)) thick doped region measured as a function of the magnetic field in the temperature range from 1.6 K to 300 K.

As seen in this figure a classical parabolic dependence was observed for both structures above 40 K. However, a significant deviation from the parabolic dependence was detected below this temperature. In this case applying the magnetic field to such structures a drop of resistivity of SDMSQWs is clearly seen in Fig. 5.13. This drop increases towards the lower temperatures. Moreover, it also increases significantly if the content of Mn or the doping level increases. We ascribe these phenomena the weak localization (WL) effect. This effect originates from successive coherent scattering events, which return the electron to its starting point. As the scattering probability in the clockwise and the counterclockwise directions is identical because of time reversal symmetry, the Feynman path amplitudes add coherently and the probability for backscattering is enhanced by a factor of two comparing with non-coherent overlapping. This leads to a reduced diffusivity and thus also to a reduced conductivity. If the circulation time of the electron in such a loop exceeds the phase coherence time, the coherent effect is destroyed and therefore limits the size of the effect. The phase coherence in the backscattering loop can also be distorted by a magnetic field due to the lifting of time reversal [13, 14]. Thus, the magnetic field quenches the WL contribution and results in a negative magnetoresistance (negative difference of $\rho_{xx}(B)$-$\rho_{xx}(0)$) which is observed in Fig. 5.13.

Another interesting observation in Fig. 5.13 is an obvious saturation of $\rho_{xx}(B)$-$\rho_{xx}(0)$ at high magnetic fields. This saturation clearly indicates the presence of the 3D channel of conductivity in such structures [11].

Figure 5.14 shows changes of the longitudinal magnetoresistance $\rho_{xx}(B)$-$\rho_{xx}(0)$ in the spin superlattice structures measured as a function of magnetic field at 1.6 K. The spin superlattice structures consisted of 25 loops of 200 Å thick $Cd_{1-x}Mn_xTe$, 50 Å thick $Cd_{0.95}Mg_{0.05}Te$ barrier, and 100 Å thick I-doped $Cd_{0.95}Mg_{0.05}Te$. Mn content was changed in different samples and equal x = 0%, 1%, 5% and 14%, respectively.

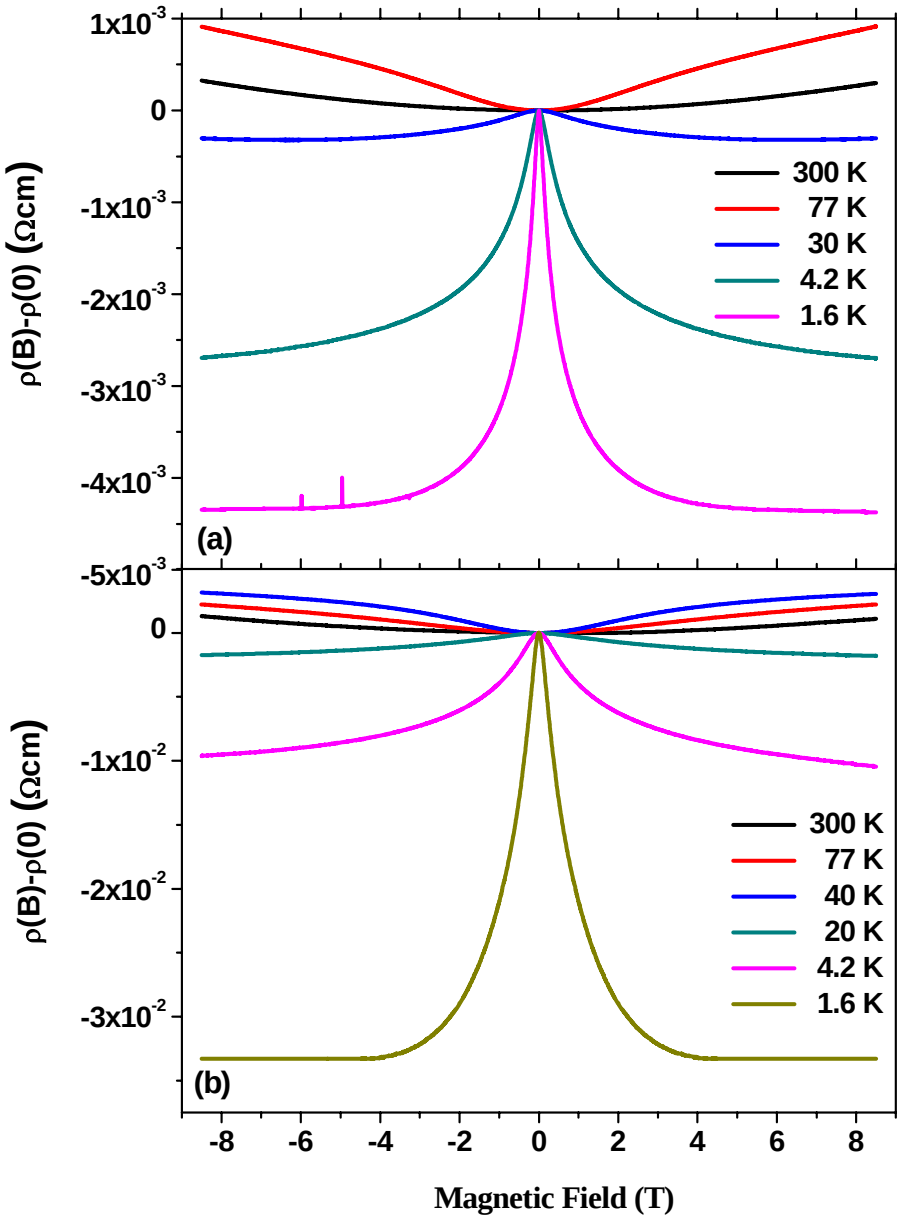

Figure 5.13 Changes of the longitudinal resistivity $(\rho_{xx}(B)-\rho_{xx}(0))$ of SDMSQW consisted of $Cd_{0.99}Mn_{0.01}Te$/ $Cd_{0.99}Mg_{0.01}Te$ with 50 Å (a) and 100 Å (b) doped region measured as a function of magnetic field in the temperature range from 1.6 K to 300 K.

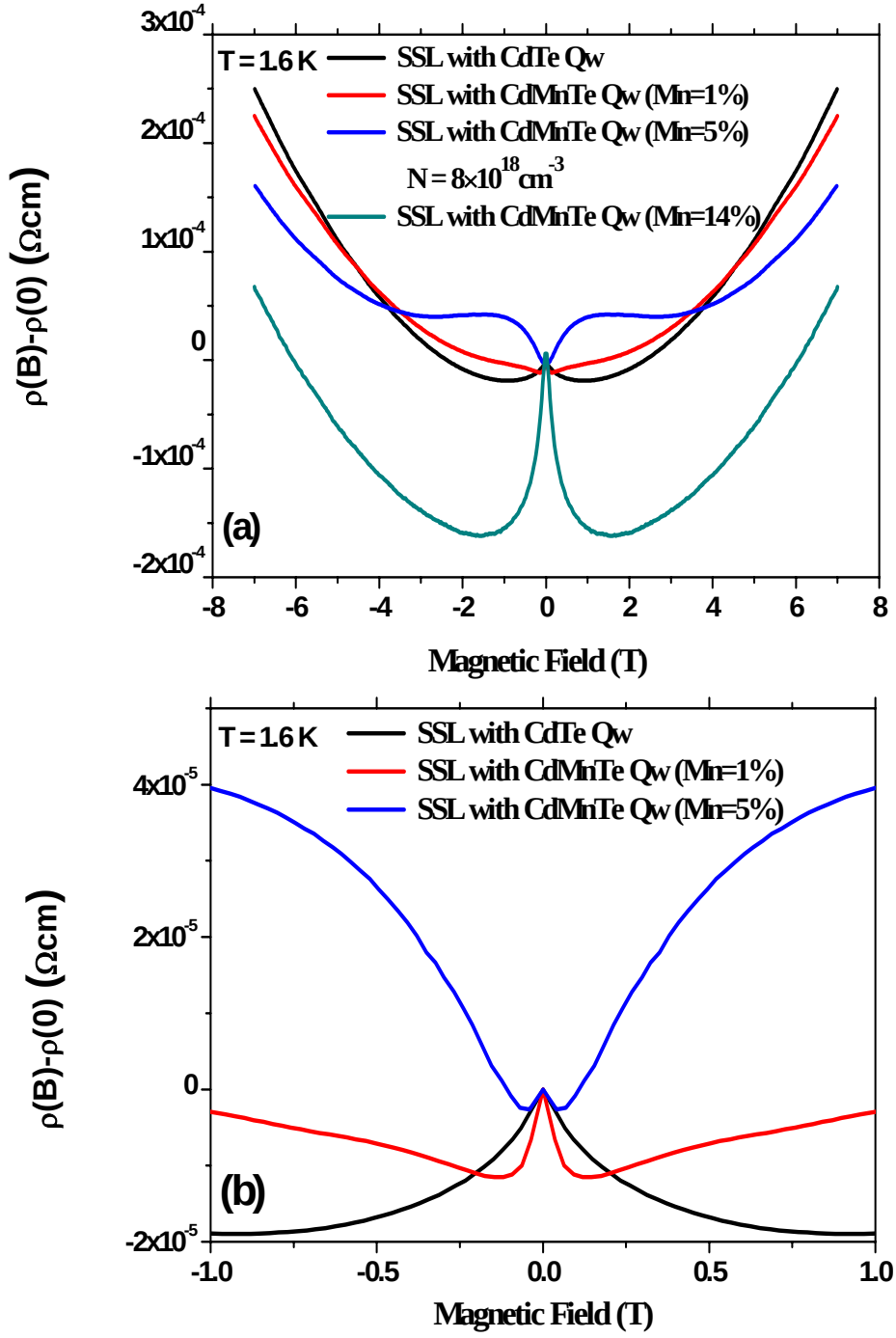

Figure 5.14 Changes of the longitudinal resistivity ($\rho_{xx}(B)$-$\rho_{xx}(0)$) of the spin superlattice structures with different content of Mn measured as a function of the magnetic field at 1.6 K (a). For the sake of clarity these curves besides the one containing 14% of Mn are enlarged in the vicinity of 0 T (b).

Similar to the SDMSQW structures a negative magnetoresistance effect was also observed in the spin superlattice structures, however, only in the vicinity of 0 T. Moreover, this effect becomes more pronounced in the structures having more and less than 5% of Mn. Thus, we believe that this can be caused by the presence of the lattice mismatch between the magnetic quantum well and nonmagnetic barriers. Indeed, if content of Mn in the quantum well region is not equal to that of Mg in the nonmagnetic barrier various defects (point defects, dislocations and so on) have a tendency to appear. One should also emphasize that decreasing the lattice mismatch the WL effect which is inseparable linked with the order existing in the system also decreases and the opposite tendency can be observed when the lattice mismatch increases. Thus, from this point of view the lattice mismatch is closely bound the WL effect described in the previous case. This is entirely consistent with our observations shown in Fig. 5.14 (b).

However, one should remember that some other effects can also contribute to negative values of $\rho_{xx}(B)-\rho_{xx}(0)$.

First of all, it concerns the effect related to disorder-induced electron-electron interaction (EEI) in the electron-electron quasi-particle diffusion channel [12, 15]. Due to this interaction changes of the longitudinal magnetoresistance as a function of magnetic field behave similarly comparing with those originating from the WL effect. On the other hand such changes are expected to be much smaller than those due to the WL effect.

The second phenomena, which should be paid attention on is associated with redistribution of electrons between two spin subbands split as a result of the magnetic field applied [16]. This splitting causes electrons to shift from the minority-spin subband to the majority-spin one. In this case the redistribution of electrons can affect the resistivity in several ways. Firstly, as shown in Ref. [17] the mobility of an electron increases with its energy. As spin splitting increases, the electron redistribution raises the Fermi energy in the majority-spin subband, whereas it lowers the Fermi energy in the minority-spin subband. This leads to a significant increase of the mobility in the majority spin subband.

When contribution of both subbands is added, the net effect of these changes in the Fermi energies is negative magnetoresistance. However, this effect is expected to be more pronounced in high magnetic fields. In contrast to this model, D. J. Kim *et. al.* [18] and Z. Gan *et. al.* [19] demonstrated that such splitting can result in two competing effects. The first one is the change of the screening radius with splitting energy which leads to positive magnetoresistance, whereas the changes of Fermi energy in both subbands tends to produce negative magnetoresistance.

Finally, one should emphasize that changes of longitudinal magnetoresistance depends significantly on the doping level of I-doped CdMgTe. Shapira *et. al.* [20] showed that if concentration of electrons is below 2×10^{17} cm^{-3} in $Cd_{0.95}Mn_{0.05}Te$ the resistivity of such structure changes in an opposite way than it is observed for the higher doping levels. This is very well consistent with our observations shown in Figs. 5.14 and 5.15. As seen in Fig. 5.15 significant positive magnetoresistance was observed in the structures with concentration of electrons about 5×10^{16} cm^{-3} in the doped region in magnetic fields varying from -2 T to 2 T.

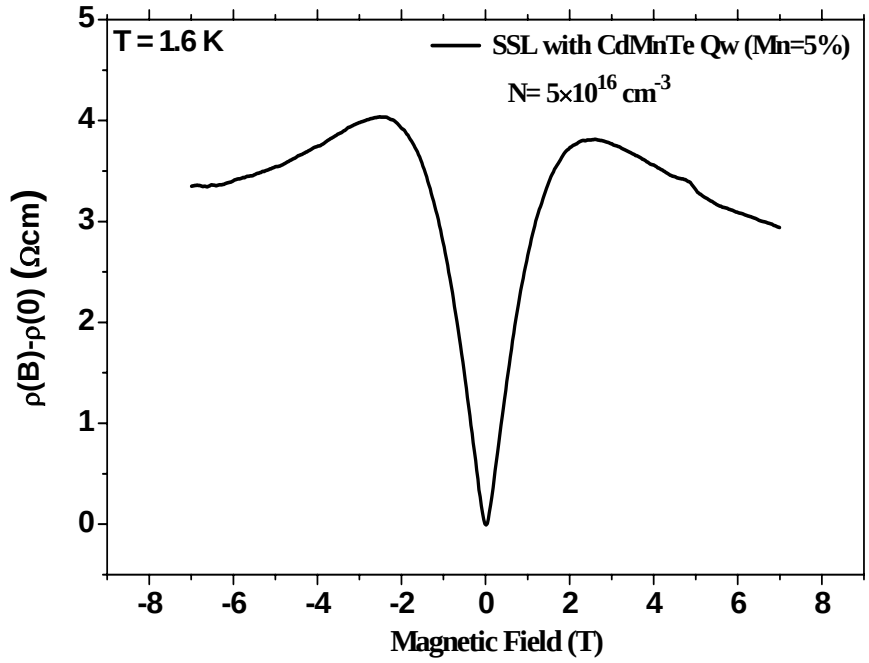

Figure 5.15 The change of the longitudinal resistance $\rho_{xx}(B)-\rho_{xx}(0)$ of the spin superlattice structure consisted of $Cd_{0.95}Mn_{0.05}Te$/ $Cd_{0.95}Mg_{0.05}Te$ measured as function of magnetic field at 1.6 K.

5.4 Conclusions

In this chapter, results of magneto-optical and magneto-transport measurements in the SDMSQW and spin superlattice structures have been presented.

From the magneto-optical measurements we demonstrated that applying magnetic field one can confine electrons with spin-down or/and spin-up orientation in the DMS material embedded between two non DMS materials in different kinds of SDMSQW and spin superlattice structures: with zero band offsets, with a shallow magnetic quantum well and with a magnetic barrier.

From the Hall effect measurements, three temperature regions in the dependence of Hall resistivity as a function of magnetic field can be distinguished in the SDMSQW structures. The first one is a region of high temperatures (from 80 K to 300 K) in which $\rho_{xy}(B)$ changes linearly as a function of magnetic field. However, a significant deflection from such linear dependence was observed in the second region from 20 K to 80 K. This clearly indicates that changes of free carrier concentration occur under different values of magnetic field in this temperature range. The linear behavior of ρ_{xy} was also observed in the third region, in which temperature changes from 1.6 K to 20 K. Due to this experimental observations two parallel channels of conductivity were concluded to exist in the SDMSQW structures. The first one is formed in $Cd_{1-x}Mn_xTe$ layer when the magnetic field is applied to the structure. Due to the defined width of the DMS layer electrons confined in this channel exhibit the 2D behavior which is also accompanied by the higher mobility of these carriers. On the other hand, the second channel is formed due to the electrostatic bending of the conduction band in the doped $Cd_{1-y}Mg_yTe$ layer. The width of this channel is much wider than that of the 2D channel. Thus, the 3D behavior of the electrons in this channel has been concluded. The relative concentrations of electrons in the 2D and 3D channels were found to depend on both magnetic field and temperature. At room temperature, the Fermi level is located high enough in the conduction band and influence of the magnetic field on the process of conductivity can be neglected. In this case, concentration of electrons localized in the 3D channel does not depend on the magnetic field. However, in the range from 20 K to 80 K, when the magnetic field is applied to the structure electrons initially localized at shallow donors in the 3D channel can move to the magnetically induced 2D channel. This leads that all electrons are confined in the 2D channel even at low magnetic fields at 1.6 K.

On the other hand, in spin superlattice structures the Hall resistivity ρ_{xy} was found depend linearly as a function of magnetic field in the whole temperature range. From this, a

dominant role of the 3D channel in the conductivity process has been concluded. However, due to the presence of Shubnikov-de Haas oscillations observed at low temperature one cannot entirely exclude that a small part of electrons contribute to the conductivity process using the 2D channel.

From measurements of changes of the longitudinal resistance of both SDMSQW and spin superlattice structures as a function of magnetic field a negative magnetoresistance effect observed at low values of magnetic fields was explained using the WL effect and the lattice mismatch effect. However, a contribution from several other phenomena such as a spin splitting of the conduction band or disorder-induced electron-electron interactions cannot be also excluded.

5.5 Literature

[1] M. Von. Ortenberg, Phys. Rev. Lett. **49** (14), 1041 (1982).

[2] N. Dai, H. Luo, F. C. Zhang, N. Samarth, M. Dobrowolska, and J. K. Surdyna, Phys. Rev. Lett. **67** (27), 3824 (1991).

[3] X. Liu, A. Petrou, J. Warnock, B.T. Jonker, G. A. Prinz, J. J. Krebs, Phys. Rev. Lett. **63,** 2280 (1989).

[4] B. T. Jonker, X. Liu, W. C. Chou, A. Petrou, J. Appl. Phys. **69,** 6097 (1991).

[5] B. Kuhn-Heinrich, W. Ossau, T. Litz, A. Waag and G. Landwehr, J. Appl. Phys. **75,** 8046 (1995).

[6] B. Kuhn-Heinrich, W. Ossau, H. Heinke, F. Fischer, T. Litz, A. Waag and G. Landwehr, Appl. Phys. Lett. **63,** 2932 (1993).

[7] R. J. Nicholas, Phys. B **191,** 156 (1993).

[8] I. Zutic, J. Fabian, S. Das Sarma, Rev. of Modern Phys.**76** (2), 323 (2004).

[9] J. Gaj, R. Panel, G. Fishman, Sol. State Commun. **29**, 435 (1979).

[10] D. Wasik, M. Baj, J. Siwiec-Matuszyk, T. Wojtowicz, E. Janik, G. Karczewski, J. Appl. Phys. **91** (2), 753 (2002).

[11] D. Wasik, M. Baj, J. Siwiec-Matuszyk, T. Wojtowicz, E. Janik, G. Karczewski, Phys. Stat. Sol. (b) **229** (1), 183 (2002).

[12] V. Kolkovsky, M. Wiater, T. Wojtowicz, J. Jaroszynski, G. Karczewski, J. Korean Phys. Soc. **53** (5), 3068 (2008).

[13] A. Prinz, G. Bruntthaler, M. Sawicki, G. Bauer, K. Ismail, B. S. Meyerson, Thin Solid Films **294,** 179 (1997).

[14] B. L. Altshuler and S. G. Aronov, in A. L. Efros and M. Pollak (eds.), "*Electron-Electron Interactions in Disordered Systems*" (North Holland, Amsterdam, 1985).

[15] I. P. Smorchkova, N. Samarth, J. M. Kikkawa, D. D. Awschalom, Phys. Rev. Lett. **78,** (18) 3571 (1997).

[16] Y. Shapira, N. F. Oliveira, P. Becla, T. Q. Vu, Phys. Rev. B **41** (9), 5931 (1990).

[17] H. Fukuyama and K. Yosida, J. Phys. Soc. Jpn. **46**, 102 (1979).

[18] D. J. Kim and B. B. Schwartz, Phys. Rev. B **15**, 377 (1977).

[19] Z. Gan and P. A. Lee (unpublished).

[20] Y. Shapira, "*Diluted Magnetic Semiconductors"*, edited by R. L. Aggarwal, J. K. Furdyna, and S. von Molnar (Materials Research Society, Pittsburgh, 1988).

Summary

Molecular Beam Epitaxy (MBE) is a versatile technique used for growing thin epitaxial structures of semiconductors, metals or insulators. The main goals of the present work were twofold. First of all in order to create high quality semiconductor nanostructures all technological processes and parameters in the MBE chamber should be optimized. Secondly, as mentioned in motivation of the present work using the optimized characteristics we mainly concentrated on investigation of various phenomena linked with the presence of diluted magnetic semiconductors in nanostructures and, thus, having a potential practical application in the field of Spintronics.

Inspired by theoretical predictions of Zutic and Fabian, described in details in Chapter 1 of the present thesis the first part of my work was devoted to construction and the following characterization of electrical and optical properties of fundamental magnetic nanodevices: the magnetic *p-n* junctions described in Chapter 3 and the magnetic bipolar transistors described in Chapter 4.

As shown in Chapter 3 we have succeeded in fabrication of high quality magnetic *p-n* junctions with different concentration of magnetic impurities and various doping levels. However, despite on the high quality nanodevices fabricated by the MBE technique we have observed none of magneto-voltaic (spin-voltaic) and spin-valve effects which were predicted by Zutic and Fabian. We believe that the main reason of this is related to small changes of the barrier height for electrons in the presence of magnetic field comparing to the initial barrier height in the absence of magnetic field. In their calculations Zutic and Fabian used very low concentrations of both electrons and holes which lead to the quite low barrier heights comparing with those in the present investigation. On the other hand, due to the freeze-out effect we could not significantly decrease the concentration of free carriers in the magnetic structures. Trying to decrease the barrier height in zero magnetic field, we fabricated *p-i-n* structures with different thickness of the intrinsic magnetic layer and different content of magnetic impurities. However, even in this case the barrier height was too high for electrons. One should emphasize that both *p-n* and *p-i-n* structures showed the electrical characteristics of high quality diodes in the whole temperature range from 50 K to 300 K. Moreover, applying forward bias such diodes could effectively emit light and, therefore, serve as Light Emitting Diodes. All these observations clearly indicate that the quality of these structures can be safely ruled out as a possible reason which is responsible for the absence of the magnetic

effects. However, besides the high barrier height some other phenomena such as relaxation mechanisms, the geometry of samples and the freeze-out effect cannot be also excluded to contribute to such observations.

Similar results have been also obtained in various series of *n-p-n* spin transistors playing as a current amplifier, which were fabricated with different width of the base region and different concentration of the magnetic impurity (Mn).

In the last part of the present thesis we investigated the influence of the giant spin splitting effect on the magneto-optical and magneto-electrical properties of single diluted magnetic semiconductor quantum well and spin superlattice structures. From magneto-optical measurements we have demonstrated that the spatial separation of spin-up and spin-down electrons can be achieved even at low values of magnetic field. This is due to the large spin-splitting of the band edges in the semimagnetic (CdMn)Te layers which is entirely controlled by the external magnetic fields. On the other hand, the Hall effect measurements demonstrated that both 2D and 3D channels of conductivity exist in the SDMSQW structures whereas a dominant role of the 3D channel has been concluded in the spin superlattice structures.

On the other hand, in spin superlattice structures the Hall resistivity ρ_{xy} was found depend linearly as a function of magnetic field in the whole temperature range. From this, a dominant role of the 3D channel in the conductivity process has been concluded. However, due to the presence of Shubnikov-de Haas oscillations observed at low temperature one cannot entirely exclude that a small part of electrons contribute to the conductivity process using the 2D channel.

Finally, from measurements of changes of the longitudinal resistance of both SDMSQW and spin superlattice structures as a function of magnetic field a classical parabolic dependence has been observed at high temperatures. On the other hand, at low temperatures a negative magnetoresistance effect observed at low values of magnetic fields was explained using the WL effect and the lattice mismatch effect. However, in this latter case a contribution from several other phenomena such as a spin splitting of the conduction band or disorder-induced electron-electron interactions cannot be also excluded.